10-23-2017

Studying the Reaction 34AR(ALPHA,P)37K and Its Impact on XRB Nucleosynthesis and Observables

Amber C. Lauer
Louisiana State University at Baton Rouge, alauer1@lsu.edu

STUDYING THE REACTION 34AR(ALPHA,P)37K AND ITS IMPACT ON XRB NUCLEOSYNTHESIS AND OBSERVABLES

A Dissertation

Submitted to the Graduate Faculty of the
Louisiana State University and
Agricultural and Mechanical College
in partial fulfillment of the
requirements for the degree of
Doctor of Philosophy

in

The Department of Physics and Astronomy

by
Amber C. Lauer
B.S., Portland State University, 2007
M.S., Portland State University, 2011
December 2017

This work is dedicated to all the women before me who didn't have this chance.

Acknowledgments

I would especially like to thank my parents, Patty, Ken, Judie, and Jay, for endless support and encouragement. Knowing you're proud makes me proud. I would also like to thank my adviser Catherine Deibel for her endless patience, and always looking out. Thanks for opportunities I've never had, and never thought I would. Thanks to Jeff Blackmon for his experimental knowledge, and family puppy sitting services. I also want to thank Erik Sánchez and Sean Larsen at Portland State University for exposing me to research and believing I was smart when I didn't, and especially to Erik for allowing me all that time on his SEM. That was when I fell in love with physics. Thanks to John Dowling for getting me, and to Geoff Clayton for doing things differently. Thanks to Juhan Frank for his immense Stellar Evolution expertise and for listening. Thanks to my group members, Ashley, Erin, Jianping, Kevin, and Lyuda, for late night insanity while working on experiments. Thanks especially to Justin Browne at MSU for programming help and instruction. Most of all I would like to thank my friends and family: Lynne Schwabe, the Holly-Grimes family, Denise Dicks, Chad Balcom, and my sister Krista, for all sharing my sense of humor and never ditching me even though I was always studying. And finally I would like to thank my LSU friends: Ed Montiel, Alison Dreyfuss, Chris Johnson, Kelsie Krafton, Kundan Kadam, Kat Munley, and Jonny Olson. I never, ever would have made it through this without you guys keeping me sane. Thank you to the Louisiana Space Consortium (LaSPACE) under NASA grant No. NNX10IA40H, and the Dr. Charles E. Coates Memorial Fund for financial assitance. This work benefited from support by the National Science Foundation under Grant No. PHY-1430152 (JINA Center for the Evolution of the Elements). The author's research assistanceship was provided under the Department of Energy Grant DE-FG02-96ER40978, PI's Catherine Deibel and Jeff Blackmon.

Table of Contents

Abstract

Type I X-Ray bursts (XRB's) are a site of nucleosynthesis for some proton-rich elements up to A=100. These stellar explosions occur on the surface of a neutron star in a Low-Mass X-ray Binary accreting H- and He-rich material. During accretion nuclear burning occurs through stable processes such as the hot CNO (HCNO) cycles, but at some critical accretion condition the the HCNO cycles are bypassed through a breakout reaction. This triggers the thermonuclear runaway of the XRB. During the burst, nucleosynthesis on certain proton-rich nuclei, called (α, p) waiting points, can stall which could stall the energy generation and diminish the light curve. These waiting-point nuclei, such as ^{34}Ar, are in $(p, \gamma) - (\gamma, p)$ equilibrium due to their low $Q_{(p,\gamma)}$ values, and do not immediately β^+ decay due to long half lives, but the (α, p) reaction may provide a path to break out of the waiting point.

We performed proton elastic scattering by ^{37}K to study the compound nucleus ^{38}Ca, at the National Superconducting Cyclotron Laboratory using a 4.448 MeV/u beam of ^{37}K incident on a 30 μm-thick polypropylene target. This was done over 13 days with detector equipment designed and built at Louisiana State University. Scattered protons were measured in telescopes of Si strip detectors, while heavy recoils were detected in a gas-filled ionization chamber. An R-matrix analysis of the measured scattering cross section calculated properties of resonances in ^{38}Ca that are important for determining the ^{34}Ar$(\alpha, p)^{37}$K reaction rate. This analysis found spin assignments for 11 resonances, of varying levels of confidence. Four states were identified as 2^+ with high confidence, along with an additional resonance not discovered by previous work. The quantities determined by this analysis were used to calculate a reaction rate.

This rate was input in stellar evolution models built with the software MESA. A 1D model mimicking the "Clocked Burster" GS 1826-24 was evolved using the standard

REACLIB reaction rate and the rate factor found in this work. The observables were then compared with a baseline and to observational results.

Chapter 1
Introduction

Hydrogen, helium, and some lithium were created in the Big Bang. All of the isotopes in the universe created after the Big Bang are made in stars and stellar events through nuclear processes. Helium production continues to dominate the stellar nucleosynthesis processes, since H is the primary fuel of the main sequence of the stellar life cycle, a phase common to all stars. As a result, H and He are by far the most common elements in the universe (Fig. 1.1). Some elements up to Fe are also created in much smaller quantities after the main sequence. Beyond this, there are still many open questions regarding nucleosynthesis sites. Only one third of the lithium predicted by Big Bang nucleosynthesis models is extant in our observations which otherwise well match predictions for isotopes of H and He. Where is the lithium? We think we know most of the processes that create elements outside the main sequence, but we still dont know where all those processes occur. Where does the rapid neutron capture process (r-process) occur that creates approximately half of the heavy elements? What is the nuclear equation of state for the degenerate matter at the core of the NS? These are a few of the questions that nuclear astrophysics seeks to answer. The stellar main sequence is generally well studied so now we look to less common stellar environments such as white dwarfs, core-collapse supernovae, and neutron stars to understand their nucleosynthesis. XRB's and NS's are currently being studied intensely to help identify the details of their various nucleosynthetic processes.

The goal of nuclear astrophysics, then, is to understand and explore the nuclear processes and events of stellar burning, and to connect these processes to phases of the stellar life cycle, and to the elemental abundances observed. When speaking of elemen-

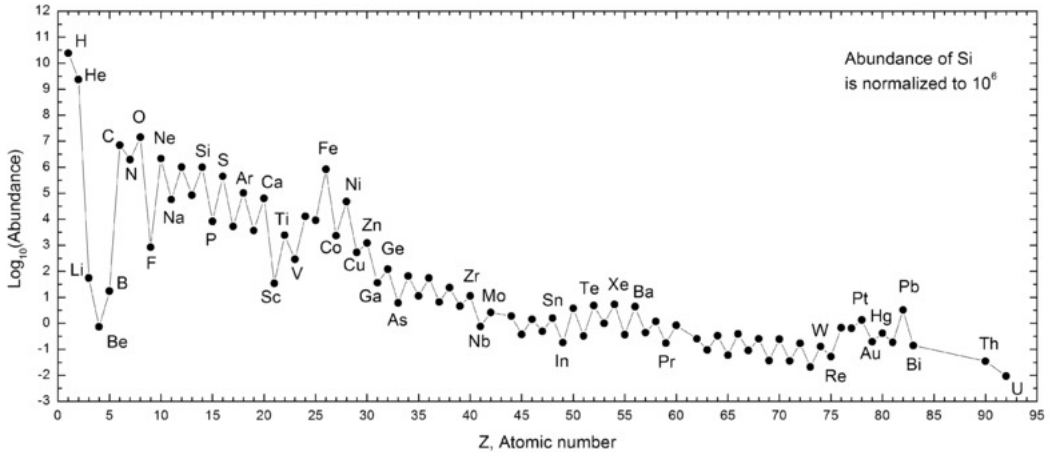

FIGURE 1.1. Elemental abundance number density in the solar system normalized to $n_{Silicon} = 10^6$ taken from [1].

tal abundances we refer to our local space, the Solar System, and what we can observe in our galaxy. Our information about the elemental and isotopic composition of the Solar System comes from several places. First and foremost is the sun. It is by far the largest object in the Solar System and thus is most of the matter. We get composition information from stars such as our sun via spectroscopy to assemble an overall picture of the total abundances (Fig. 1.1). Then there are those sources here on Earth; the material all around us, meteors that fall to Earth, and recently samples brought back by space missions, that help identify isotopic abundances. For more exotic nucleosynthesis we look to spectroscopy of remote sources.

Type I X-ray Bursts (XRB's) are the most common stellar explosions in the Galaxy. Discovered independently in 1976 by Grindlay *et al.* & Belian *et al.* [2] [3], they are unique astrophysical environments. XRB's are known to occur on Low-Mass X-ray Binaries, which are Neutron Star (NS) systems with a low-mass companion, $< 1\ M_{\odot}$. There are around 200 of these systems known, but at present only around half are known to exhibit bursts [4] [5]. They are brief, typically lasting less than 100 seconds. These explosions are highly energetic, expelling up to 10^{40} ergs of energy. XRB nucleosynthesis can create nuclei up to A=100 [6], although there is no known mechanism by which the

XRB material joins the interstellar medium. XRB light curves are difficult to observe from Earth and they occur on a star whose very physical nature is uncertain, but they can help us understand certain nuclear processes, and the equation of state of the underlying NS, so they are heavily studied in many fields of astrophysics. The study of XRB's is a multi-disciplinary activity combining astronomical observation, nuclear experiment, nuclear and astrophysical theory, and cross-disciplinary computational modelling.

Astronomical observations obtained by telescopes provide the link between theory, experiment, and computational models. The Rossi X-ray Timing Explorer, the Fermi Gamma-ray Space Telescope, and the Chandra X-ray observatory search for X-ray sources to identify low-mass X-ray binaries (LMXBs) and their signature outburst, the XRB. The improved X-ray observing capabilities provided by the Rossi X-ray Timing Explorer (RXTE) and the Chandra observatory are responsible for most of the existing catalogue of known bursters [4]. New X-ray telescopes, such as NuStar, by NASA, will hopefully expand our knowledge of LMXB's and XRB's. However, observations of XRB's are characterized by photons in the X-ray spectrum, which are not visible on Earth due to atmospheric interference. Thus we must rely on space based observatories. This limits the amount of data collected since there are only a few telescopes with this capability and there is a high demand for observing time. The current XRB observations show light curves with features such as length, amplitude, and shape, that can vary widely and have anomalous small scale features like oscillations and local troughs.

The aim of experimentally studying nuclear reactions in the astrophysical regime is to determine reaction rates. Studying X-ray bursts in the laboratory involves examining the reactions that power them through nuclear experiments performed using accelerator facilities. Recent important experimental developments in low-energy nuclear physics include the improved ability to create beams of radioactive ions, like ^{37}K, as well as increasingly dense gas targets through cooling and compression. Detection capabilities

are also improving thanks to general technological innovation, like advancements in electronics and silicon fabrication. The analog components upon which the field was previously reliant were prone to signal loss and noise, while digital components are far more compact, reliable, and faster. Meanwhile the silicon detectors which are prevalent in nuclear physics have benefitted from the advancements in Si wafer fabrication (purity, crystal purity, doping accuracy, crystal size, etc.) that have accompanied the onset of the digital age. But X-ray bursts involve hundreds of different reactions, and we can only study them one at a time in the laboratory, so progress is slow and methodical. Often we are unable to study the reaction of interest directly, because the astrophysically-relevant experiments involve low-energies and unstable nuclei. Reaction rates are often calcuated using incomplete nuclear structure information or purely theoretical methods. This can result in large uncertainties in the rate. Of all the reactions that could be important during XRB's very few are presently measured with sufficient precision, but sensitivity studies help us to decide which reactions are most important.

Computational models of stellar bodies and environments have the ultimate goal of representing stellar environments in 3D with fully-coupled physics. As such they are reaping the benefits of the age of big data, with new clusters and massive computing power added to facilities every year. Hundreds of cores and thousands of GB of memory are now available for a single application. Parallelization allows us to create ever larger models, bringing us closer to the goal of 3D fully coupled physics. Despite all this computer models still have their limitations. Limitations in theoretical knowledge trickle down into the models, and thus models still suffer from the lack of an accurate description of the nuclear equation of state in NS's. Multi-body problems have no analytical, closed form solution except for a few exceptional, metastable cases, although the ability to numerically approximate these systems improves constantly. Also, fully-coupled physical models incorporating hydrodynamics, nuclear networks, mixing, as-

troseismology, and other stellar phenomenon, which can only be accurately described with 3-dimensional physics, are limited to approximations of a single radial dimension due to the current capabilities in computing power. The current XRB models show that the rates of some of the unmeasured reactions can change the shape of the light curve as well as the nucleosynthetic path of the XRB and the final elemental abundances [6][7] [8] [9]. These models also reveal information about the underlying NS. We also use the advances in statistical analysis packages to analyze the large data sets resulting from nuclear experimentation.

The goal of theoretical astrophysics is to map the stellar structure and evolution, and identify and constrain the underlying physics. As with all theoretical disciplines, this specialty relies on the new ideas and frameworks designed by great abstract thinkers in order to advance. These frameworks also benefit from the technological advancements of other fields, and they are improved and perfected when observation, experiment, and models are able to test the predictions that result from theoretical efforts. So too the specialty is limited by time to wait for new theoretical developments. Also, some environments such as neutron star cores may never yield to our attempts at experimental duplication and observation.

The present theory of XRB's places them on the surface of a NS, in a binary system with a low-mass companion star. The LMXB designation comprises main-sequence, white dwarf, or red giant companions; however, it is unlikely that all of these have the necessary photospheric composition to produce a burst on the accompanying neutron star [4]. The most likely scenario is a main sequence companion, as it has the necessary H and He abundances. In the bursting system, the companion has expanded outside its gravitational lobe and is losing mass. The two stars are close enough to funnel material from the surface of one star to the other. This material then merges with the NS surface and can undergo stable nuclear burning. However, much of the physics is still not known.

There is no reliable equation of state for NS cores to describe the thermodynamic variables and estimate important quantities like radius and its relationship to the mass. But we are able to place some limits on the mass-radius relationship from observational data and theoretical models to narrow the field of possibilities, as in Steiner *et al.* 2013 [10], depicted in Fig. 1.2.

Even though there are limitations on our knowledge and capabilities, the information we can learn is still immensely useful, and each advancement pushes the field ahead. The end goal is the synthesis of information provided from all these sources to form a cohesive picture of the LMXB system, its underlying stars, the explosive nuclear physics, and the XRB observations.

This work is a study of proton scattering by ^{37}K to examine excited states in the ^{38}Ca compound nucleus of the ^{34}Ar$(\alpha, p)^{37}$K reaction, in order to help constrain the reaction rate. At present there are no published experimental results for the direct reaction in the astrophysically relevant energy regime. The constrained rate will then be used in a model to study its implications for the observables and abundances that characterize the XRB. The experimental portion discussed in Ch. 4 was completed in March 2016 at the National Superconducting Cyclotron Laboratory (NSCL) at Michigan State University. The analysis of the experimental data, discussed in Ch. 5, was completed with the nuclear-particle physics analysis package ROOT, and the AZURE2 R-matrix code. The computational portion, discussed in Ch. 6, was designed using the stellar modeling software MESA and compiled and run in the Louisiana State University (LSU) nuclear-astrophysics Laboratory.

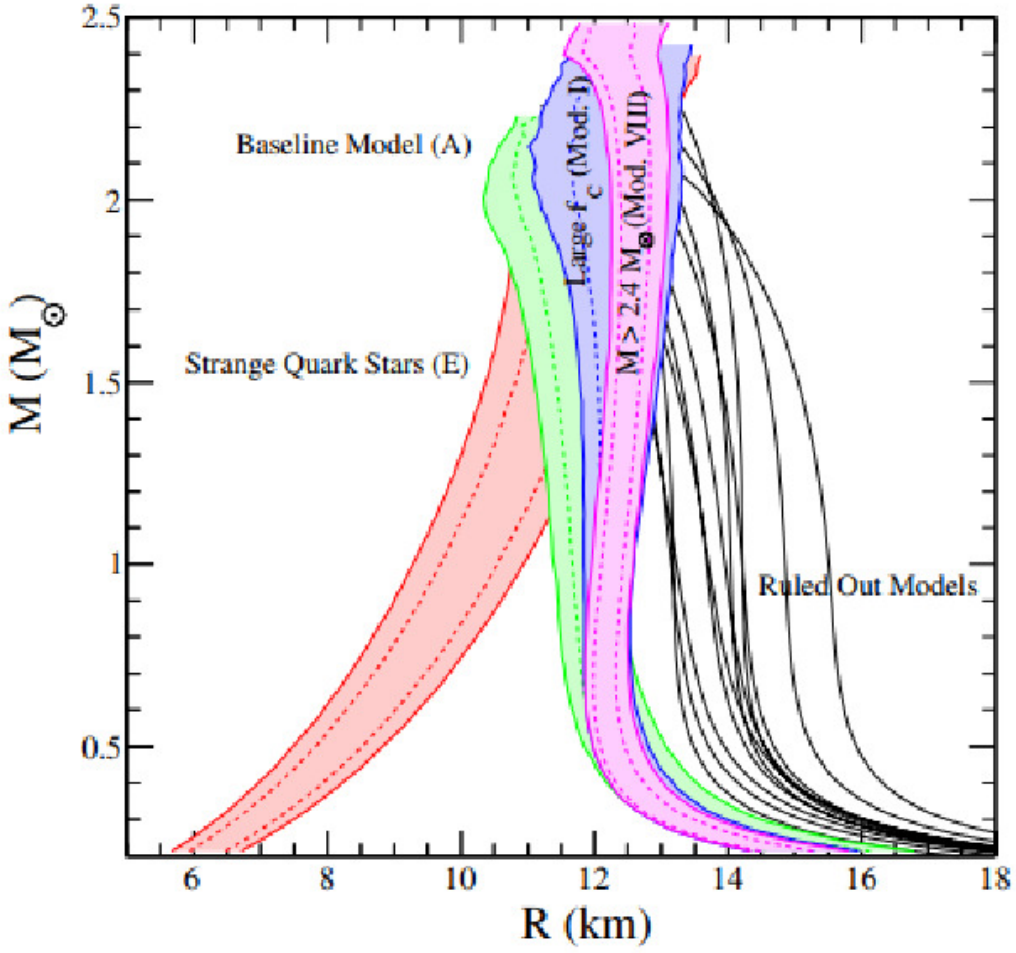

FIGURE 1.2. Possible mass-radius relationships predicted by observations combined with theoretical equations of state. The colors note the theoretical model used, as labeled in the figure [10].

Chapter 2
Motivation and Theory

2.1 Stellar Evolution and the Neutron Star

The life cycle of a star depends on mass and composition, as shown in Fig. 2.1. The first process of H fusion to He signifies the birth of the star and the beginning of the main sequence. The main sequence, which lasts millions to billions of years, is the main phase of stellar evolution and is common to all stars. In general, stars are classified by mass, as this is the primary factor in determining the life cycle of the star, along with initial composition and population. It is in the high-mass stars that we are interested, those having a main sequence mass about 10 $M_{\odot}$, as some of these will become neutron stars. However, lifetime goes inversely with mass so these heavier stars do not spend as much time on the main sequence as low-mass stars. High-mass stars have a life span of only millions of years, versus billions for their low-mass siblings.

During the main sequence stars convert H into He via either the pp chain or CNO cycles, which, like much of the life cycle, depends on mass and initial composition. This is a phase marked by hydrostatic equilibrium within the star. After the main sequence phase the core contracts gravitationally, raising the central temperature and allowing burning to enter various advanced regimes, which generally start with He burning and proceed through successive shells of heavier element burning up to Si [11] [12]. This burning is responsible for producing many heavy elements up to the iron group. For elements heavier than the iron group, the endothermic nature of the production reactions makes them incapable of powering the star, and there is no longer large-scale core nucleosynthesis and thus no energy generation to balance the gravitational pressure [11]. At this point the stars undergo a large scale mass loss event which leads to their final form as depicted in the life cycle diagram Fig. 2.1. In the heavier stars in which we are

interested, this event is a core collapse supernova (CCSN), which is also being explored as a possible site of heavy element nucleosynthesis. After the CCSN, the heaviest stars become black holes, which have a main sequence mass of $15 - 20\ M_{\odot}$ (though this should not be considered an upper limit, stars above this limit exist but are not well understood). These CCSN remnants have masses greater than the Tolman-Oppenheimer-Volkoff (TOV) limit of $1.5 - 3\ M_{\odot}$. However, if the remaining mass is less than the TOV limit the CCSN remnant will be a neutron star. These intermediate mass progenitors have a main sequence mass of $10 - 15\ M_{\odot}$ [13].

2.2 Neutron Star Binaries

Complications are added to neutron star evolution when they are in a binary, like up to 50 percent of the stars in the universe [11]. Two stars in a binary system have a shared gravitational space. Hypothetical lines can be drawn to show surfaces of gravitational equipotential as illustrated in Fig. 2.2. These surfaces create the Roche Geometry, which includes the intersections of several of the equipotential surfaces, known as the Lagrange points. The innermost of the equipotential surfaces that contain both stars is called the Roche Lobe, and the individual bells of the lobe define the space in which the material of each star is contained and constrained by its own gravity. If one star loses mass via a wind or its photosphere expands outside the Roche Lobe due to a dynamic or gravitational event, matter is funneled through the first Lagrange point into the gravitational space of the companion. The material spills into the other bell in a jet, which spirals around the surface of the star parallel to the equatorial plane. As it circles the star, viscosity and other forces absorb angular momentum until the material is slow enough relative to the rotational velocity of the star to join the surface. An idealized version of this disk structure is depicted in Fig. 2.3 [15].

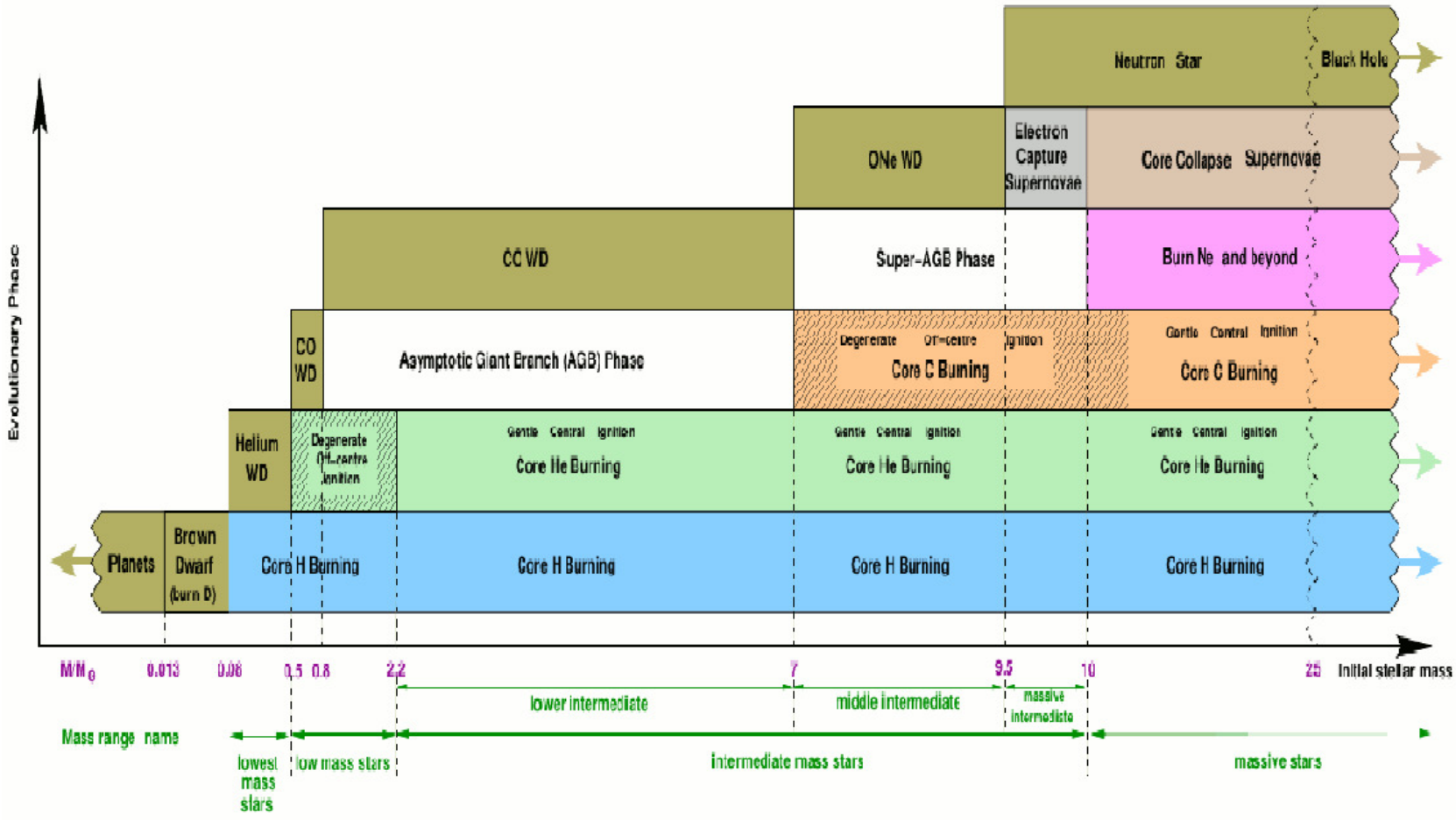

FIGURE 2.1. The stellar life cycle by mass [14].

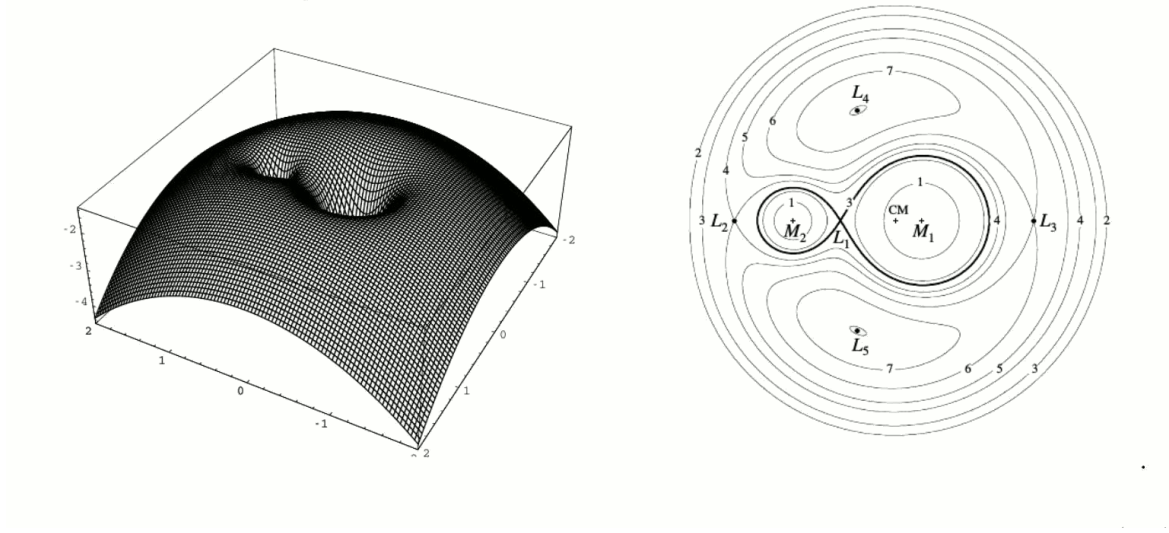

FIGURE 2.2. The Roche Lobe Geometry. The left figure shows one equipotential-surface in 3D. The right figure shows a countour plot of a 2D slice of the equipotential geometry, with M1 being the more massive star and M2 the companion. The innermost surface that surrounds both, known as the Roche Lobe, is shown in bold. The Lagrange points are labeled L1-L5, with L1 being the saddle point that funnels matter from one bell of the lobe to the other [15].

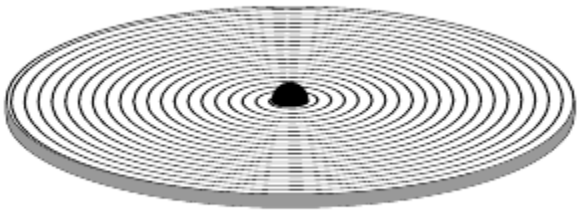

FIGURE 2.3. An idealized visualization of the accretion disc with material spiraling toward the surface [15].

2.3 X-ray Burst Observables

X-ray binaries are marked by their persistent X-ray flux, caused by infalling matter releasing its gravitational potential as light in the X-ray regime. During the X-ray burst, the nucleosynthesis in stars is responsible for the release of photons via emission or thermal excitation, so during the explosive behavior a strong peak in X-ray emissions can be observed. This is known as an XRB light curve, and is one of the defining measurables used to explore them. These light curves are characterized by a sharp rise in the baseline over a period of a few seconds with a slow exponential decay. They last around 10-100 s and recur on a period of hours to days. And most relevant to the nucleosynthesis, they release $10^{39} - 10^{40}$ ergs of energy and reach peak temperatures of 2 GK. Figure 2.4 shows sample bursts from three different sources.

Spectral lines are also usually important for characterizing stellar phenomena, and we do observe a few in the LMXBs and during outburst, but it is thought that the spectral lines observed during XRBs, such as the H- and He-like Fe absorption lines, are from photons interacting with the accretion disc. Though they are probably not informative of the composition of the NS surface, they do reveal details about the accreted matter, and, consequently, the companion. They also provide gravitational redshift information, which helps constrain the mass-radius relationship [17].

2.4 Neutron Star Nucleosynthesis and the X-ray Bursts

The XRB is powered by runaway nucleosynthesis. In a LMXB, if the companion star is a main sequence or red giant star, the material is H and He rich. The accretion layer structure is shown in Fig. 2.5. Due to the intense gravitation of the neutron star, the conditions on the surface are favorable for nuclear burning, and this takes the form of the pp and CNO cycles, much like in the main sequence star itself [18]. The Hot CNO (HCNO) cycles dominate the burning in NS conditions. There are 3 such HCNO cycles, and each has an isotope whose β decay lifetime limits the rate of burning [11].

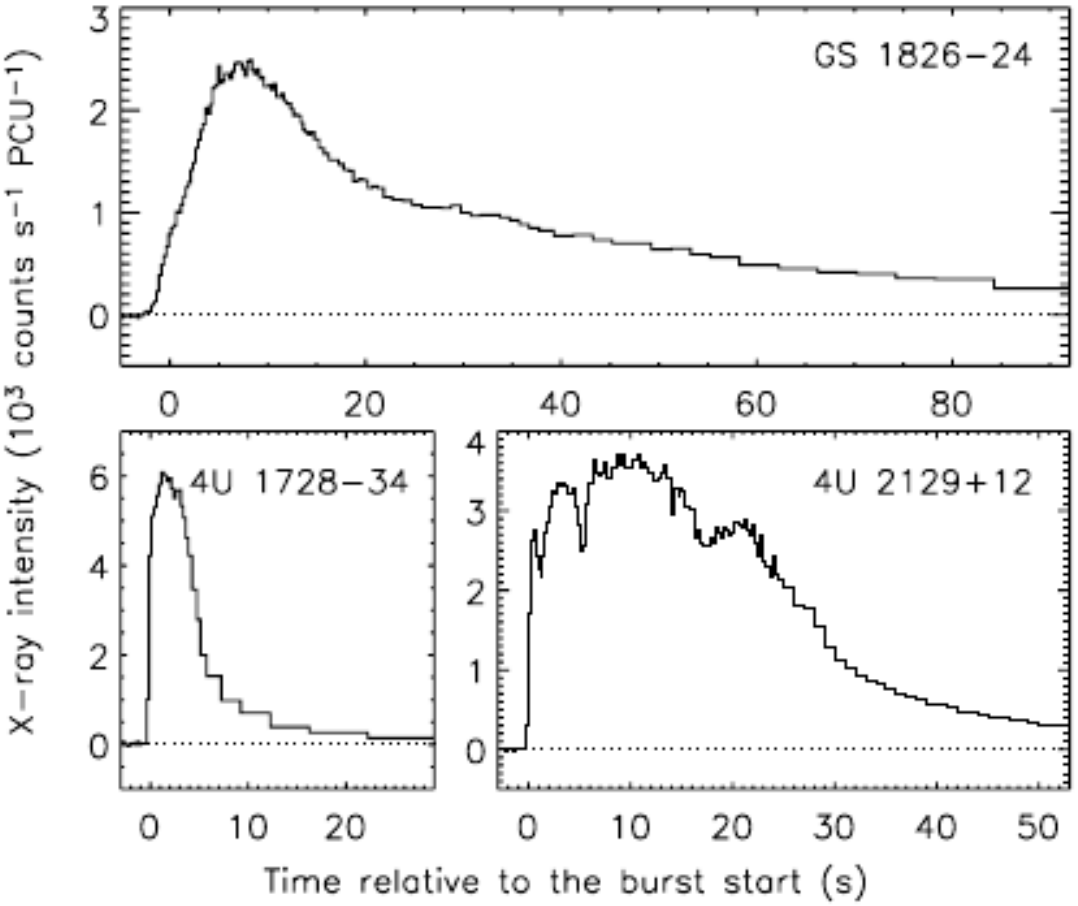

FIGURE 2.4. Sample bursts from three sources, Galloway *et al.* [16].

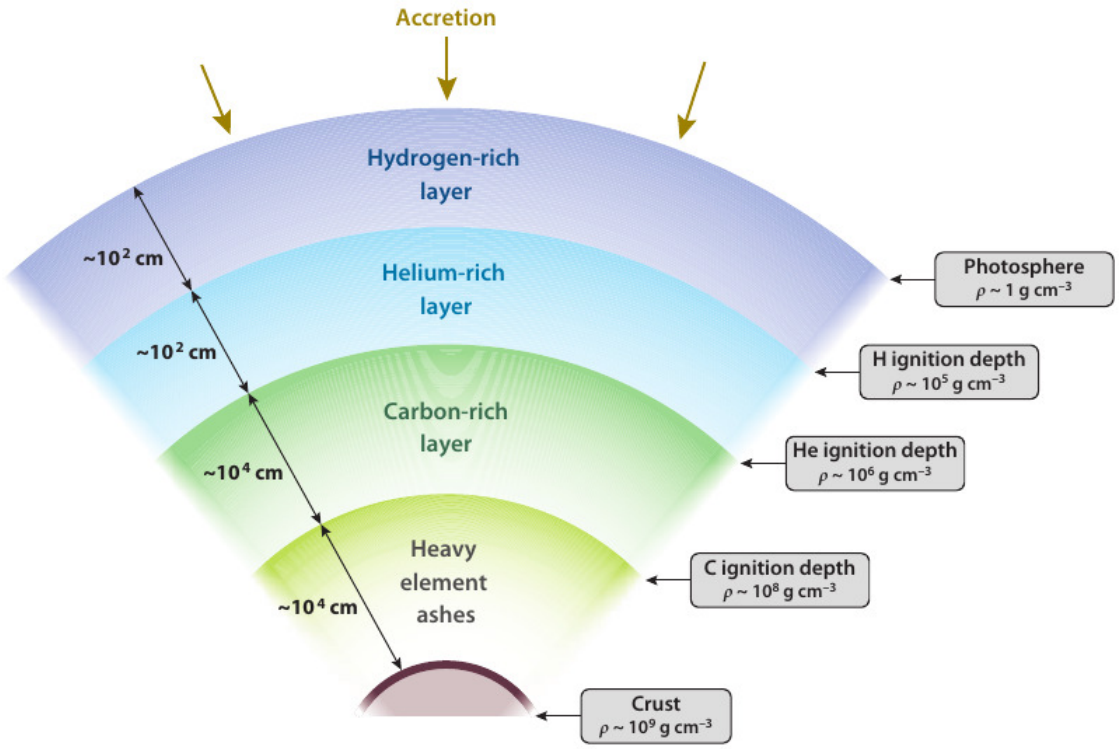

FIGURE 2.5. The structural layers of an accreting neutron star taken from Watts 2012 [19].

If accretion reaches some critical fraction of the Eddington limit, between .01 an .3, which depends on the mass and composition of the two stars [19], temperature and pressue increase and the HCNO cycles are visited before breaking out into the runaway nucleosynthesis of the XRB.

HCNO I:

$$^{12}C(p,\gamma)^{13}N(p,\gamma)^{14}O(\beta^{+}\nu_{e})^{14}N(p,\gamma)^{15}O(\beta^{+}\nu_{e})^{15}N(p,\alpha)^{12}C \tag{2.1}$$

The time-limiting β decay in HCNOI, seen in Fig. 2.6, are ^{14}O ($T_{1/2}$=70.61 s) and ^{15}O ($T_{1/2}$=122.24 s), and these lead to a bottleneck and a buildup of these isotopes. When there are O^{16} seed nuclei present, another cycle can occur, possibly concurrently to HCNOI, that of HCNOII:

$$^{16}O(p,\gamma)^{17}F(\beta^{+}\nu_{e})^{17}O(p,\gamma)^{18}F(p,\alpha)^{15}O(\beta^{+}\nu_{e})^{15}N(p,\gamma)^{16}O \tag{2.2}$$

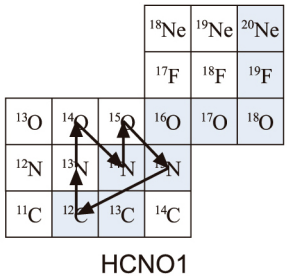

FIGURE 2.6. The Chart of Nuclides representation of HCNOI [11].

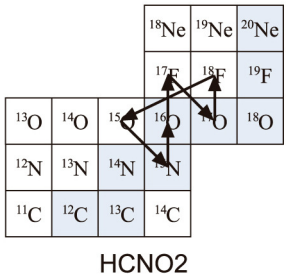

FIGURE 2.7. The Chart of Nuclides representation of HCNOII [11].

The time limiting β in HCNOII, seen in Fig. 2.7 is ^{17}F ($T_{1/2}$=64.49 s). The $^{17}F(\beta^+\nu_e)^{17}O$ process may be bypassed in favor of $^{17}F(p,\gamma)^{18}Ne$, leading to HCNO III:

$$^{16}O(p,\gamma)^{17}F(p,\gamma)^{18}Ne(\beta^+\nu_e)^{18}F(p,\alpha)^{15}O(\beta^+\nu_e)^{15}N(p,\gamma)^{16}O \tag{2.3}$$

For HCNOIII, seen in Fig. 2.8, the time limiting β of this cycle, ^{15}O and ^{18}Ne, represent the final hurdle to escape the stable burning of the HCNO cycles altogether. After reaching HCNOIII, conditions become favorable for a He shell flash. The triple-alpha reaction ($3\alpha \rightarrow ^{12}$C) becomes favored and occurs briefly in a thin shell instability, where thermal energy released by thermonuclear reactions cannot be dissipated through stellar expansion or cooling as originally described by Hansen & Van Horn 1975 [20], that is, thermodynamic conditions are not relieved by the flash of nucleosynthesis. This flash provides a burst of energy to bypass HCNOIII via a breakout reaction, and pushes thermodynamic conditions into XRB values.

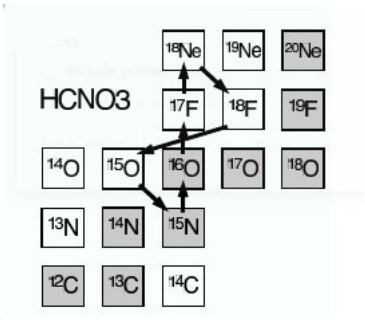

FIGURE 2.8. The Chart of Nuclides representation of HCNOIII [11].

Depending on temperature, this reaction will be either $^{15}\mathrm{O}(\alpha,\gamma)^{19}\mathrm{Ne}$ or $^{18}\mathrm{Ne}(\alpha,p)^{21}\mathrm{Na}$, with the latter operating at higher temperature regimes. This is known as a "breakout" reaction because it provides a pathway out of the HCNO cycles and into the runaway nucleosynthesis of the XRB. Following breakout, during the early times of the burst, nucleosynthesis is dominated by the αp process, a series of (α, p) and (p,γ) reactions, and this drives the rise of the burst light curve. Then the nucleosynthesis proceeds into the rp process, or rapid proton capture process, which is an uneven series of radiative proton captures and β^+ decays that correspond to the decay of the burst light curve. The nucleosynthesis can proceed as high as A=100, depending on various factors such as the ash composition, accretion rate, and previous bursts. In any case, the burst cannot proceed past the Sn-Sb-Te cycle, which was found in Schatz *et al.* [6] to be the limiting cycle. The nuclei created during the burst are proton rich, and during the final phase of the burst they decay towards stability. Figure 2.9 depicts one possible path for the XRB nucleosynthesis and its series of reactions [17]. A combination of accretion composition and burst ash composition can cause the surface to vary in H, He and C ratios and this can affect the depth of the burst ignition as well as the shape of the light curve, length, and final abundances of the burst [17][9].

2.5 XRB (α, p) Process Waiting Points

Waiting points are important nuclei in XRB nucleosynthesis. Due to either thermodynamic and/or nuclear conditions, the reaction flow is restricted and nucleosynthesis

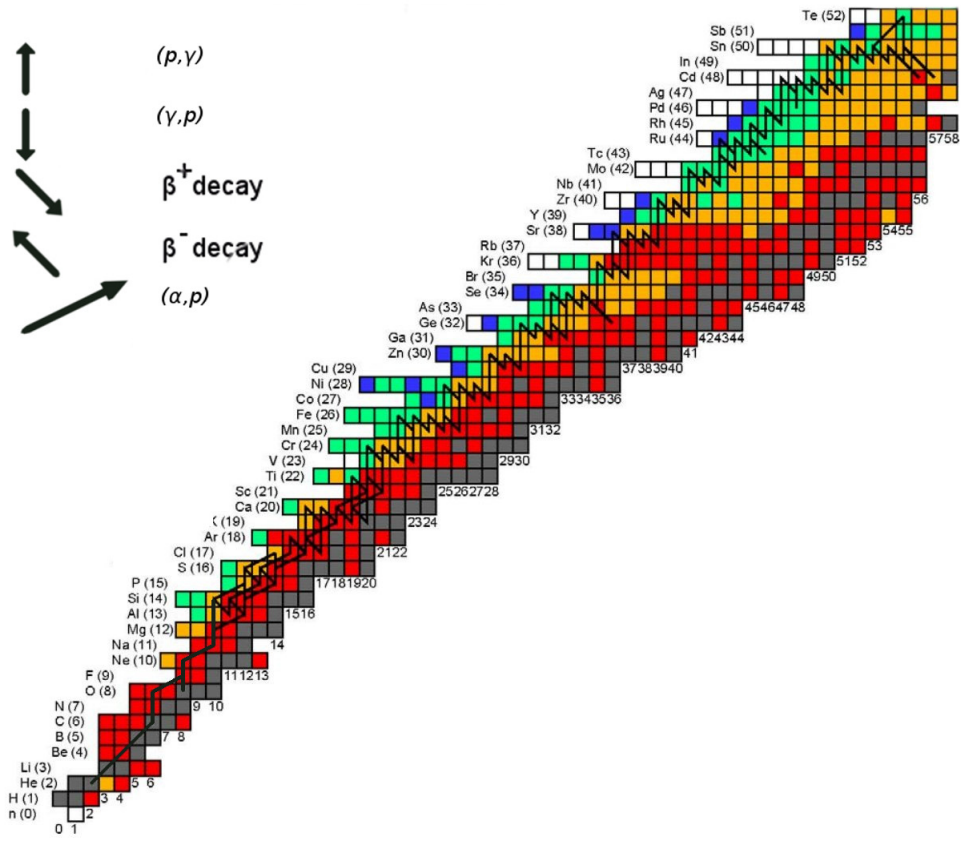

FIGURE 2.9. A simulated possible path of XRB nucleosynthesis taken from Schatz *et al.* [17] and labeled with reaction arrows.

stalls. The (α, p) waiting points occur during XRB's on even-even, low $Q_{(p,\gamma)}$-value nuclei, with (Z-N)/2=-1. The (radiative) proton captures that dominate during the XRB are favored and occur readily on the waiting-point nuclei, but, due to the low $Q_{p\gamma}$-value, this process is in equilibrium with the corresponding photo-disintegration ((p, γ)-(γ, p) equilibrium), resulting in repeating cycle between the two. The proposed (α, p) waiting points are ^{22}Mg, ^{26}Si, ^{30}S, ^{34}Ar, and sometimes ^{38}Ca [8] [9], and this work is interested in the ^{34}Ar waiting point. A β^+ decay, $^{34}\text{Ar}(\beta^+\nu_e)^{34}\text{Cl}$, might occur that would break out of the equilibrium, but these waiting point nuclei have long lifetimes relative to the short time scale of the burst. Under other circumstances the β^+ decay channel lifetime of ^{34}Ar $T_{1/2}$=.84 s is sufficient to allow this path to dominate. Since the nucleosynthesis is responsible for the observed light curve during the XRB, such a stall may also restrict the corresponding photon emission. During the burst, increasing temperature can provide an alternative, (α, p) path that can offer a detour out of the stalled nucleosynthesis, to continue the burst (Fig. 2.11). This is the motivation to study $^{34}\text{Ar}(\alpha, p)^{37}\text{K}$. This could also help explain the enigmatic double peaked bursts evident in 4U 1636-56 [16] (Fig. 2.10). Other possible explanations include quasi-periodic oscillations, localized burning, and photospheric radius expansion [8].

2.6 ^{34}Ar$(\alpha, p)^{37}$K Nuclear Theory

Compound nuclear reactions consist of several phases. First, is the incoming channel, which refers to the reactants, or the initial particles or nuclei. In an experimental setting, these are the projectile and the target. Next, for a very brief time, the system of compound reactions exists as the compound nucleus, that has the combined Z and N of the reactants. Finally, the system terminates in an exit channel, which refers to the compound nucleus decay products, such as an emitted light particle and the heavy daughter nucleus. The entrance channel for this reaction finds both reactants, $^{34}\text{Ar}+\alpha$, in their ground states. The compound nucleus, ^{38}Ca, due to conservation of energy, must be in

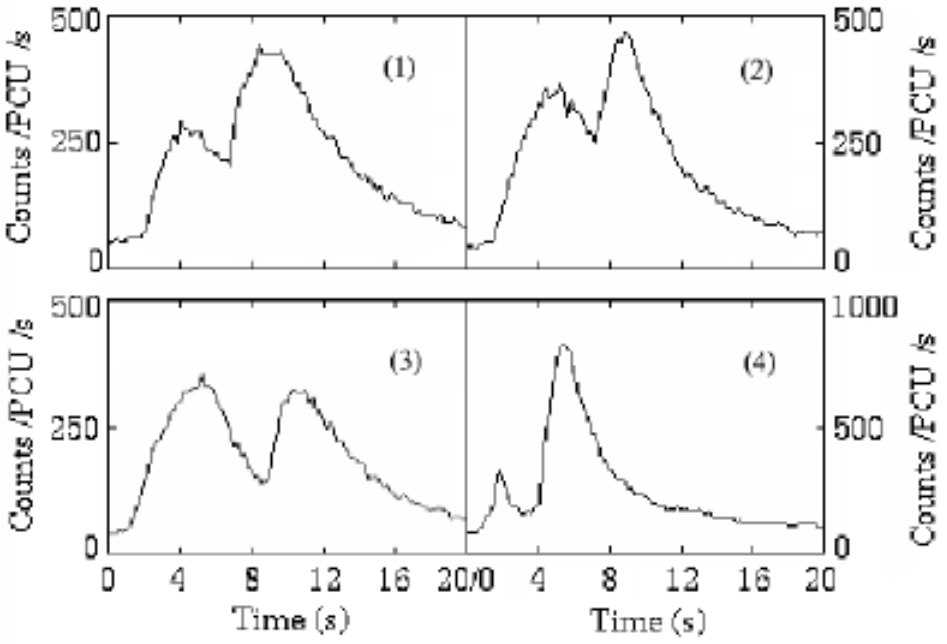

FIGURE 2.10. Double peaked bursts observed in 4U 1636-536, from [21].

.

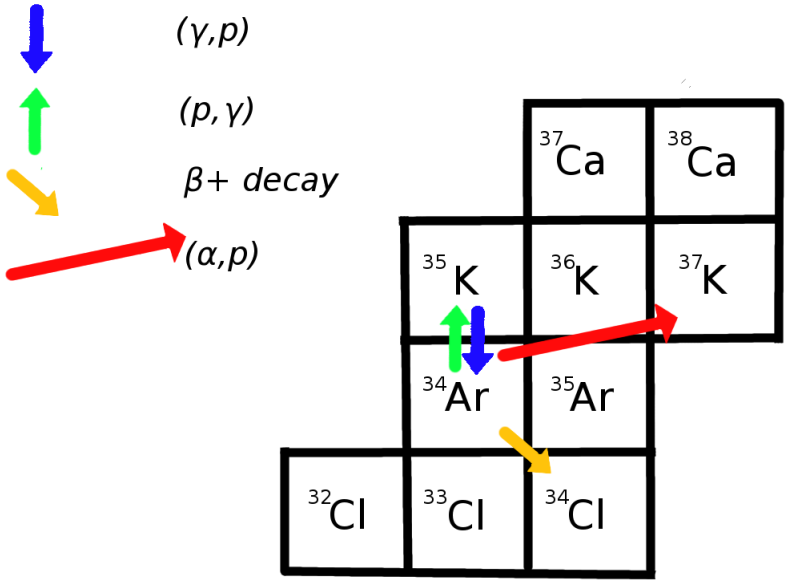

FIGURE 2.11. Graphical representation of waiting point nucleosynthesis on ^{34}Ar.

an excited state while the daughter, the heavy product ^{37}K in the ^{37}K+p exit channel, can also be in an excited state as well as the ground state.

In order to fuse with the nucleus the incoming particle must overcome the Coulomb force and be bound by the strong force. However, very few stellar environments provide the high temperature/energy required for this. Fortunately, quantum mechanics tells us that there is always some statistical probability that a particle at a given energy can spontaneously tunnel through a force barrier such as the Coulomb potential.

The quantity known as the reaction rate is the probability of a reaction between two particles in a stellar plasma, in units of reactions per time per volume. To build this function we construct a probability weighted average, starting with a function known to depend on the relative velocities of the particles, known as cross section, given by

$$\sigma(v) \equiv \frac{(N_R/t)}{[N_b/(tA)]N_t}. \tag{2.4}$$

This is a quantitative measure for the interaction probability, where, assuming the beam is narrower than the target

$N_R/t = \frac{\text{(interactions)}}{\text{(time)}}$,

$N_b/(tA) = \frac{\text{(incident particles)}}{\text{(area*time)}}$,

and

N_t = (areal density of target atoms). We can rearrange this to isolate the quantity we will later define as reaction rate: r, interactions per time per volume:

$$r = \frac{N_R}{Vt} = \sigma \frac{N_t}{V} v \frac{N_b}{V}. \tag{2.5}$$

If the quantity$N_i = \frac{N_{m_i}}{V}$ is the number density of species i, then the reaction rate between particles 0 and 1 is

$$r_{01} = N_0 N_1 \nu\sigma(\nu). \tag{2.6}$$

To define this in terms of a more convenient quantity, we convert Eq. 2.6 from a velocity dependent function into a function of energy. In the nuclear environment of the stellar plasma, particle motion is non-relativistic, so we can invoke the Maxwell Boltzmann distribution,

$$P(E)dE = \frac{2}{\sqrt{\pi}} \frac{1}{(kT)^{3/2}} \sqrt{E} e^{-E/kT} dE, \tag{2.7}$$

as the probability density function P(E), of a nucleus' kinetic energy in an astrophysical environment of temperature T, and where k is the Maxwell-Boltzmann constant, and E is the center-of-mass energy of the system in MeV. Then the reaction rate is the expected value of the product of velocity and cross section σ, weighted by the probability density of E, P(E), both converted to functions of energy. The reaction rate is the integral equation:

$$N_A < \sigma\nu >_{01} = N_A \left(\frac{8}{\pi m_{01}}\right)^{1/2} \frac{1}{(kT)^{3/2}} \int_0^\infty E\sigma(E) e^{-E/kT} dE \tag{2.8}$$

where N_A is Avogadro's number, m_{01} is the reduced mass, and T is the temperature. This is still in a generalized form for any type of reaction, to specify for a given reaction we must further define the quantity σ. For the nonresonant contribution for charged-particle reactions, we treat the cross section in terms of the transmission probability for s-waves through the Coulomb barrier, approximated as a spherical potential. We invoke the Gamow factor (a quantity derived elsewhere), for this probability

$$\hat{T} \approx exp\left(-\frac{2}{\hbar} \sqrt{\frac{2m_{01}}{2E}} Z_0 Z_1 e^2 \right) \equiv e^{-2\pi\eta}, \tag{2.9}$$

where $\hbar$ is the reduced Planck constant, and Z_0 and Z_1 are the proton numbers of the incoming particles. The quantity in the exponent of the right hand side of this equation, $2\pi\eta$, is the Sommerfield Parameter and is found numerically to be

$$2\pi\eta = .0989534 Z_0 Z_1 \sqrt{\frac{1}{E} m_{01}}, \tag{2.10}$$

and we use it to recast the cross section in terms of a new quantity, the astrophysical S-factor S(E) (which we will later assume is constant, S_0 to first approximation), defined by

$$\sigma(E) = \frac{1}{E} e^{-2\pi\eta} S(E). \tag{2.11}$$

We rewrite the non-resonant reaction rate thusly:

$$N_A < \sigma\nu >= \left(\frac{8}{\pi m_{01}}\right)^{1/2} \frac{N_A}{(kT)^{3/2}} S_0 \int_0^\infty e^{-2\pi\eta} e^{-E/kT} dE \tag{2.12}$$

$$= \left(\frac{8}{\pi m_{01}}\right)^{1/2} \frac{N_A}{(kT)^{3/2}} S_0 \int_0^\infty exp\Big(- \frac{2}{\hbar} \sqrt{\frac{m_{01}}{2E}} Z_0 Z_1 e^2 \Big) e^{-E/kT} dE. \tag{2.13}$$

Examining the components of this function, the Coulomb tunneling probability, which goes as

$$P \propto e^{-2\pi\eta}, \tag{2.14}$$

and the probability density function, i.e. the Maxwell Boltzmann distribution, which goes as

$$P \propto e^{-E/kT}, \tag{2.15}$$

we see the peaks generally lie away from each other, but there is a small region of overlap in the high energy and low energy tails of the Maxwell Boltzmann distribution and Coulomb transmission probability, respectively (Fig. 2.12). The maximum of this

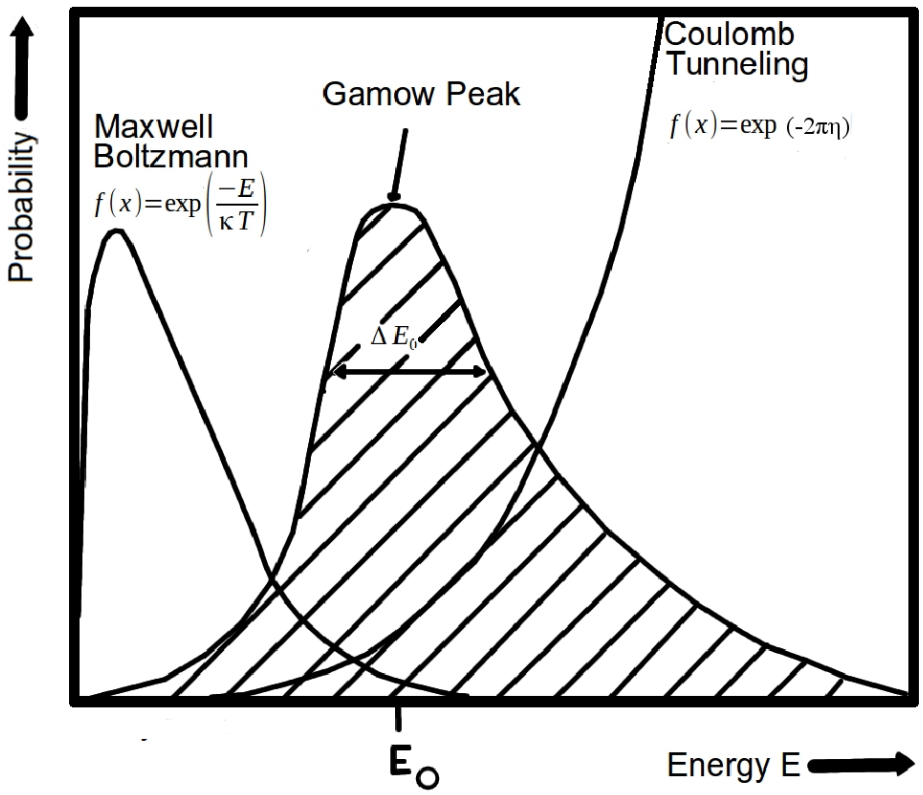

FIGURE 2.12. A visualization of the individual functions that govern the probability of a reaction between two particles The Maxwell-Boltzmann distribution, which predicts the likelihood of finding the incoming particle at energy E relative to the target nucleus, is shown with the S-wave Coulomb transmission probability. The overlap of these two regions is known as the Gamow Window, with the peak notated with E_0 and width ΔE_0.

region, defined as the Gamow Energy, E_0, is found by taking the first derivative of the integrand in Eq. (2.13), and setting it equal to 0 so that

$$E_0 = [\left(\frac{\pi}{\hbar}\right)^2 (Z_0 Z_1 e^2)^2 (\frac{m_{01}}{2})(kT)^2]^{1/3} \equiv 0.1220\left(Z_0^2 Z_1^2 m_{01} T_9^2\right)^{1/3}. \tag{2.16}$$

The width of the Gamow Peak, referred to as the Gamow Window, is found by approximating the combined probability, Eq. (2.13) with a Gaussian:

$$\exp\left(-\frac{2E_0^{2/3}}{\sqrt{E}kT} - \frac{E}{kT}\right) \approx exp\left(-\frac{3E_0}{kT}\right) exp\left[-\left(\frac{E-E_0}{\Delta/2}\right)^2\right], \tag{2.17}$$

and matching the second derivatives of the right hand side and left hand side, giving

$$\Delta = \frac{4}{\sqrt{3}}\sqrt{E_0 kT} = .2368\left(Z_0^2 Z_1^2 m_{01} T_9^5\right)^{1/6}. \tag{2.18}$$

Using Eqs. 2.16 and 2.18 at XRB peak temperature, $T_9 \approx 2$, gives a Gamow peak value for the $^{34}\mathrm{Ar}(\alpha, p)^{37}\mathrm{K}$ reaction of $E_0 = 3.23$ MeV, and the Gamow window 2.37 MeV$< E_{c.m.} <$ 4.09 MeV. Since energies in the stellar environment are rarely high enough to overcome the Coulomb barrier altogether, this region is enough to supply all the nucleosynthesis needs of the stellar environment [11].

We can distinguish charged-particle cross section contribution equations by their smoothness over the astrophysical temperature regime. The compound nucleus can only form in specific quantum states, and so in general the cross section increases energies that are accessible to these states. If these states are plentiful, broad, and distributed regularly across the energy range, the cross section will appear as a smooth function. If these states are few and narrow, the result is a narrow resonant cross section, which rises sharply at localized regions where energies correspond to the excited states of the compound nucleus. When these states are above the energy threshold of the combined mass energy value of the entrance channel reactants, they are called resonances, and the theory and equation of these cross sections takes its name from this fact. In this case, we invoke the Breit-Weigner equation for a single resonance level:

$$\sigma = \omega\frac{\lambda^2}{4\pi}\frac{\Gamma_0\Gamma_1}{(E_r - E)^2 + \Gamma^2/4}, \tag{2.19}$$

where λ is the De Broglie wavelength, $2\pi\hbar/\sqrt{2m_{01}E}$, Γ_0 and Γ_1 are the resonance partial widths of the entrance and exit channels, while Γ is the total width of the resonance, and E_r is the resonance energy. This equation comes from an extensive derivation of transmission probabilities through the Coulomb barrier, which can be found in [11]. This

equation includes the quantity ω, which is derived from the "g" factor or multiplicity to account for relative spin probabilities:

$$\omega \equiv \frac{(2J_r + 1)(1 + \delta_{01})}{(2j_0 + 1)(2j_1 + 1)}, \tag{2.20}$$

where J_i is the spin, and δ_{ab}, the Dirac delta function, is included to account for identical particles. So

$$\sigma = \frac{\lambda^2}{4\pi} \frac{(2J_r + 1)(1 + \delta_{01})}{(2j_0 + 1)(2j_1 + 1)} \frac{\Gamma_0 \Gamma_1}{(E_r - E)^2 + \Gamma^2/4}. \tag{2.21}$$

Combining this with equation 2.8 where we defined the reaction rate as a probability weighted function, we construct the integral:

$$N_A < \sigma\nu >_{01} = N_A \frac{\sqrt{2\pi}\hbar^2}{(m_{01}kT)^{3/2}} \omega \int_0^\infty \frac{\Gamma_0 \Gamma_1}{(E_r - E)^2 + \Gamma^2/4} e^{-E/kT} dE. \tag{2.22}$$

Over narrow resonances, we can assume a relatively constant value for the partial widths and Maxwell-Boltzmann factor $e^{-E/kT}$, and the rate for a single resonance becomes

$$N_A < \sigma\nu >_{01} = N_A \frac{\sqrt{2\pi}\hbar^2}{(m_{01}kT)^{3/2}} e^{-E_r/kT} \omega \frac{\Gamma_0 \Gamma_1}{\Gamma} 2\pi \tag{2.23}$$

and for the total resonant reaction rate we sum over all resonance levels,

$$N_A < \sigma\nu >_{01} = N_A \left(\frac{2\pi}{(m_{01}kT)} \right)^{3/2} \hbar^2 \Sigma_i (\omega\gamma)_i e^{-E_{r_i}/kT} \tag{2.24}$$

where $(\omega\gamma)_i = (\omega \frac{\Gamma_0 \Gamma_1}{\Gamma})_i$, and i is an index over resonances. Thus the variable quantities in this equation are those we hope to calculate using the experimental data contained in this work:

E_r, which is the resonance energy,

Γ_0 and Γ_1 which are the particle partial widths,

Γ, which is the total resonance width, and

$\vec{J} = \vec{L} + \vec{S}$, which is the spin state of a given level.

Returning to our reaction of interest, ^{34}Ar$(\alpha, p)^{37}$K is an α particle capture on a ^{34}Ar nucleus. An α particle is the fully ionized ^{4}He nucleus, while ^{34}Ar is a proton-rich unstable isotope of argon (Z=18) with a half life of $T_{1/2}$ = 844.5 ms. Thus it is radioactive, with β^+ decay (emission of a positron and electron neutrino) to ^{34}Cl (Z=17) as its only decay mode (which then β^+ decays to the stable ^{34}S (Z=16)). The combination of ^{34}Ar and an α particle make the compound nucleus ^{38}Ca. Since the incoming particle is an α particle, the compound nucleus must form at an excited energy state above the α threshold, at 6.105 MeV, or the sum of the mass energies of the nucleus and α particles in their ground states minus the ^{38}Ca compound nucleus mass energy. Above this threshold the reaction is more likely to occur at or near resonant states of the compound nucleus. The proton emission from these excited states can occur to the ground state or any of the allowed excited states of the daughter nucleus, and each of these exit channels may contribute to the reaction rate.

Returning to Eq. s2.24, the quantity ω, $j_a = j_\alpha = 0$ and $j_b = j_{^{34}Ar} = 0$, and $\delta_0 = 0$. For the quantity $\frac{\Gamma_0\Gamma_1}{\Gamma}$, $\Gamma_0 = \Gamma_\alpha$, $\Gamma_1 = \Gamma_p$, and $\Gamma = \Gamma_\alpha + \Gamma_p + \Gamma_\gamma$. The latter quantity, Γ is dominated by the proton-partial width, Γ_p, which forces the quantity $\frac{\Gamma_p}{\Gamma} \approx 1$. Thus our reaction equation simplifies to

$$N_A < \sigma\nu >_{01} = N_A\left(\frac{2\pi}{(m_{01}kT)}\right)^{3/2}\hbar^2\Sigma_i(2J_i + 1)\Gamma_{\alpha_i}e^{-E_{r_i}/kT} \tag{2.25}$$

or the numerical approximation

$$N_A < \sigma\nu >_{01} = 1.54x10^{11}(\mu T_9)^{-3/2}\Sigma_i(2J_i + 1)\Gamma_{\alpha_i}e^{-11.605*E_{r_i}/T_9}. \tag{2.26}$$

It is this equation that will ultimately be used in our final reaction rate calculation.

Chapter 3
Previous Work

3.1 Sensitivity Studies

Sensitivity studies are particularly useful in guiding the experimental work of nuclear astrophysics. A stellar model using MESA, KEPLER, or private stellar evolution software, models the structure, composition, and nuclear network equations of a star. The star is evolved over time, and reaction rates are varied by a factor to examine features of interest such as the nuclear reaction network evolution and final abundances of the burst, and energy generation and luminosity to simulate a light curve. This helps determine which rates are important in a given astrophysical environment and guides experimental efforts. If extended or in-depth nucleosynthesis analysis is needed, a profile of the temperature and pressure can be recorded. This profile can be input into nuclear network software such as NUGRID or custom network codes, which focus on a single task: calculating the nucleosynthesis, and thus is able to evolve a much larger network. There are three different sensitivity studies which found $^{34}\mathrm{Ar}(\alpha, p)^{37}\mathrm{K}$ to be important in the context of XRB's.

The first of these three sensitivity studies published was Fisker 2004 *et al.* [8] in an effort to specifically identify the source of the double-peaked burst behavior depicted in Fig. 2.10. This work used the AGILE code in a 1D hydrodynamic simulation with a limited diffusion configuration based on mixing-length theory. The accompanying network included 298 isotopes up to tellurium. Fisker *et al.* computed the light curve resulting from nucleosynthesis models in which two of the 5 potential waiting-point reactions were tested, altering their rate by a factor of 100. The work concluded that $^{34}\mathrm{Ar}(\alpha, p)^{37}\mathrm{K}$ affected the dip in the simulated double-peaked burst and would decrease the magnitude of this feature if the reaction rate were 100 times faster. The luminosity of the second

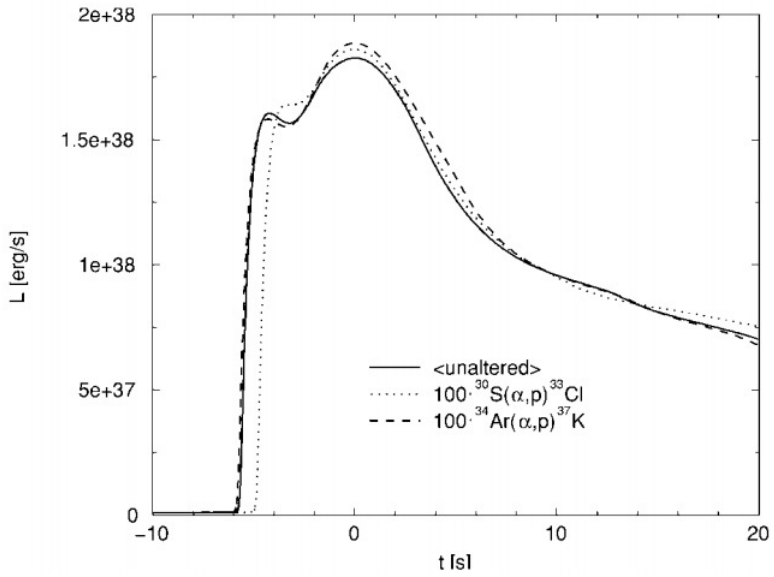

FIGURE 3.1. Computational predictions of the variance in an XRB light curve with rate variances of x100 on two (α, p) reaction waiting points, from [8].

peak also increased with this increase in the rate. The effects of rate variance on the light curve are shown in Fig. 3.1 [8].

In 2008 Parikh *et al.* [7] focused, using two approaches, on a post-processed nuclear network combined with three thermodynamic profiles taken from literature (Schatz 2001 [6], Koike 2004 [22], and Fisker 2008 [8]). The first approach used was a series of models with the somewhat standard process of varying the reaction rates individually by a factor of 10 as a generalized uncertainty value for both experimental and theoretical rates. This is in contrast to the rate variation method used by Cybert *et al.*, discussed in the next section. The second approach of Parikh *et al.* repeatedly ran a single model in which all rates were varied using Monte Carlo simulated values within their uncertainties. One of the goals of this second approach was to test correlations between multiple related rates and the XRB features in question.

The general goal of Parikh *et al.'s* work was to test the impact of these variations on final abundances and energy generation in the XRB. The thermodynamic profiles of Schatz, Koike, and Fisker, were combined with initial abundances taken from the

same sources and input into the nuclear network. To further vary the parameter space, the Koike 2004 profile was altered to achieve target variations of burst duration, max temperature, and metallicity. All other model input values were concurrently scaled, until the target values of burst duration, max temperature, and metallicity, matched the desired output. This produced a total of 10 individual $T - \rho$ profiles-initial abundance combinations to input into the post-processed nuclear networks. The nuclear network was then calculated using custom software with a network that included 606 nuclides, with species up to ^{113}Xe, and all the possible charged-particle and weak reactions that connected them. Neutron capture rates were not included. The $^{34}\mathrm{Ar}(\alpha, p)^{37}\mathrm{K}$ reaction was found to be influential in only one of the 10 models, compared to some reactions found to affect final abundances of some species by factors of 10, or altering the abundances of dozens of different species. However, the results are still intriguing. In the model in question, the Koike 2004 profile was scaled so that the initial abundances possessed a higher metallicity of 0.19 compared with Solar, and $^{34}\mathrm{Ar}(\alpha, p)^{37}\mathrm{K}$ was found to affect the final abundance of ^{34}S by a factor of 0.42. Since this was the sole model that varied metallicity, this may indicate that further models with additional metallicity variations are necessary.

Parikh *et al.'s* work was limited compared to more recent simulations performed only a few years later. At that stage in computational development, there were still significant barriers to fully coupled nuclear networks with stellar structure and composition models. Parikh's work still represents an advancement, however, as it was able to include a large network with a multi-zone approach. Previous work was limited to a choice of one or the other. Computational advancement has progressed quickly in this arena and coprocessed, adaptive networks now allow for fully coupled models, and computational optimization, as well as the feedback between the thermodynamics and nucleosynthesis such as was done by Cyburt *et al.* [9].

The most recent sensitivity study completed was by Cyburt *et al.* in 2016 [9]. Cyburt *et al.* used the stellar evolution package KEPLER to study the effects of varying reactions important to XRB's. They utilized KEPLER on a cluster to model the burst in two phases. Due to the computationally intensive nature of these models, they first used a one zone model in the code ONEZONE to limit the parameter space of the multi-zone model. A single zone assumes a uniform abundance profile and no mixing. In this model they chose 1931 (p,γ), (α,γ) and (α,p) and reactions and varied them individually by a factor of 100 up and down in the single zone code using a decoupled thermodynamic model of an XRB from GS 1826-24, (the Clocked Burster). The factor of 100 was chosen rather than adopting an experimental uncertainty range, where available, to highlight any possible reaction that might be important rather than provide a truly physical picture. The resulting calculated light curves and abundance profiles were compared to determine which reactions had the largest impact. One hundred different reactions were highlighted as important during this process; 28 reactions were found to have a significant effect on the light curve, with $^{34}\mathrm{Ar}(\alpha,p)^{37}\mathrm{K}$ in that group, as seen in Fig. 3.2. Another 72 reactions were identified as significantly impacting the final abundances of the XRB. The $^{34}\mathrm{Ar}(\alpha,p)^{37}\mathrm{K}$ reaction had no noticeable impact on final abundances.

The second phase used a multi-zone model using KEPLER, with the network fully coupled to the stellar evolution. In multi-zone models, each zone has different, but coupled, values for the various measured quantities (mass, radius, thermodynamic variables, and abundance profile), with material and abundance mixing from one zone to another. In this model the choice of rate variation was slightly more involved. If uncertainty values or reasonable upper limits on these values were available, they were used, if not the same factor of 100 was applied. The rate of $^{34}\mathrm{Ar}(\alpha,p)^{37}\mathrm{K}$ was varied by a factor of 10 in the second phase, multi-zone model.

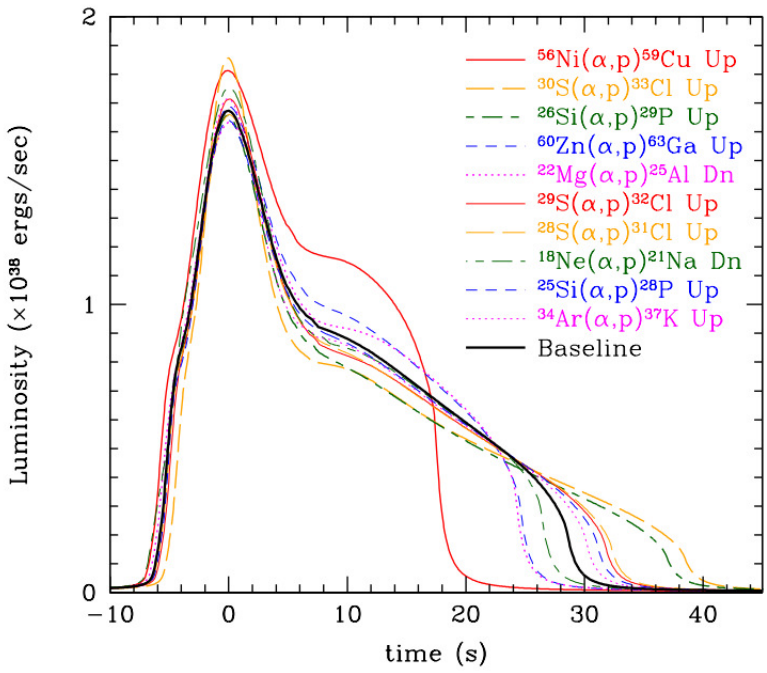

FIGURE 3.2. Computational predictions of the XRB light curves produced when the listed reaction rates are varied by a factor of 100 up or down [9].

In the single zone model, the reaction ^{34}Ar$(\alpha, p)^{37}$K was found to alter the luminosity by a sensitivity of .8, with sensitivity defined by the metric

$$M^i_{LC} = \int | < L_i(t) > - < L_0(t) > |dt, \tag{3.1}$$

or the luminosity difference over time integrated for the entire burst, where L_0 and L_i are the baseline and current model luminosities, respectively. The ^{34}Ar$(\alpha, p)^{37}$K reaction was 26 of the 28 reactions found to significantly affect the light curve. However, in the multi-zone model it was found to have no impact on the light curve, though it should be noted that the authors acknowledge a significantly different result if the rate had been varied by the same factor of 100 the multi-zone model as were some other rates. In that case, it would have reached their benchmark for significance. The ^{34}Ar$(\alpha, p)^{37}$K reaction rate was found to have no effect on final abundances in either phase of this study.

It should be noted that a sensitivity study without coprocessing should be regarded with caution as evidenced by the existence of the double-peaked burst. The post-processing method relies on the assumption that a small network, sometimes just a few species, is sufficient to calculate the energy generation. If the double-peaked behavior was found to be caused by the nucleosynthesis, that would not only be strong proof of the need for the feedback mechanism, but would also show that any model without the ability to display this behavior is incomplete. Since the light curve is known to be correlated with the thermodynamic profile, any reaction with the ability to affect the light curve strongly must also have a significant impact on the thermodynamic profile. This could also be said for any reaction thought to be inextricably linked to specific features of the burst that is not included in the standard truncated network used for pre-processing of the stellar evolution: ^{18}Ne$(\alpha, p)^{21}$Na and ^{15}O$(\alpha, \gamma)^{19}$Ne for example.

3.2 Existing Rate Information

When experimental information for a reaction is not available or is incomplete, we must rely on theoretical calculations to estimate its rate. T. Rauscher & K. T. Thielemann are responsible for many of the theoretical rates in the standard library, REACLIB, which is a database of measured and theoretical reaction rate values assembled by Cyburt *et al.*[23] representing the most up to date and accepted literature values, and version controlled by date for strict comparison. In a seminal work from 2000, Rauscher & Thielemann calculated reaction rates for (n, γ), (n, p), (n, α), (p, γ), (p, α), and (α, γ) reactions as well as their inverses [24]. The work was done using the Hauser-Feschbach (HF) code NON-SMOKER, to produce a comprehensive database of theoretical rates. The Hauser-Feschbach method uses estimates of the density of resonance levels and transmission coefficients of the entrance channels to the compound nucleus. Combined with the allowed exit channels, these form a complete set of all the possible contributions to the reaction rate. However, the HF approximation relies on an assumption of high level

density, that is, 5-10 non-overlapping narrow resonances per MeV [24] so that the total reaction rate can be estimated by a sum of the contributions for each level at a given temperature. The existing $^{34}\mathrm{Ar}(\alpha, p)^{37}\mathrm{K}$ reaction rate in the standard industry library "REACLIB" [23] is depicted in 3.3 and 3.4 [24], and is given by the the exponential approximation

$$e^{[a_0+a_1/T_9+a_2/T_9^{1/3}+a_3*T_9^{1/3}+a_4*T_9+a_5*T_9^{5/3}+a_6*log(T_9)]} \tag{3.2}$$

where

$a_0 = 53.8370$

$a_1 = 0$

$a_2 = -70.86$

$a_3 = .2630$

$a_4 = -8029$

$a_5 = .0550$

$a_6 = -.6666$

Other than this theoretical calculation, little information exists regarding the rate of the $^{34}\mathrm{Ar}(\alpha, p)^{37}\mathrm{K}$ reaction, which is thought to be important to XRB's as discussed in Ch. 2, hence the motivation to study it. Because of the difficult nature of studying radioactive species, as well as the difficulty measuring the small cross sections in the astrophysically significant energy range, there is no comprehensive rate for this reaction based on experiment. Previous experiments are limited and too recent to be included in the accepted rate. In fact, the REACLIB rate for this particular reaction is strictly theoretical, based exclusively on HF calculations by T. Rauscher as part of the REACLIB v1.0 release and updated in 2010 by Cyburt *et al.* [23].

We can speculate on the details of the compound nucleus, including the energy levels and spins, using the mirror nucleus $^{38}\mathrm{Ar}$. Since $^{38}\mathrm{Ar}$ is stable it has been studied more

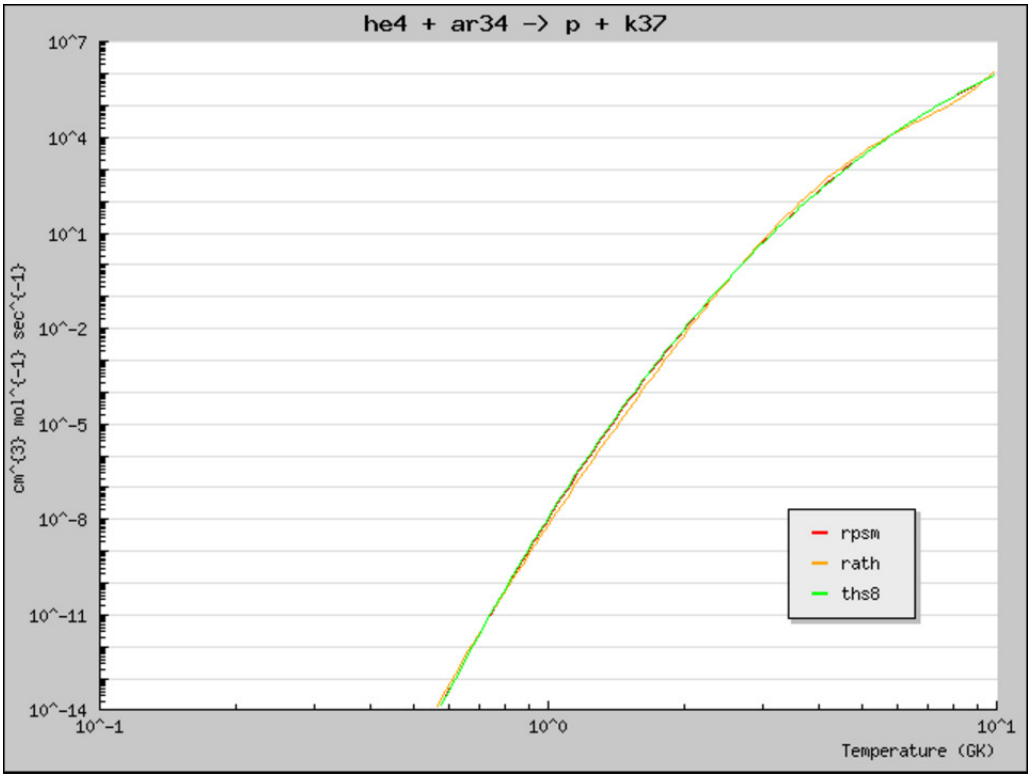

FIGURE 3.3. The current accepted value for the $^{34}\mathrm{Ar}(\alpha, p)^{37}\mathrm{K}$ reaction rate, taken from REACLIB [23] and produced by the theoretical work of Cyburt *et al.* [24], denoted in the figure as ths8, along with the rate from [25] denoted rpsm, and from [24], denoted rath.

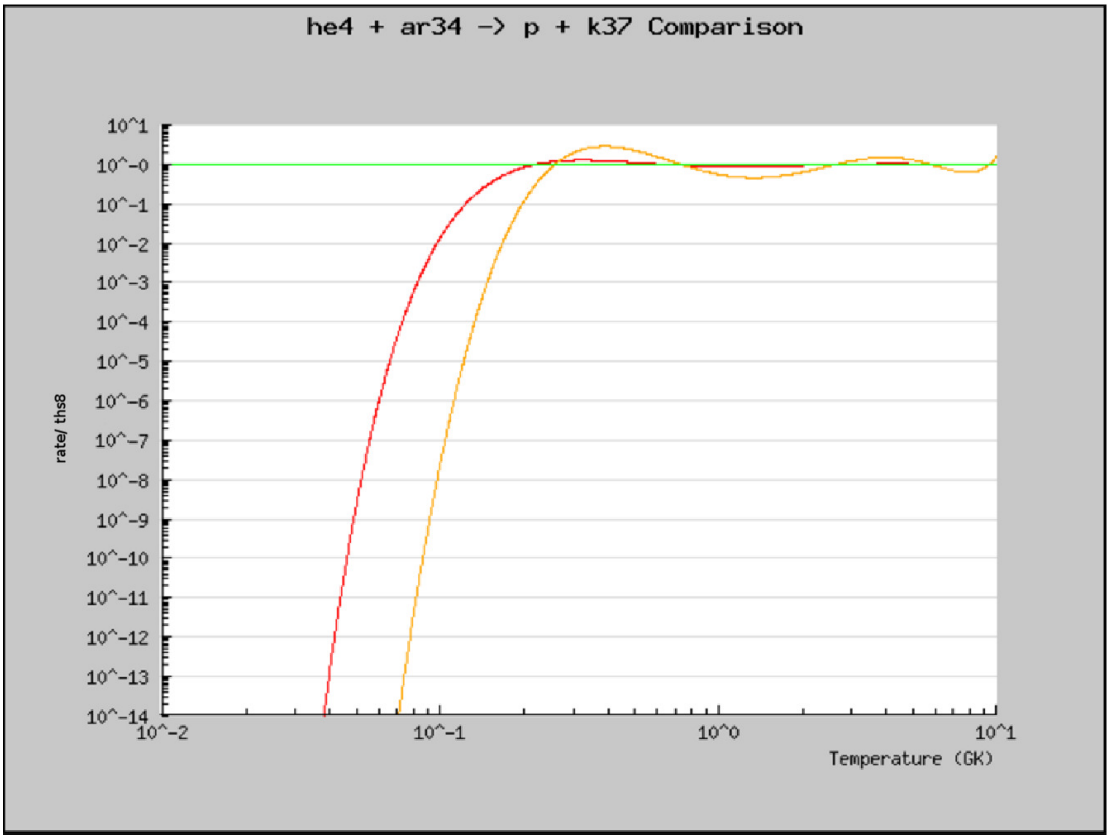

FIGURE 3.4. The ratios of rpsm (red) and rath (yellow) to current accepted value (green) for the ^{34}Ar(α, p)^{37}K reaction rate, taken from REACLIB [23].

extensively. When preparing for new experiments as well as analysis, the mirror nucleus is one of the starting points for predicting resonance energies. The levels in ^{38}Ca that correspond to the mirror should be s-wave resonances, which are probably the most influential on the reaction rate. In the mirror nucleus there are at least 10 known s-wave states that lie approximately within the energy regime of the experimental setup (E_r = 5157, 5552, 6249, 6852, 6947, 7181, 7236, 7370, 7702, and 7893 keV) [26]. An additional group of p-wave resonances should also exist in the same region, with approximately the same density.

3.3 Previous Experiments

In 2008, O'Brien *et al.*, at the Research Center for Nuclear Physics in Osaka, Japan used the fully dispersion matched WS beam line with the Grand Raiden spectrometer, to study the compound nucleus of four of the waiting point nuclei (^{22}Mg, ^{30}S, ^{34}Ar, ^{38}Ca) using (p,t) reactions. They utilized a 100-MeV proton beam directed to a target chamber which held 3.51-mg/cm^2-thick target of ^{40}Ca, to study the ^{40}Ca$(p,t)^{38}$Ca reaction. The reaction products were momentum analyzed using the K=600 spectrograph, while the tritons were detected by two Multi-Wire Drift Chambers, which measure position and angle information, and two plastic scintillators, which measure timing and are used for particle identification. This work extended the previous search for excited states in ^{38}Ca from 7-8 MeV up to 12 MeV. The published results from this experiment are limited to the image of the excitation function in Fig. 3.5 [27]. Though a detailed analysis has not been published, the levels within the observed energy range of this experiment appear consistent with those discussed below from Long *et al.*, with one possible exception in the region of 7.6 MeV which will be discussed in Ch. 6.

The 2017 work by Long *et al.* [28] also studied the compound nucleus ^{38}Ca through the ^{40}Ca$(p,t)^{38}$Ca reaction at the iThemba LABS facility Somerset West, South Africa. They utilized a 100-MeV proton beam produced by the K=200 Separated Sector Cy-

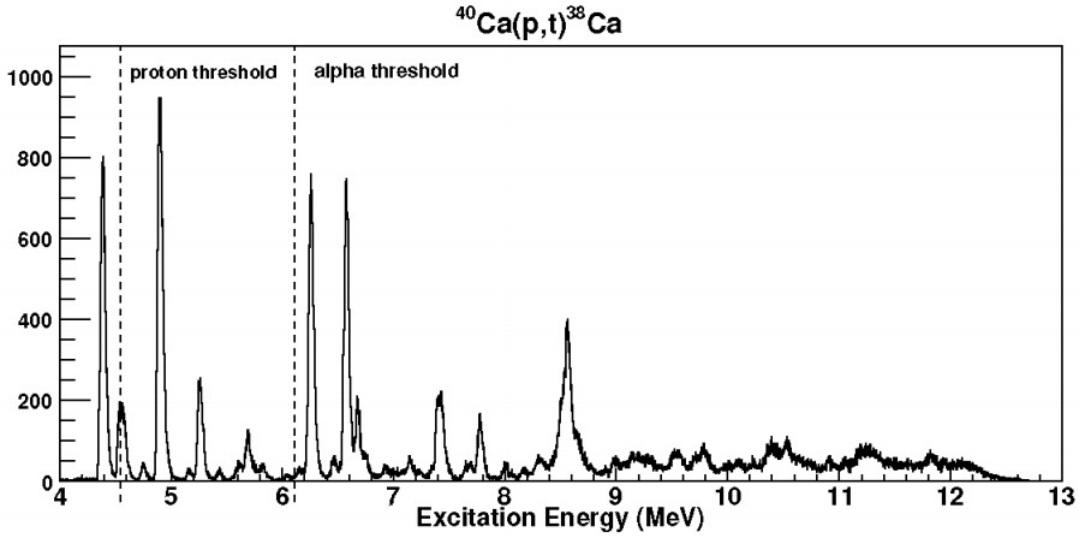

FIGURE 3.5. Excitation function from [27]. Numerical values for the resonance energies are not given directly and no further analysis of the data from this experiment has been published, but visual examination reveals that the results are similar to those given in [28], except for a small feature in the range 7.5-7.8 MeV that will be discussed in depth in Ch. 6.

clotron directed to a target chamber which held a 2.1-mg/cm^2 target of highly enriched ($\geq 99\%$) ^{40}Ca, to study the ^{40}Ca$(p,t)^{38}$Ca reaction. The light reaction products and beam were momentum analyzed in the K=600 spectrograph, and the tritons were then transported to the detector system remarked to be similar to that of O'Brien *et al.* [27], of wire drift chambers and plastic scintillating detectors. The resulting momentum, position, angle, ΔE, and time-of-flight information of the tritons was then used to reconstruct the reaction kinematics and excitation spectrum in Fig. 3.6, which revealed the new levels. The spectrograph was used at two different field strengths to target the full range of excitation energies from the ground state to 13 MeV, as well as two lab angles ($\theta_{lab} = -1.2°$ and 8°). The new levels are listed in Table 3.1. The levels identified by this study may not all contribute strongly to the ^{34}Ar$(\alpha, p)^{37}$K reaction rate, and this will be investigated in the subsequent analysis of this work.

Deibel *et al.* used the Argonne Tandem Linac Accelerator System (ATLAS) at Argonne National Laboratory (ANL) to study the time inverse reaction ^{1}H$(^{37}$K,$\alpha)^{34}$Ar us-

TABLE 3.1. Excitation energies (keV) of unbound states measured by Long *et al.* (left) and previously known (right), with asterisks referring to those only measured at 8° [28]. The α threshold for ^{38}Ca is 6105.12 keV. The sources for the previously measured levels are: A.[29], B.[30] and C.[31].

Long *et al* (keV)	Previous (keV)
6277(3)	6280(30)^A/6270(8)^B
6485(6)	
6601(3)	6598(7)^A/6600(30)^B
6704(3)	6702(10)^A/6760(50)^C
6772(13)	6801(12)^A
6950(5)	
7041(8)	
7176(8)	7200(50)^A
7370(5)	
7480(9)	7470(50)^C
7801(3)	7800(12)^A/7800(30)^B
8026(5)	
8189(6)	
8322(5)	
8507(9)	
8586(3)	8595(10)^A
8672(6)	
8717(8)*	
8924(9)*	
8994(9)*	
9073(9)	
9157(8)	
9230(9)*	
9296(8)*	
9735(8)	
9809(6)	
10104(9)	
10410(9)	
10557(8)	
10946(11)*	
11089(11)*	
11189(13)*	
11861(11)*	

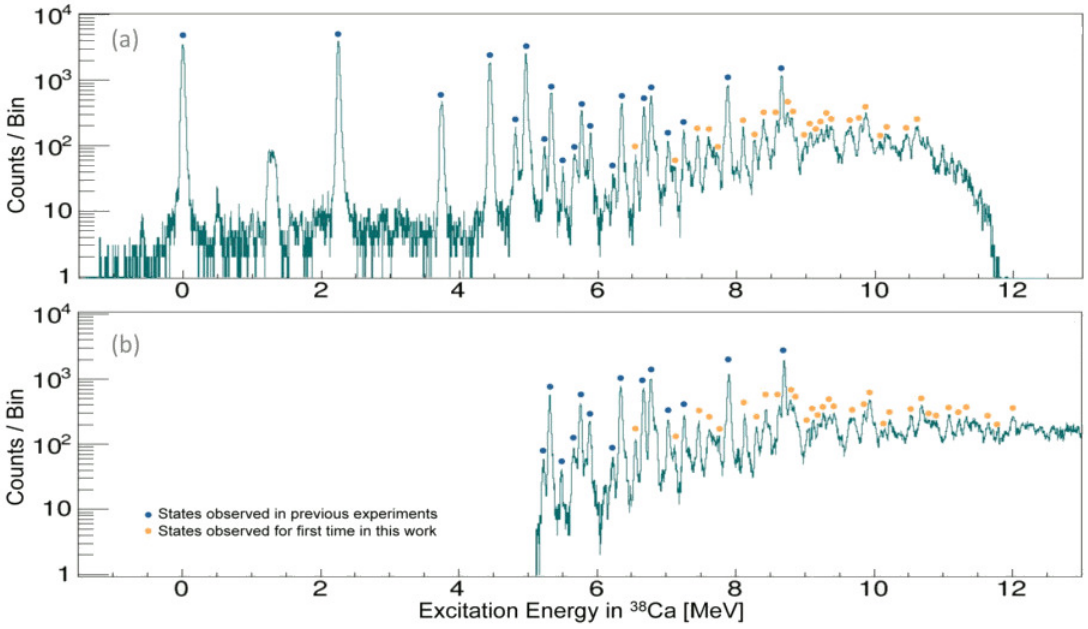

FIGURE 3.6. Newly discovered levels identified by Long *et al.* depicted along with the previously known levels [28]. The two figures represent different magnetic field strengths in the spectrometer to target different energy regimes.

ing a Si Strip detector and the Enge split-pole spectrograph [32]. The ATLAS accelerator was combined with the in-flight technique [33], in which a stable beam impinges on a very low Z target before the experimental area to create the radioactive beam. A 360-MeV ^{36}Ar primary beam impinged on a LN_2-cooled D_2 gas target at 1.4 atm to create a 275-MeV radioactive beam of ^{37}K with intensities on order of 10^4 pps, with a beam purity of around 50%. This heavy beam was then impinged on a 650-μg/cm^2 proton-rich CH_2 target in what is referred to as inverse kinematics (i.e. a heavy beam on a light target). Gold degrader foils of varying thickness were used to reduce the beam energy and thus target a range of energies with a single beam energy. The light α particles were detected in an annular Si detector designed to measure energy as well as angle relative to the beam axis, while the ^{34}Ar heavy recoils continued at shallow angles into the Enge magnetic spectrograph, which momentum analyzed them before they were detected in a parallel grid avalanche counter and ionization chamber (IC). Position and energy loss of the ^{34}Ar ions and α particles, time-of-flight, and coincidence detection were combined

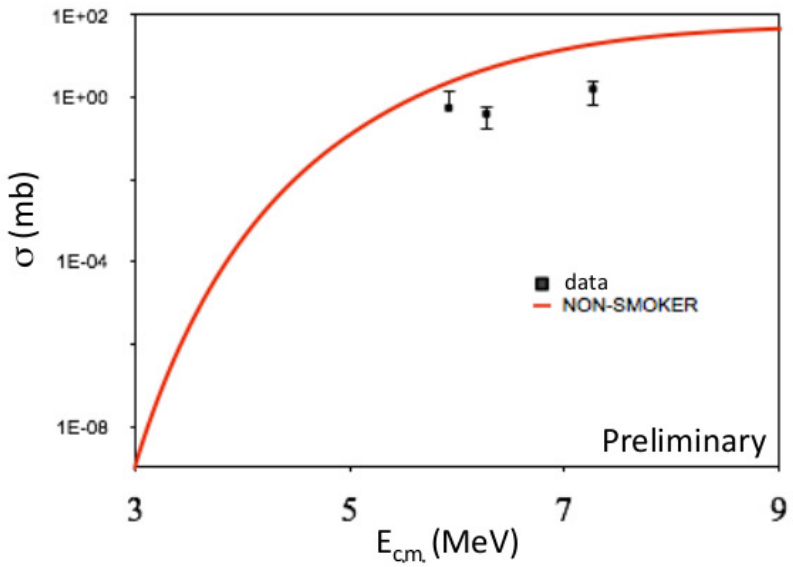

FIGURE 3.7. Preliminary data points from the time inverse reaction $^{37}K(p,\alpha_0)^{34}Ar$ performed at ANL [34].

to reconstruct the kinematics of the reaction, and the yield was used to determine the cross section of the time-inverse reaction. Due to the principle of detailed balance, the reverse ground-state to ground-state reaction rate (i.e. ^{34}Ar$(\alpha, p)^{37}$K) can be calculated to the same uncertainty. Because of beam contamination, the data was limited to the higher energy alpha branch. The cross section was measured at beam energies corresponding to a range of 6 MeV <$E_{c.m.}$ <7.6 MeV, which is outside the Gamow window for this reaction, described in the previous chapter. Preliminary analysis shows deviation from the accepted Hauser-Feschbach rate as seen in Fig. 3.7, and this is thought to be attributed to the previously discussed limitations with HF theory related to level density. Further analysis is in progress [32].

Most recently, members of a collaboration led by PI Kelly Chipps used the Jet Experiments in Nuclear Structure and Astrophysics (JENSA) gas jet target to study the ^{34}Ar$(\alpha, p)^{37}$K forward reaction. This experiment was conducted during the same experimental cycle as the proton elastic scattering discussed in this work, using some similar experimental equipment as this work which will be discussed in Ch. 4.

The $^{34}Ar^{15+}$ beam was provided at 1.625 and 1.710 MeV/u at average intensities of 1700 and 1000 pps, respectively. The JENSA target was designed as a solution to the general challenges of gas targets. In order to provide a ^{4}He target one must use the element in its gas state, since its liquefaction temperature is around 4K. This raises the difficult task of cooling and/or compressing the gas to achieve densities large enough to be useful in nuclear experiment. Several other solutions to this problem exist. For instance, the ATLAS experimental setup discussed earlier uses a chilled gas target contained in an aluminum cell with Havar windows. LN_2 is constantly circulated around the gas volume to chill it to temperatures of 90K, achieving a factor of 3 improvement in density over standard temperature and pressure conditions.

The JENSA gas jet target is a compressed jet open to the experimental environment, with a width of 4 mm at a density of 10^{19} atoms/cm^2. The detector system consisted of Si detectors arranged on the inner surface of the cylindrical experimental chamber, with an annular end-cap. This barrel configuration measures the lighter α particles and protons at their higher emission angles, while on the beam axis at the shallowest angles, a gas filled ionization chamber, provided by LSU and discussed in Ch. 4, collected the heavy ^{37}K recoils. However, due to the low radioactive beam intensities and low cross sections in the astrophysically relevant regime, the range of energies studied 5.75 MeV $<E_{c.m.}<$6.25 MeV, was above the Gamow window, so future work remains. This experiment remains under analysis [35].

Chapter 4
Experimental Design

4.1 Indirect Experiments

The reaction of interest, ^{34}Ar(α, p)^{37}K, involves radioactive species on both ends; the ^{34}Ar reactant as well as the residual nucleus ^{37}K. Ion beams of radioactive species, especially those that are short lived, can be difficult or even impossible to produce depending on stability. Those beams that can be produced are often low in intensity compared to stable beams by orders of magnitude. These low beam intensities combined with the low cross sections of charged particle reactions at astrophysically relevant energy regimes often make the direct reaction measurements impractical or impossible. In the ^{34}Ar(α, p)^{37}K reaction both the heavy projectile and light target are difficult to use in experiments. ^{34}Ar has half life of $T_{1/2}$=844.5 ms, and therefore cannot be used to create a target. The only alternative is to use it as a projectile, and then it is necessary to create, isolate, and accelerate this short lived-unstable species. The target reactant is an α particle, which is the ^{4}He nucleus. The difficulty with using this as a target, discussed in the previous chapter, is seen in the uncommon phase diagram of ^{4}He which is a gas down to temperatures of 4K and has no true solid-liquid-gas triple point. Therefore we are not able to rely on predictable phase changes to manipulate the gas more easily. This poses difficulties in target handling as well as target density. As seen in Section 2.5, the relative values of density and area of the projectile and target figure heavily into the reaction rate. Gas targets, then, are not ideal, so various methods have been developed to improve the particle densities, such as chilling and compressing. These methods still present difficulties, though, and so it is advantageous to consider other avenues. Studying the reaction of interest directly is always the ideal, but when this is not possible

other reactions can reveal partial information that allows us to calculate or estimate to the quantities important in the reaction rate equation rate discussed in Ch. 2.

Time-inverse reactions like that in this work are useful to study, however, we are only able to study ground state to ground state transitions, while we know that excited states in the daughter nucleus may also be significantly populated. Like the heavy reactant in the forward reaction, ^{34}Ar, the heavy reactant in the time-inverse reaction, ^{37}K is radioactive, so it too cannot be used as a target, and therefore must be the beam projectile. Fortunately, ^{37}K is closer to stability than ^{34}Ar, with a half life of $T_{1/2}$=1.227 s. The necessary proton target can be achieved using one of many proton-rich polymers, in this case polypropylene, or C_3H_6. Due to the very low cross section of the full, ^{37}K+p, fusion channel, the current experimental setup would likely count just a few events ovesr the extent of the experiment. An alternative method is to study properties of the compound nucleus via other interactions, such as that in this work. While scattering does not reproduce the full fusion reaction, the behavior still allows us to draw conclusions about the excited states of ^{38}Ca that may be populated by the ^{34}Ar$(\alpha, p)^{37}$K reaction. Thus we studied proton scattering to examine excited states in the compound nucleus ^{38}Ca to study the important components of the reaction rate, such as the resonance energies of ^{38}Ca, and their partial widths, and spin (J^{π}) states, this indirect study allow us to help constrain the reaction rate, following a method similar to Ruiz *et al.*[36].

4.2 Experimental Setup

There are three main components to this experimental setup: the beam line, target, and detectors. The ^{37}K beam was provided by the NSCL starting with a Electron Cyclotron Resonance ion source injecting ^{40}Ca into the K500 & K1200 coupled cyclotrons, which are the primary accelerators depicted in Fig. 4.1. Projectiles can be accelerated as high as .5c. The ^{40}Ca primary beam impinges on a ^{9}Be production target that creates multiple isotopes, and the A1900 fragment separator uses various magnetic fields to select the

desired ^{37}K isotope based on magnetic rigidity, which is related to charge, mass, and energy. A gas catcher then extracts the ions and slows them to be used down the beam line. The final projectile species is then fed into the Electron Beam Ion Trap charge breeder to strip electrons and produce a highly charged ^{37}K beam that can then be accelerated more efficiently. The ReA3 linear accelerator then re-accelerates it for use in the experimental area. This resulted in a 4.448 MeV/u ^{37}K beam with 85% purity and an intensity of 10^4 pps. Finally the prepared beam enters the experimental area, where the experiment-specific target as well as the detector equipment are located. A multi-target wheel with apertures centered on the beam line, holding a 30-μm prepared target of C_3H_6 is the final destination of the beam before it enters the detector equipment. An additional target of 3.2-mg/cm^2 ^{12}C was included to measure background from the ^{37}K+^{12}C fusion evaporation reaction which can also occur on the polypropylene target. The experiment was run in March 2016, with 13 days of the primary beam and 1.5 days of runs using beams ^{40}Ar, ^{37}Cl, and ^{37}Ar to test background, beam contamination, and fusion evaporation products.

After the beam impinges on the target the reaction products behave in a predictable way according to the kinematics of the reaction, and depending on their relative masses. The light protons are ejected from the target at angles from 0-90° and are detected by an array of 4 layered telescopes of double-sided silicon-strip detectors. This array is shown in Fig. 4.2. In the silicon detectors, the particles create electron-hole pairs, and a bias voltage is applied to the back layer of Si to force the charge to be collected before the pair recombines. The telescopes occupy 4 quadrants, paired diagonally, with either 2 layers of model QQQ3 or 3 layers of model QQQ5 Si detectors, supplied by Micron Semiconductor LTD. Both designs span an angular range in ϕ of roughly 45 degrees, giving near complete coverage in ϕ around the beam which defines the z-axis. The array is positioned at 23.14 cm as measured from the target along the beam line to the plane

c 

FIGURE 4.1. Internal view of an NSCL cyclotron. Usually the equipment is under high vacuum, and must be temporarily taken off line to view its internal structure [37].

of the active area of the first upstream detector in the QQQ3 telescopes, and the plane of the active area of the second detector is located .645 cm behind the first. The QQQ5 telescopes are located at 23.485 cm as measured from the target along the beamline to the plane of the active area of the first upstream detector, with the next layer active area plane .645 cm behind and the third .74 cm farther. The front area of the QQQ3 detector is divided into 16 successive anular strips in θ, with equal pitch, while the back side is divided into 16 strips segmented in ϕ. The front area of the QQQ5 detector is divided into 32 strips in θ, which were designed with variable pitch specifically to minimize the difference in surface area with increasing θ. The back is divided into 4 segments in ϕ. This corresponds to angular coverage, projected from the target, for the QQQ3 and QQQ5 telescopes, of θ_{lab}=12.55-22.84° and 6.4-19.17°, respectively. The first layer of the QQQ5 telescope had active detector thickness of 100 μm, while layers 2 and 3 as well as both layers of the QQQ3 telescopes had active detector thickness of 1 mm. Assuming a particle loses all its energy in the detectors, successive layers give individual energy loss and can be summed to give total energy, which, when compared assist with particle ID. The angular information, when combined with the energy information provides the details to reconstruct the kinematics of the scattering in the center of mass (c.m.) frame, in which the energy of the system has no dependence on the velocities of the two particles, but is instead only related to the structure information of the compound nucleus. Thus the raw energy measured in the detectors as well as the angular information implicit in the strip identification provide the quantities necessary to calculate energy in the lab and center-of-mass frames.

The forward focused heavy projectile, as well as the unreacted beam continue to travel at shallower angles ($< 2°$) compared to the protons and enter a Kapton window into a gas-filled Ionization Chamber (IC). This detector is based on a proven design [38] [39] adapted and built at LSU [40]. This cylindrical chamber was filled with inert CF_4 (carbon

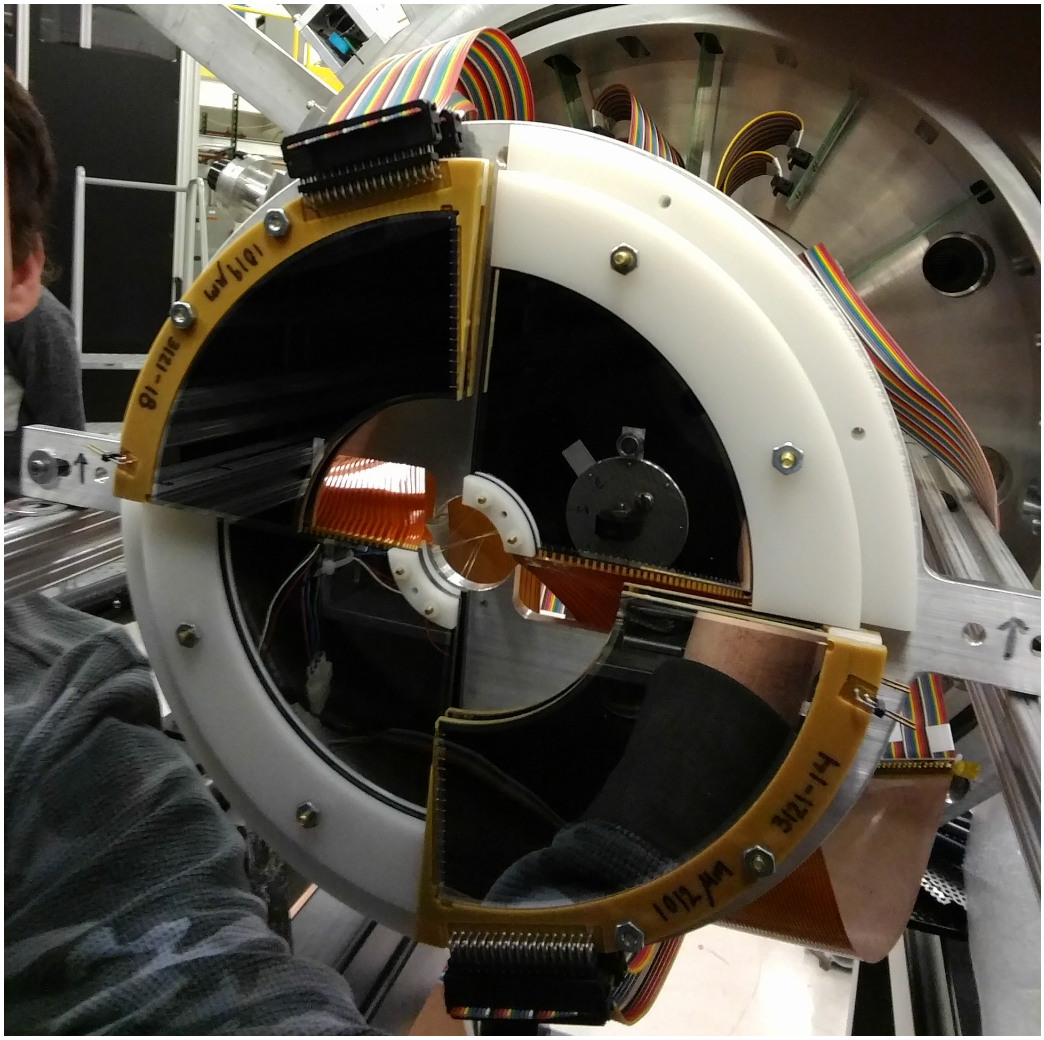

FIGURE 4.2. A photograph of the installed Si array in the experimental setup at NSCL, MSU.

tetrafluoride) gas held at a constant pressure of 40 Torr. The chamber houses a series of 20 grids of 2 cm spacing, positioned normal to the beam line and centered on the axis. Eighteen of these grids are 21.6 cm diameter aluminum rings with an inner diameter of 17.8 cm., wired with gold plated tungsten wires spaced 2 mm apart, as seen in Fig. 4.4. These grids are alternately held at a positive bias voltage and ground, to create a field which preferentially directs ionized electrons towards the biased grids. These biased grids are wired in common with others in a group, and there are two groups to detect successive energy loss measurements, denoted as ΔE, and seen in Fig. 4.3.

A recent update to this design is the addition of Printed Circuit Board (PCB) grids in the anode position in the first two sections. These 21.9-cm diameter grids have a square hollow inner area with side length 10.0 cm, with 3-mm wire spacing. These PCB grids have resolution down to a single wire (as opposed to the entire grid), and thus any signal allows for position information perpendicular to the wires. The two grids themselves are placed perpendicular to one another, so the x and y position information is combined to give a location within the chamber volume. Thus there are four sections in the ionization chamber: the first two individual PCB (x,y) sections, and the third and fourth energy loss sections discussed above, with 2 and 5 biased grids wired in common, respectively. Both the position-sensitive and common wired grids are shown in Fig. 4.4. The assembled grid array is shown in Fig. 4.3.

The heavy particles enter the chamber and collide with the gas molecules, ionizing the outer shell electrons. These electrons are collected by the grid, and the total current value is proportional to the energy loss of the heavy particle. Assuming several sections of grids and a long enough volume in the chamber, the particle will lose all its kinetic energy ionizing the gas. The successive energy loss values in individual sections again provide total energy loss, as well as ΔE. This can be used to identify particles and reconstruct the reaction kinematics. A schematic of the entire detector array is depicted in

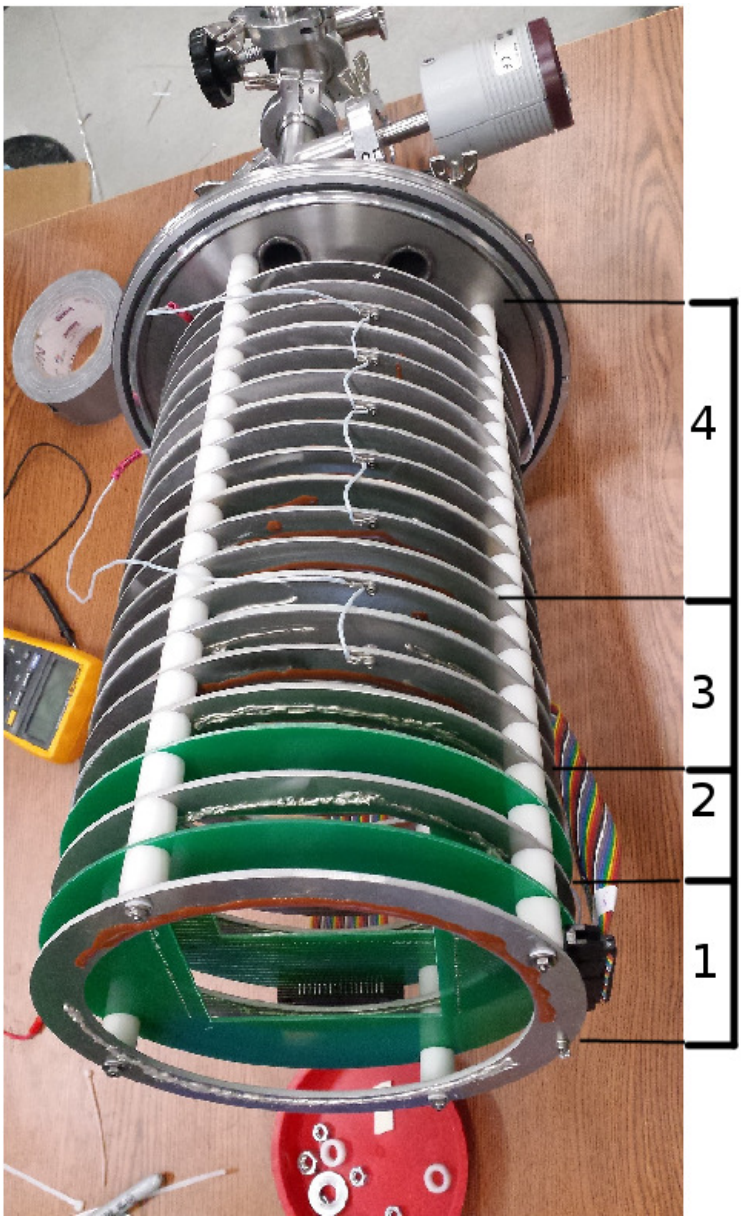

FIGURE 4.3. The assembled array of grids from the ionization chamber. Sections 1 and 2 are the green position sensitive PCB's, while 3 and 4 are sections measuring ΔE, and E residual, respectively.

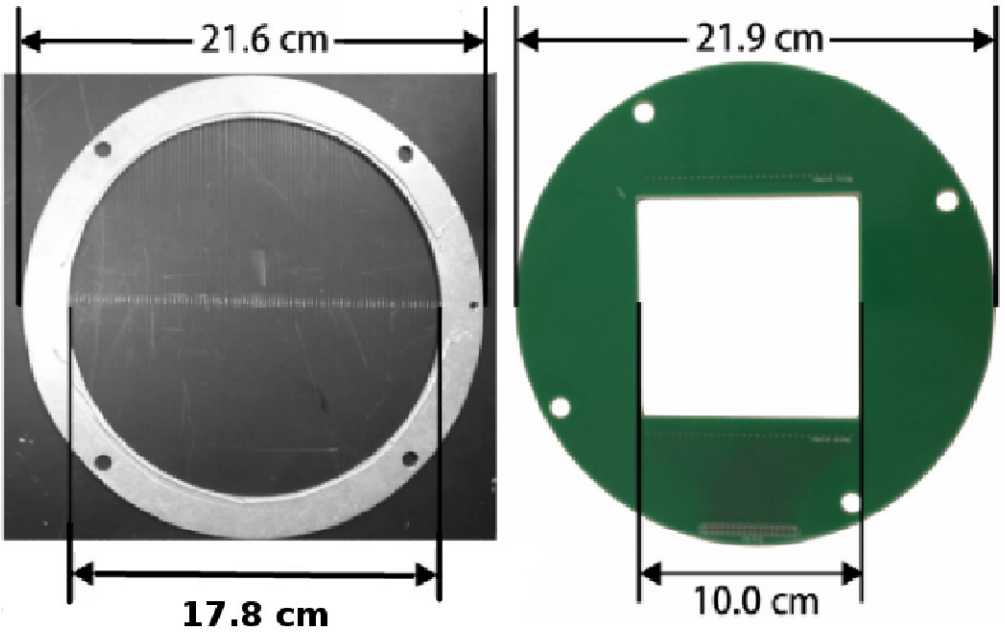

FIGURE 4.4. The left image shows the aluminum common wired grids, while the right shows the PCB grids, both from the LSU ionization chamber, taken from [40].

Fig. 4.5. Appendix B contains schematics for all the detector components including the Si array and IC.

4.3 Detector Electronics

The silicon detectors have 36 and 32 output signals for the QQQ5 and QQQ3 models, respectively, corresponding to each front and back channel, along with connections for ground, bias, and the guard ring. The detector output signals are connected via ribbon cable and vacuum feedthroughs to preamplifier motherboards designed and built at LSU to reorder the signals by channel in a more convenient layout and amplify the signal by 30 mV/MeV [41]. This design is based on the LASSA chip from Indiana University by

.

From there, the sorted and amplified signals enter the Application Specific Integrated Circuit (ASICs) Data Acquisition System (DAQ), which is an ideal system for experiments such as this with hundreds of channels, which might ordinarily require large

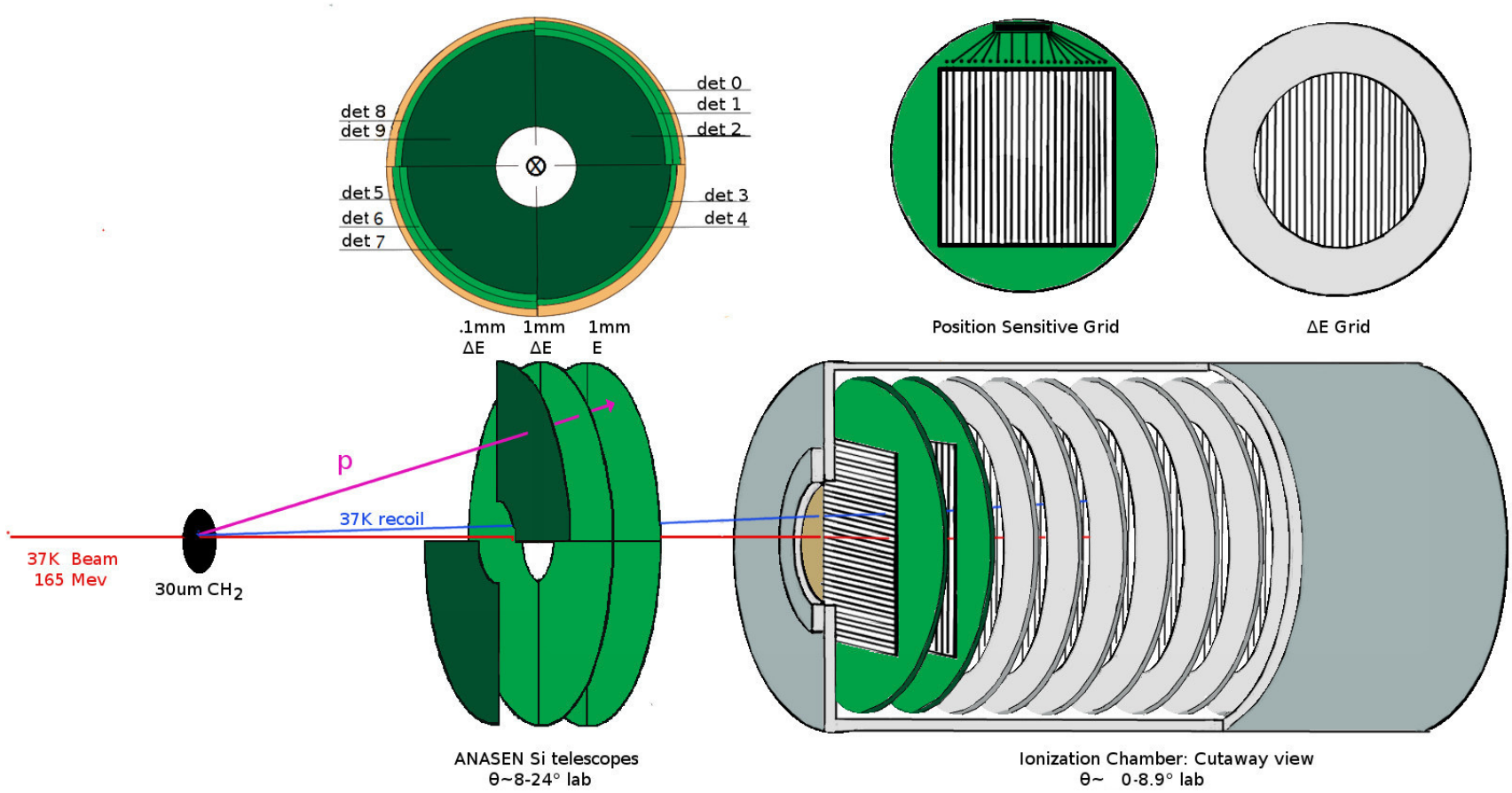

FIGURE 4.5. The experimental detector setup with details of position and angle.

numbers of analog components. This circuit design by [42] provides pulse shaping, additional amplification, and analog-to-digital conversion for solid-state detectors. The data is then digitized using XLM VME-based flash digitizers. The system utilizes a specialized computer system designed for experimental and commercial settings. This design transfers power management and data transfer needs to a large "dumb" standardized crate, while slots hold various component cards that perform signal processing tasks. A dedicated slot holds the crate resident single board computer, which is somewhat similar to the familiar motherboard-processor combination of personal computers, to make the data collection front end. The data is transfered over USB to a workstation running the MSU NSCL Data Acquisition System (NSCLDAQ), that organizes data into ringbuffer format and writes to storage in the NSCLDAQ .evt file format.

Similar front-end amplification is applied to signals from the IC using preamplifier boxes, which order and amplify the 32 signals from each of the two position sensitive PCB grids, as well as one signal each from the commonly-wired ΔE vs E sections, labeled 3 and 4 in Fig. 4.3. These preamplified signals are then digitized directly by an NSCL Digital Data Acquisition System (DDAS), which uses a PXI standard system to digitize the data using 100 Mhz digitization, and organize the data, creating an independent ring buffer of raw data that is read by the National Superconducting Cyclotron Laboratory Data Acquisition System (NSCLDAQ). In addition the DDAS system provides an internal 50 Mhz clock that is fed into a SIS3820 deep-scaler module included in the VME data stream to provide a synchronized time stamp between the DDAS and VME data streams. The two data streams (DDAS and VME) were merged using the event building feature of the NSCLDAQ system based on this synchronized clock, which is the last step of data acquisition before moving on to analysis using the ROOT package.

Additionally, the Si detector array trigger from the ASICs is sent to a analog Time-Amplitude-Conversion (TAC) module to start a relative time measurement with the ΔE

signal from the IC that is processed by a Constant-Fraction Discriminator that forms a stop to the time measurement. This measured value is converted to a voltage with amplitude relative to the duration, which is digitized using a channel of the DDAS system, to provide an independent analog-based time correlation between the data streams.

Chapter 5
Analysis

5.1 Calibration

The first step in analyzing the data provided by the experiment is converting it to the format required by the C++-based, statistical analysis package ROOT which was designed by the European Center for Nuclear Research (CERN) to handle the unique requirements and large data sets used in nuclear and particle physics experiment [43]. The NSCL standard nuclear experiment file format, the .evt file, contains the uncalibrated values from each channel of the DAQ. A C++ program written expressly for conversion to ROOT format takes the .evt file and organizes it in the ROOT file format structured around data units known as trees, branches, and events. An event contains signals from one or more channels corresponding to an event measured during the experiment, such as proton measurements in the Si, heavy ^{37}K recoils in the IC, unreacted beam in the IC, and a TAC signal for coincidence between the Si and IC. Within an event the raw signal value is recorded along with the corresponding channel numbers. ROOT then provides the framework to sort, filter, and calibrate events based on desired features such as minimum energy values or detector and channel information.

Within the Si telescopes, each detector and strip are generally set manually with a gain and offset within the electronics to match each other and to encompass the full range of needed values. The raw values correspond to a range of 32768 ASICs channels, however, the channel value has no meaning in real energy units, therefore, it is necessary to convert this information to meaningful energy values in keV.

Signals with known energy values are needed to provide this conversion. The detector response is approximately linear in energy, so it is necessary to know the channel of zero voltage and the slope of real energy values relative to the raw detector channel.

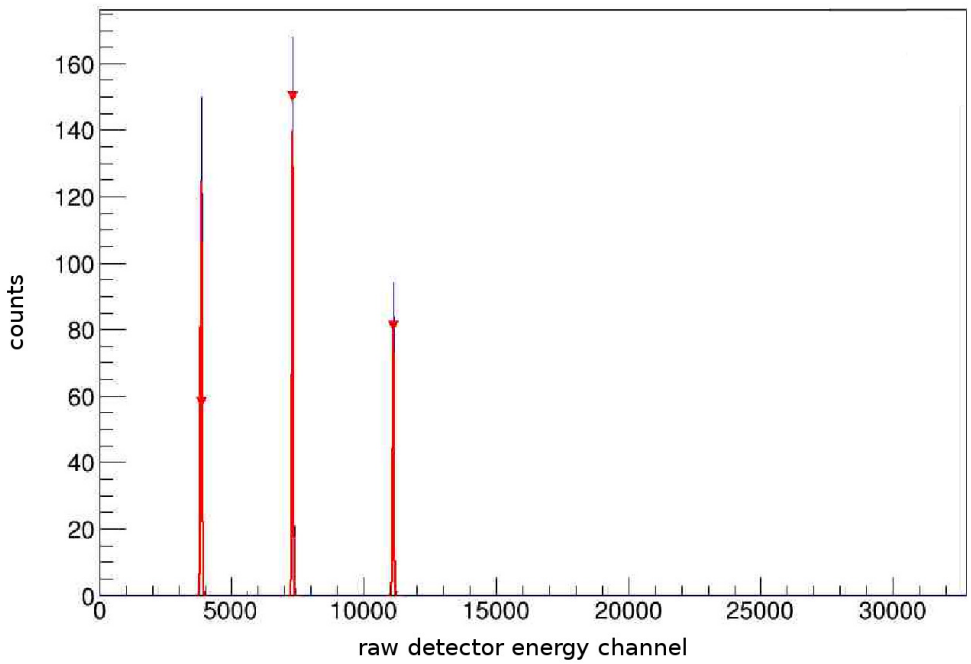

FIGURE 5.1. A ROOT analysis of the 300, 600, and 900 mV pulser spectrum of a single channel from a silicon detector. The results of the ROOT peak fitting are depicted in red.

An electronic pulser was connected to the input electronics for the detectors, and events of three known voltage values of 300, 600, and 900 mV were recorded by the DAQ . These spectra are analyzed individually within ROOT using fitting routines designed to detect the centroid of any Gaussian peak or other local maximum. Figure 5.1 shows a single channel spectrum of these pulser values, with the peak fitting estimate shown in red. From the centroid value of the three pulser peaks we extrapolate a line to find the channel of zero voltage, which corresponds to the channel of zero energy.

To determine the slope of the calibration a known energy value is provided by a radioactive isotope with a known emission spectrum. In this case, a source of ^{241}Am was placed in the experimental chamber. With its known α spectrum the raw channel can be adjusted by a factor corresponding to the primary decay energy divided by the raw channel peak centroid minus the zero energy channel. ^{241}Am decays 85% of the time by α particle emission with an energy of 5.486 MeV. Figure 5.2 shows the uncalibrated

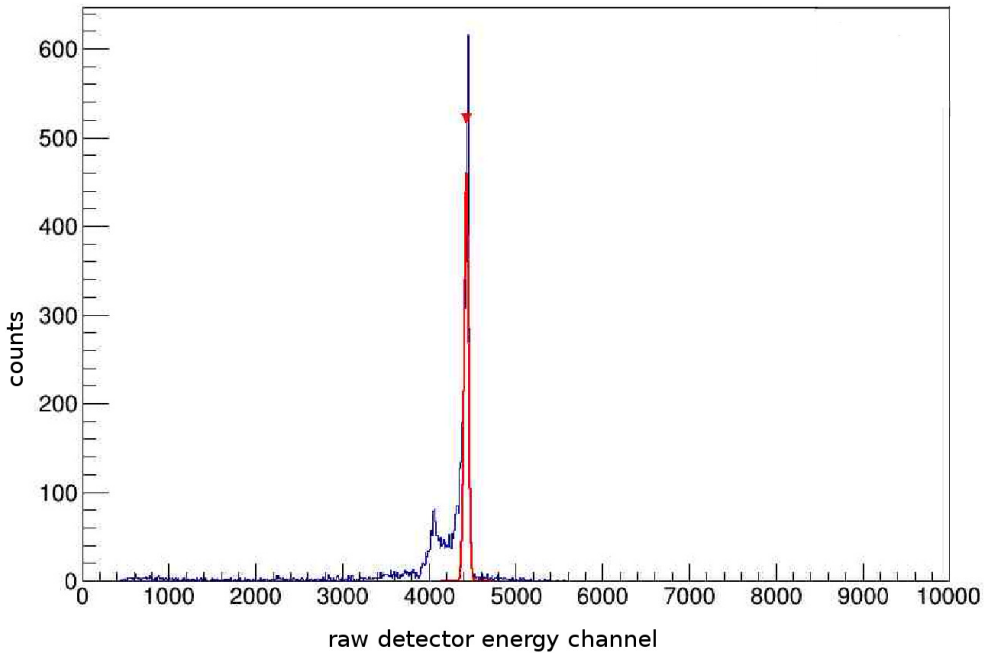

FIGURE 5.2. A ROOT analysis of the α peak spectrum of ^{241}Am in a single channel from the silicon detector. The results of the ROOT peak fitting are depicted in red.

^{241}Am α spectrum of a single channel in the silicon detector system. The broader asymmetric peak is due to an unresolvable triplet which includes the 13% 5.443 MeV and 2% 5.338 MeV decay branches. Fig. 5.3 depicts a color intensity plot of 32 channels for a single QQQ5 detector before calibration, with the channel number in the x axis and energy of counted events, in keV, in the y axis. Compare this to Fig. 5.4 which reflects the calibrated spectrum. The highest intensity regions in yellow correspond to the peak of the α energy which are all clearly aligned to within the energy resolution after calibration.

Ideally, a calibration spectrum is taken both before and after the experiment, to measure drift in raw channel values during the experiment. However, in both cases there was missing calibration information in some specific detectors, so the overall calibration reflects values taken from spectra recorded both before and after the experiment. In those detectors in which calibration spectra were available both before and after the experi-

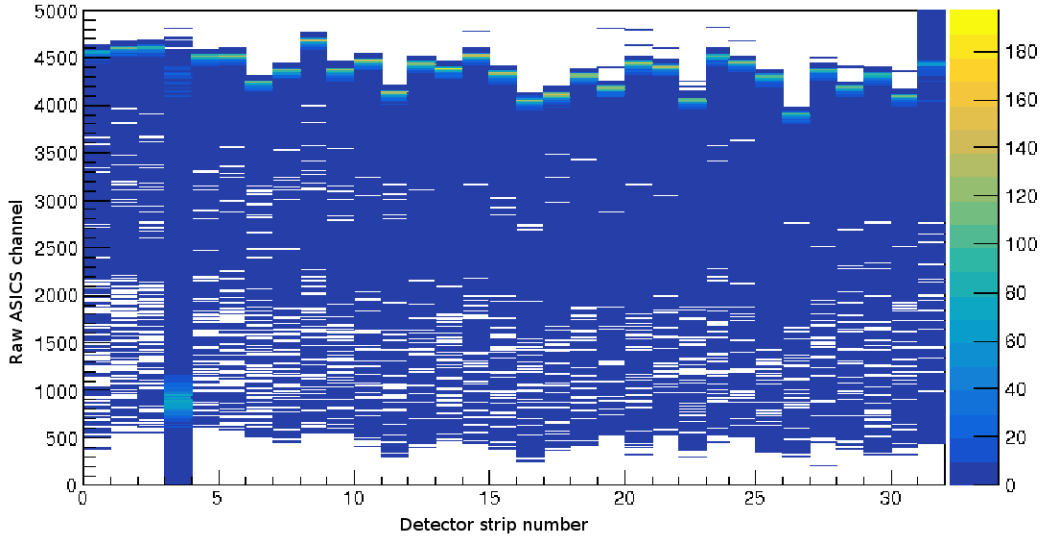

FIGURE 5.3. The uncalibrated ^{241}Am spectrum in a single QQQ5 detector. The highest intensity region in yellow corresponds to the peak of the alpha spectrum as depicted in Fig. 5.2, and in this spectrum corresponds to a raw energy value.

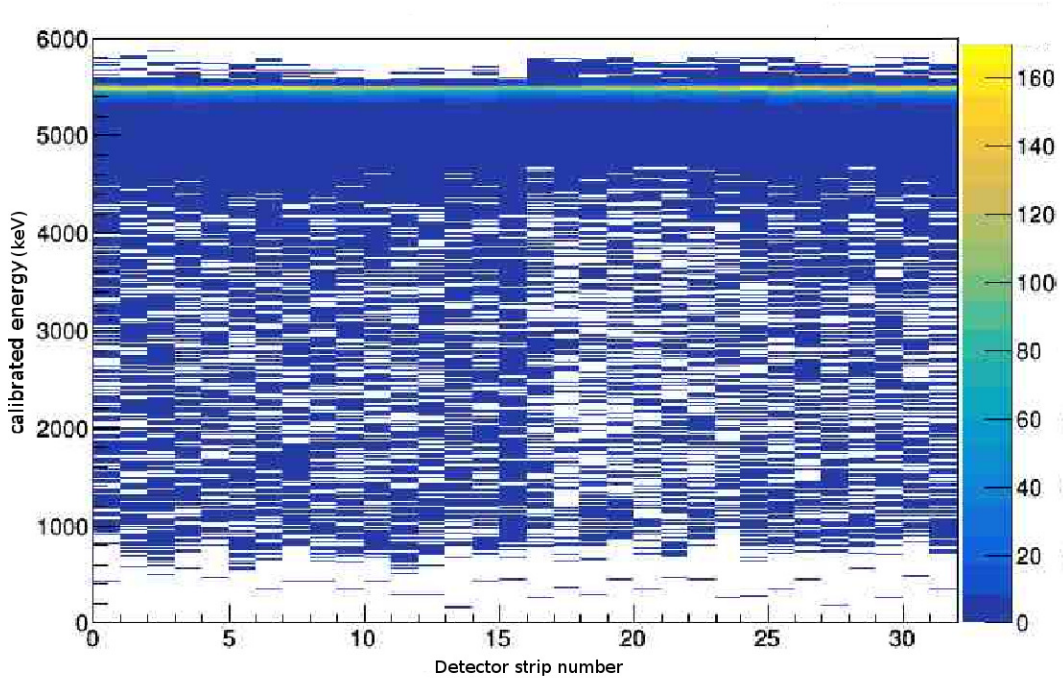

FIGURE 5.4. The calibrated ^{241}Am spectrum in a single QQQ5 detector. The highest intensity region in yellow corresponds to the peak of the alpha spectrum in each strip as depicted in Fig. 5.2, and should line up at a single energy value for every channel within the energy resolution.

ment the drift was minimal and less than the energy resolution of the detectors, and the resulting calibration is based on the assumption this is true for all detectors. In one of the three-layer QQQ5 telescopes, the backside of the third layer was missing calibration information entirely. In this case all energy values were taken from the front.

Another phenomenon common to segmented detectors is caused by the region between strips. When a particle is incident on this region it is common for its energy to be either split between neighboring channels with some loss, or duplicated in both channels, which makes the energy value for these events unreliable. To supply the missing energy information, the energy was taken from the backside channels, which are segmented in ϕ rather than θ. They are also subject to the same phenomena, however, because the region between strips is small, the conditional probability that events would be split in both front and back sides is low, and these events were $\sim$1% of total. In this way, errors due to this phenomenon were minimized.

A similar procedure can theoretically be performed on the ionization chamber with known signals, however, in this experiment the entire kinematic reconstruction was performed using the proton signals. The IC was put to two uses; to monitor the beam and to give time coincidence with events in the Si telescope. To accomplish the latter it was used as an input for the TAC module, which records the time elapsed between a detection in the Si array and the IC. This information is used for event identification, which will be discussed in the next section.

5.2 Event Identification

In this experiment, there are several nuclear interactions that can occur, and we use the coincidence timing from the TAC module to sort the events. The two most likely processes are the desired proton scattering, and the fusion evaporation from ^{37}K+^{12}C. Though the primary light products of ^{37}K+^{12}C are also protons, the most common heavy recoils, as calculated by LISE++'s, PACE calculator [44], should have a higher A and Z

than the heavy recoil from the ^{37}K+p proton scattering. The primary interaction between the heavy recoil and the gas in the IC is Coulomb scattering, and range goes as M/Z^2, therefore we expect the ^{37}K to travel much further in the IC than the fusion evaporation products. The heavy fusion evaporation products will not usually travel far enough into the IC to produce a signal and thus will not result in a TAC output. The scattering event signals from the protons detected in the Si and the ^{37}K recoils detected in the ionization chamber, will have a preferred range of TAC values. The fusion evaporation products should have a random time correlation to the unrelated heavy recoils in the IC. The TAC signal is recorded for every coincident event, and indeed forms a statistically significant peak. The uncalibrated TAC spectrum is shown in Fig. 5.5. Figure 5.6 analyzes the number of events added to the TAC spectrum for a given gate around the peak from Fig. 5.5. Within a gate of around ±2000 channels the number of events added is highly nonlinear, which indicate they are non-random or constant, and must correspond to events of interest. Outside of this range new events are added at a roughly constant rate over the remaining range of TAC values indicating random, uncorrelated events. The TAC background, shown in the Fig. 5.6 as the yellow line, was found by fitting the curve to all data in the TAC spectrum except the peak corresponding to the region of interest as in Fig. 5.7. By selecting a range of time values recorded by the TAC centered strategically around this peak, it is possible to preferentially select a majority of events of interest. After final analysis, a raw TAC gate from channels 12700-13600 was chosen to maximize good events and eliminate background. The final TAC range is bound by the green bars in Fig. 5.5.

To confirm we have made the correct choice for the TAC gate we can also look to the proton energy spectra. When comparing the calibrated energy losses in the first and second layers of a QQQ3 telescope, a pattern emerges. The protons detected form a grouping with a clear curve in the spectrum in Fig. 5.8. A second spectrum in Fig.

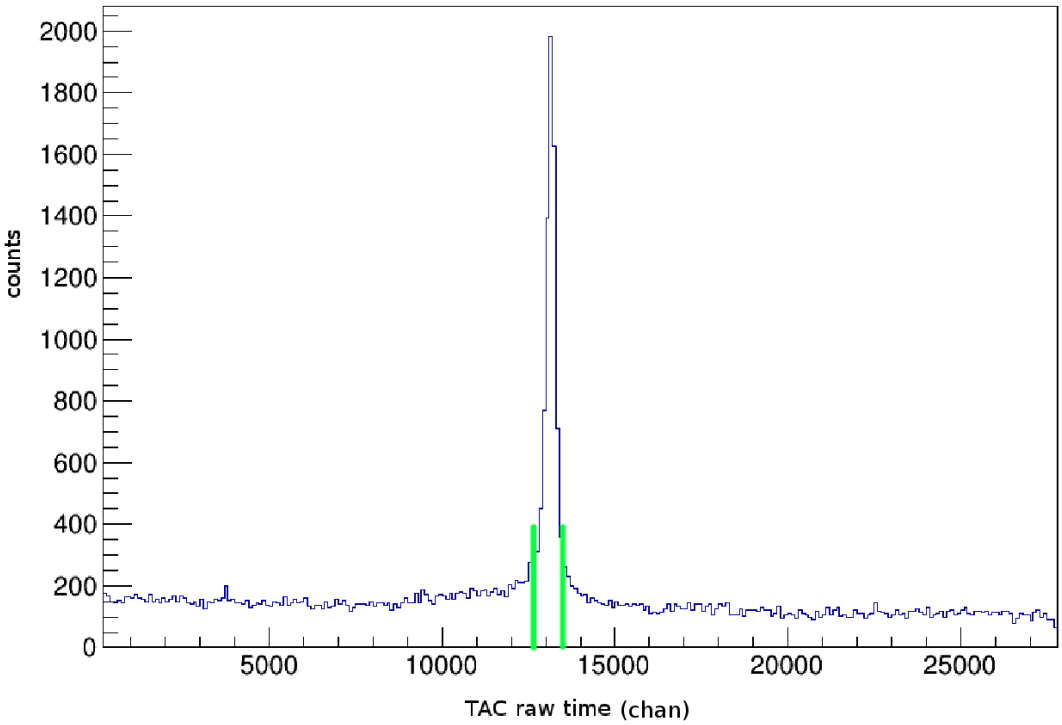

FIGURE 5.5. A raw (uncalibrated) spectrum of TAC values for the detected events in the experiment. These correspond to all the possible events. Since the heavy recoils from the fusion evaporation are not detected in the IC and thus do not generate a TAC signal, the peak must generally correspond to the events of interest, that of ^{37}K+p. The bars in green show the region ultimately selected as the TAC gating value discussed in the text.

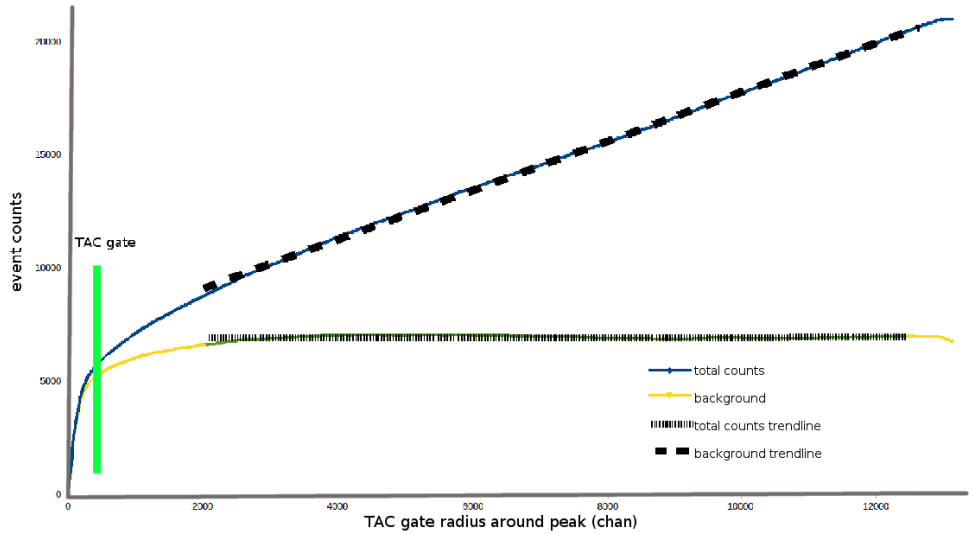

FIGURE 5.6. TAC range analysis which shows the addition of events with time width. Within a range of ±2000 channels around the peak in Fig. 5.5, the curve is non-linear, corresponding to the events of interest. The events added outside the peak are very nearly linear with time and must be random, and therefore correspond to fusion evaporation and other background. The data points are shown with a trend line approximation. The green vertical line reflects the TAC gate chosen.

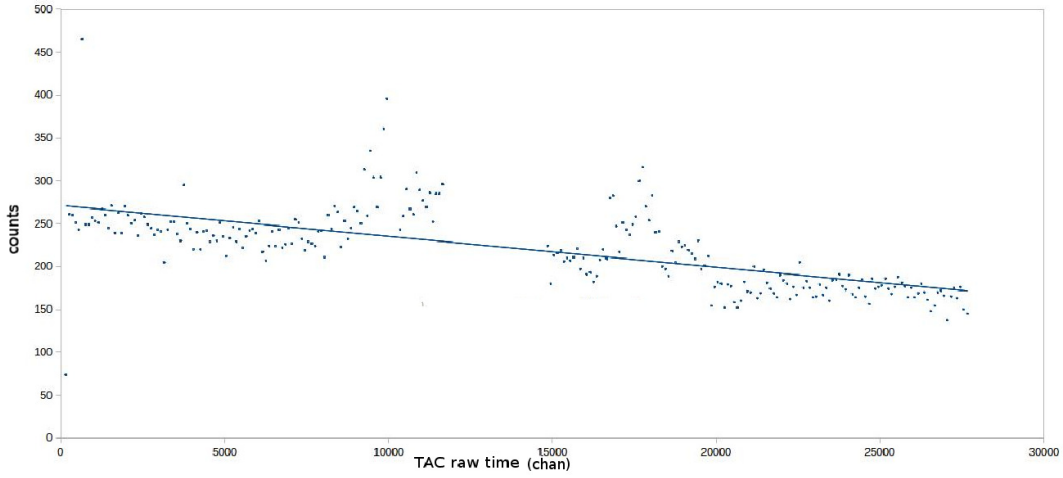

FIGURE 5.7. A raw (uncalibrated) spectrum of TAC values for the detected events in the experiment with the ^{37}K+p coincidence peak removed inside the gate. The remaining values can be well modeled with a line. The slope of this line is small, and this demonstrates the roughly constant addition of background events.

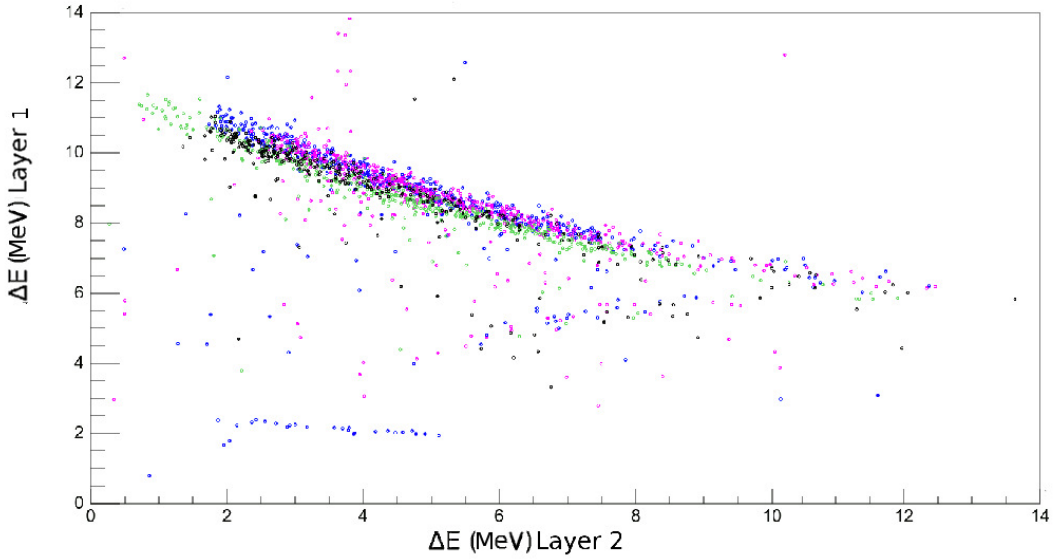

FIGURE 5.8. Proton relative energy losses in subsequent layers of Si with colors reflecting the four telescopes. No selection of desired events via gating around the TAC peak has been done. Some discrepancy between the four telescopes is expected within the resolution, but additional inconsistencies exist due to issues with the thin 100 μm QQQ5 detector in the first layer, discussed in Section 5.2. The smaller, intersecting line diagonal to the main line is proton events which did not lose all their energy in the final detector layer.

5.9, with events selected to be within the time gate of the TAC peak, shows many of the detected events lying outside of the particle group are culled from the spectrum. Additionally, we can perform the same analysis on data collected from a ^{37}K projectile with a ^{12}C target, a setup that is designed to mimic background events due to the carbon in the C_3H_6 target. Fig. 5.10 shows the coincidence between heavy recoils in the IC and fusion-evaporation products detected in the silicon. We compare this peak to the one collected for the main experimental runs from Fig. 5.5 and find that the events are mostly constant over the TAC range. There is a small peak, but it is not significantly above the baseline, and it is at the edge of our 12700-13600 TAC time gate. Finally, we examine relative energy loss plots for these fusion evaporation products, shown in Fig. 5.11. Applying the same TAC gate of 12700-13600 as we did above in Fig. 5.9, gives Fig. 5.12, and we see that many of these products are removed from the spectrum.

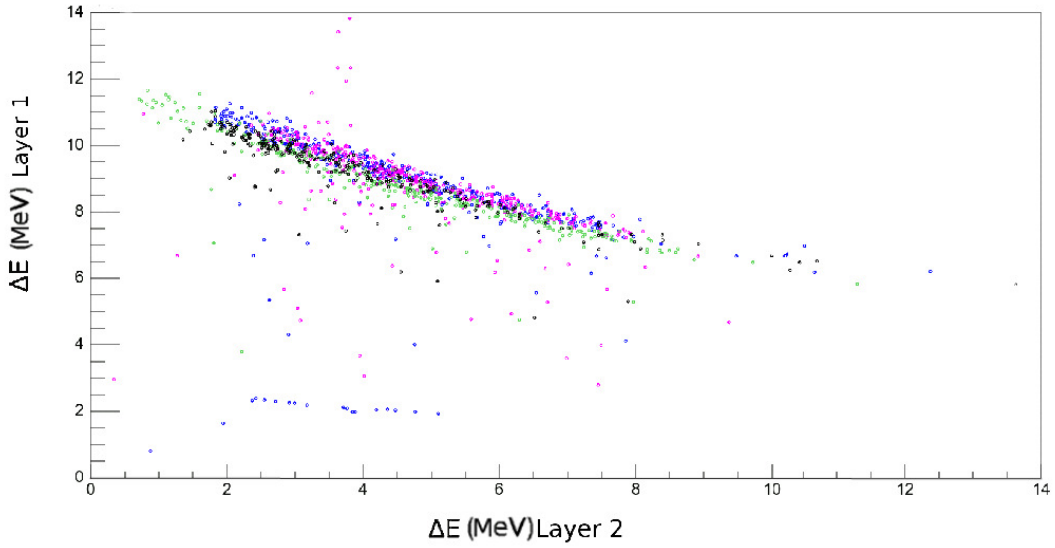

FIGURE 5.9. The identical spectra to Fig. 5.8 with a time gate identified by the TAC peak used to select coincident events corresponding to the ^{37}K+p.

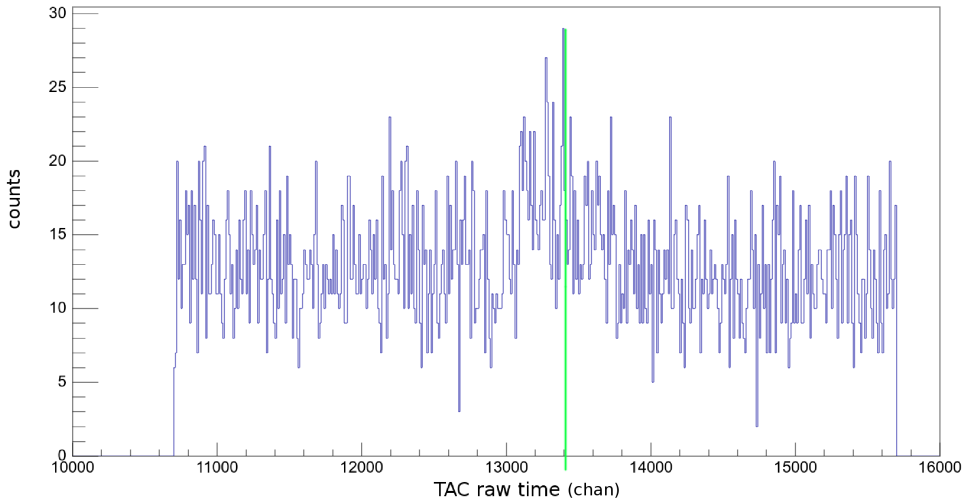

FIGURE 5.10. A raw (uncalibrated) spectrum of TAC values for the ^{12}C fusion evaporation events taken during runs of a ^{37}K beam incident on a carbon target, intended to calculate background. Though this spectrum does have a peak above baseline, it is minimal and at the edge of the 12700-13600 TAC gate region selected for the experiment. This helps confirm we are selecting only the events of interest during the main experiment. The vertical green line shows the approximate location of the peak, which is well outside the chosen TAC gate range.

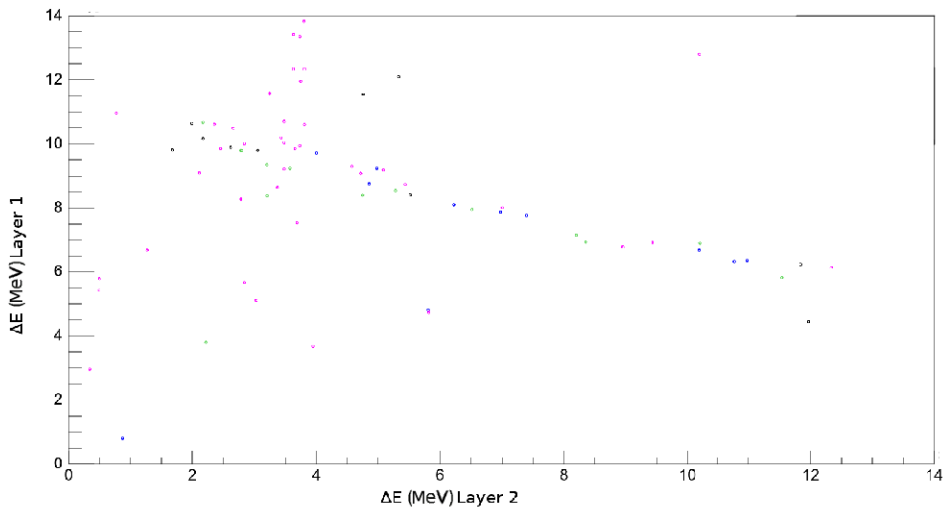

FIGURE 5.11. Fusion evaporation product relative energy losses in subsequent layers of Si with colors reflecting the four telescopes. No removal of undesired events via gating around the TAC peak has been done.

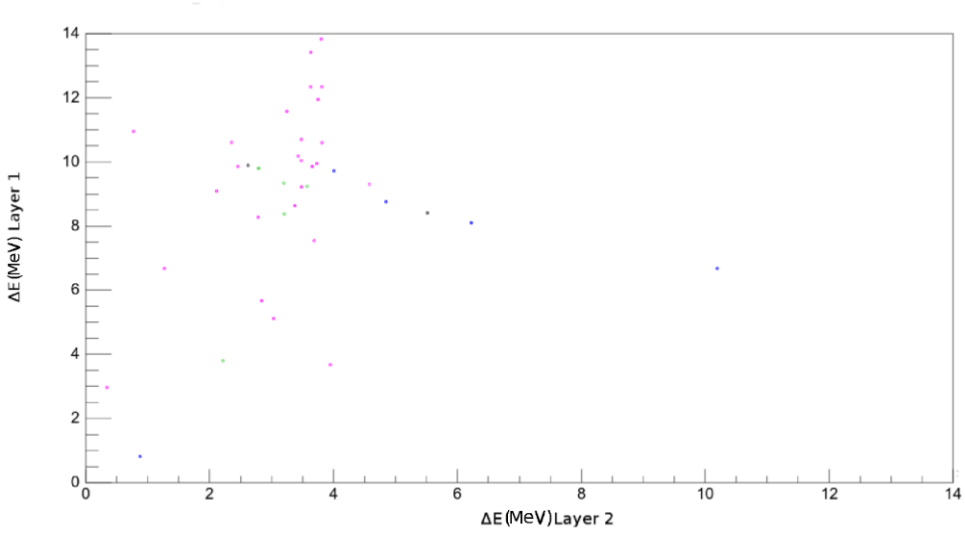

FIGURE 5.12. The identical spectra to Fig. 5.11 with the time gate identified by the TAC peak applied to remove $^{12}C + p$ fusion evaporation products.

Due to some experimental settings, additional corrections were needed to assure that the data fully represented the physical conditions. The thresholds of the detectors, each set individually, were well above the expected minimum value of event signals, and the electronic noise in the detectors. As a result, a range of events needed to be eliminated due to incomplete energy loss information. These events lost energy in both 1-mm layers of a single telescope, but the loss in the second layer was below the threshold value. The energy loss in a single layer in the center-of-mass frame varies with laboratory angle as seen in Fig. 5.13. The missing region of energy is indicated in Fig. 5.14, with red arrows showing examples in channels 2, 5, and 11. In order to compensate for this in the QQQ3 model telescopes, a range of 600 keV corresponding to the threshold value was cut from the data, staggered increasing with each of the 16 channels. An example, represented by Fig. 5.15, reflects the condition at 3200 keV, where channels 1-8 would be removed from the spectrum, while 9-16 would be included. The same method is applied throughout the cut region. This correction resulted in much lower statistics and higher relative uncertainty for the region in question, corresponding to ~7.9-8.3 MeV in the excitation function. This region is currently not considered reliable and has considerations for the final spin assignment analysis discussed later in this chapter.

The removed data must be accounted for in the final analysis. The detector strips correspond to angular coverage in the detectors, so in order to account for these missing events, the solid angle was adjusted to reflect the missing channels. Geometric efficiency is a quantity used within the differential cross section calculations, discussed in Section 5.4. Missing channels such as Ch. 8 seen in Fig. 5.14 record no data, so it is sufficient to remove the corresponding angular coverage value.

The QQQ5-model, 3-layer telescopes required an additional correction. The first layer was 100 μm thick. Since energy deposited goes inversely with incident energy, protons from ^{37}K+p scattering with high enough energy to be detected in all three sections would

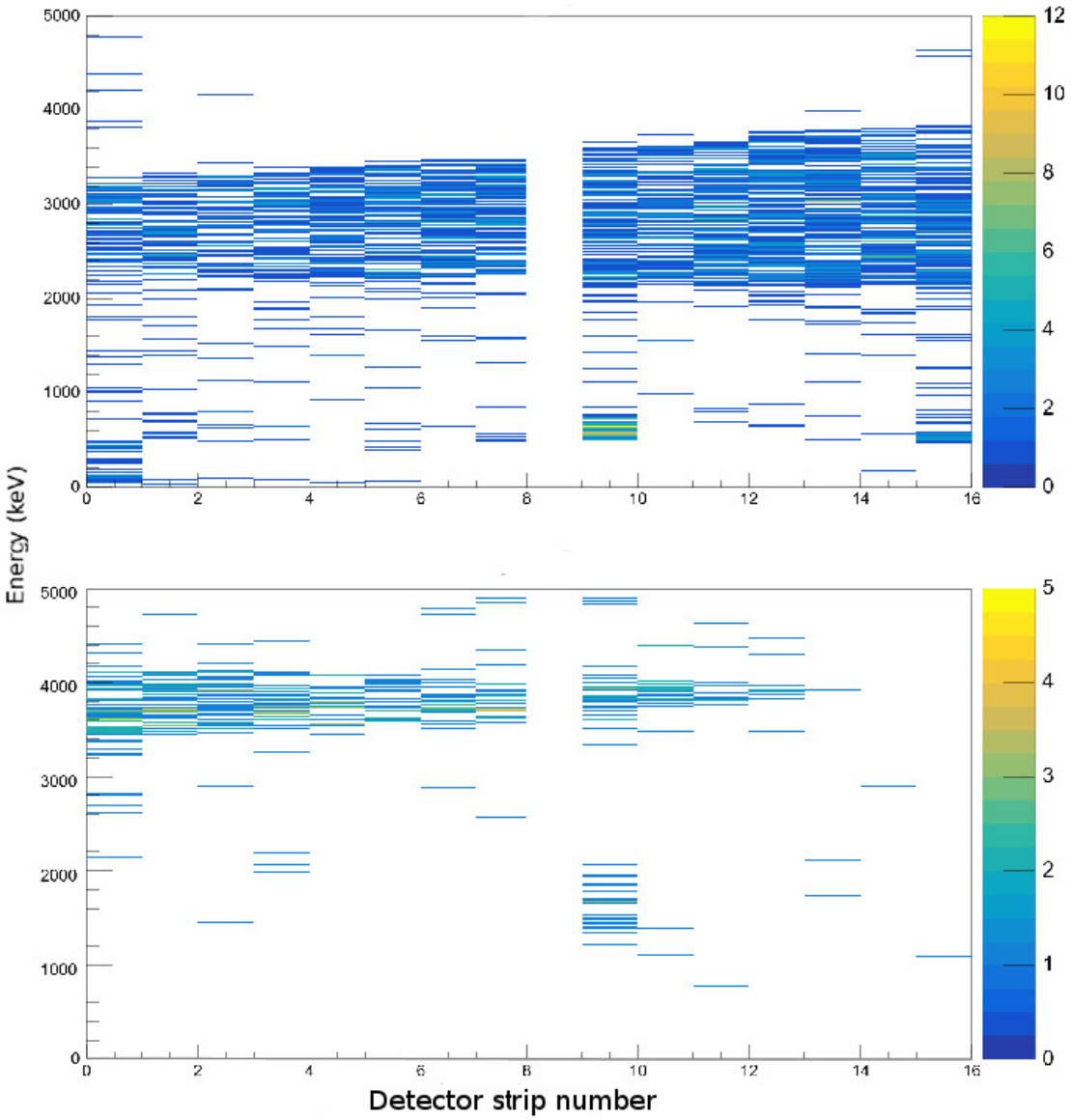

FIGURE 5.13. Two spectra showing center-of-mass energy as a function of channel from the same telescope as Fig. 5.14. This shows the events detected only in the first layer (Top) and events detected in both first and second layer (Bottom), which both fill a different region of the spectrum, but when added together are expected to fit together to make a contiguous combined spectrum. Each channel has a specific angular coverage, and the channels are numbered from the center of the telescope array outward. The combined spectrum and the gap in the information can be seen in 5.14.

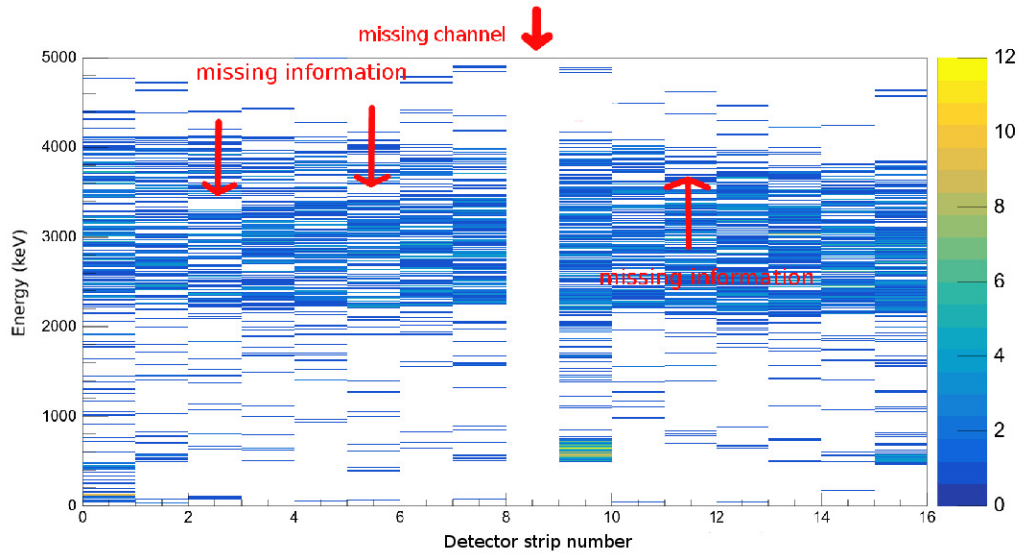

FIGURE 5.14. A spectra showing center-of-mass energy vs detector strip number in one two-layer QQQ3 telescope. The arrows show the missing information region, and a missing channel, both of which must be accounted for in the $d\Omega$ calculations in the differential cross section ($\frac{d\sigma}{d\Omega}$).

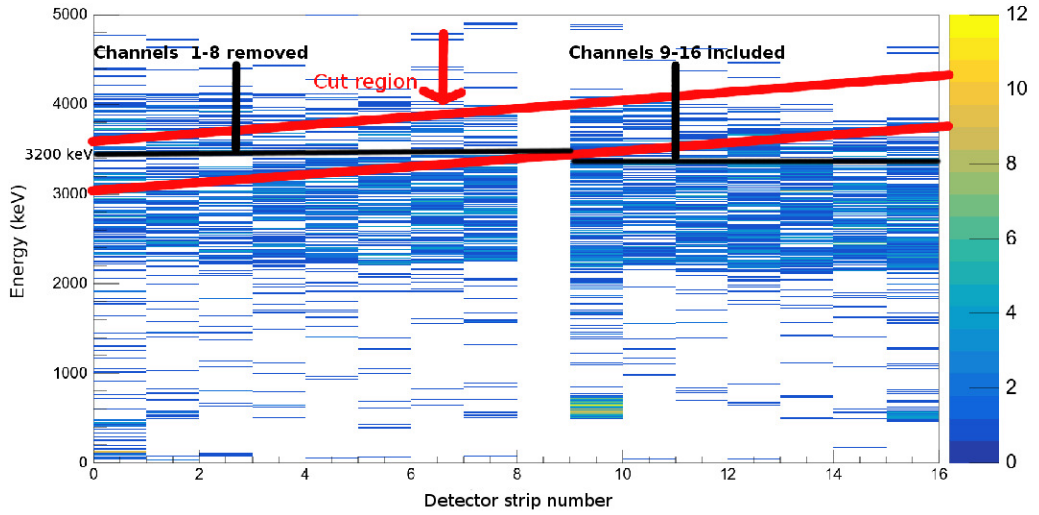

FIGURE 5.15. The same spectra as Fig 5.14. Events from the region between the red lines were removed from the spectra, and the corresponding channel was removed from the total angle in the $d\Omega$ factor, discussed in Section 5.4.4.

lose less than 240 keV in 100 μm of Si. This was below the threshold value for these two detectors. Any event that deposited energy in the second and third layer must also deposit energy in the first, but almost no events with coincidence in all three layers were detected. Rather, most were coincident in either the first two layers or the final two. Thus we must conclude that events coincident in only the final two layers had some quantity of energy missing from the total. The data for the experiment was thus split into two regimes: those occurring in the two-layer, QQQ3 telescopes, and those in the three-layer, QQQ5. In the QQQ5 telescopes, events which only recorded coincidence in the first two layers were separated from those coincident in the second and third layers, while any energy detected in the first layer was ignored. Constant corrections were added to the two regimes of first-second layer and second-third layer, 60 keV and 260 keV, respectively. This correction was the average energy lost in the 100 μm detector, with differences within the resolution of the experiment.

The background from the ^{37}K+^{12}C fusion evaporation is presently accounted for, however, there are several beam contaminants including ^{37}Ar and ^{37}Cl that can also interact with the polypropylene target. Additional experimental time was taken to explore these effects using dedicated beams of these species. This data is still under analysis.

5.3 Kinematic Reconstruction

The information collected from the Si detectors is the proton energy and angle, and we need to convert this to the center-of-mass frame, for reasons discussed in the previous chapter. This value is found by applying trigonometric identities to the geometric construction of the scattering angles in lab and center-of-mass frames, seen in Fig. 5.16. Following the derivation in [45], we get the following conversion formula:

$$E_{c.m.} = \frac{E^p_{lab}(m_k + m_p)}{4(m_k)cos^2(\theta)} \tag{5.1}$$

where E^p_{lab} is the proton energy in inverse kinematics in the lab frame, m_p is the proton

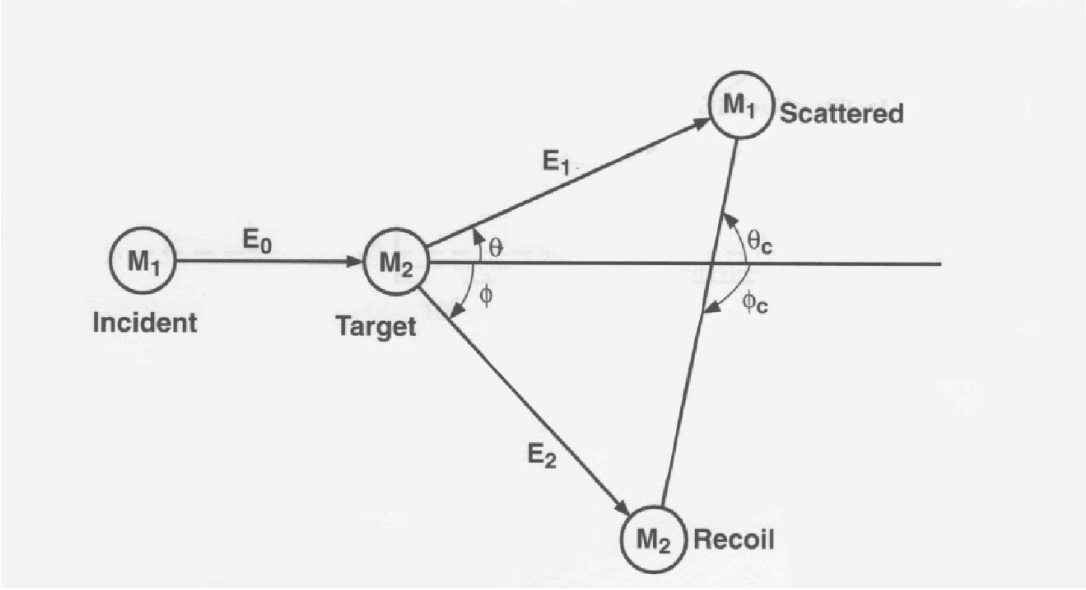

FIGURE 5.16. Geometric construction of scattering angles, where E_0 is the beam energy in the lab, M_1 is the projectile, M_2 is the target, E_1 and E_2 , θ and ϕ, and θ_c and ϕ_c are their respective scattering energies, angles, and c.m. angles. In the case that $M_2 > M_1$, limits are placed on the angles that θ and θ_c can take on. Taken from [45] .

mass, m_k is the mass of ^{37}K, and θ is the proton angle in the lab frame in inverse kinematics. Applying this to the proton lab energy spectrum gives the excitation spectrum seen in Fig. 5.17. In addition, we can reconstruct the approximate measured energy range from the beam energy and energy loss in the target. The 4.448 MeV/u ^{37}K beam loses approximately 1.895 MeV/u in the polypropylene target, as calculated using LISE++ [44], for a remaining energy of 2.569 MeV/u, so we can expect interactions to happen over this range of values. Converting to the c.m. frame requires a factor of m_p/m_k, this corresponds to an energy range of 2.52-4.38 MeV, and a range of excitation energies of 7.14-9.04 MeV, for a total range of 1.9 MeV. The observed range of excitation energies is approximately 6.7-8.5 MeV, which is inconsistent with the value calculated from the beam energy, and is presently not understood. Known sources of energy loss have been analyzed and accounted for. The α calibration calculation has an inherent correction caused by a “dead layer” before the active area of the Si detectors, which results in an energy loss that is not recorded. This results in a difference in the recorded α energy of

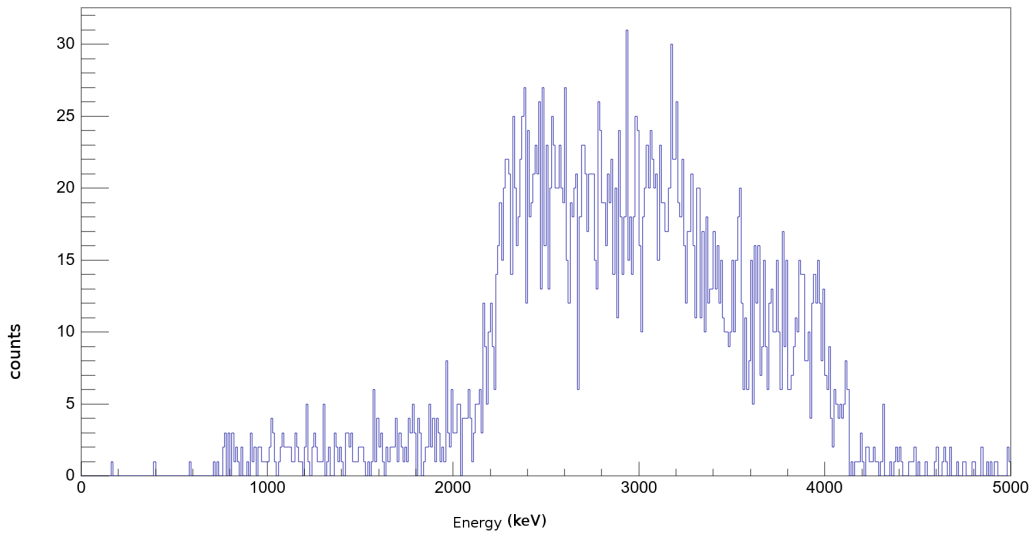

FIGURE 5.17. An excitation function for one telescope of the 2-layer QQQ3 Si detectors, with the number of elastically scattered protons in the y axis, and energy in the x axis, in the center-of-mass frame.

~ -120 keV at the decay peak energy value of 5.485 MeV. The subsequent correction in energies of $\sim$ 11 MeV is ~240 keV. Also, the scattered protons lose a range of energies in the target depending on the location of the interaction, such that those that scatter at the front, upstream end of the target can lose as much as ~120 keV compared to those scattered at the downstream end of the target. Since these two energy loss corrections are of similar magnitude but opposite sign, the combined effect is to minimize both, with a total correction of ~0-120 keV, or ~0-30 keV in c.m., and thus these cannot be the source of the discrepancy. Additional analysis is underway to determine if the calibration can be independently confirmed via data collected during runs with the ^{40}Ar stable beam on the CH_2 target. Proton scattering on ^{40}Ar is well studied going back more than 50 years [46] [47]. Additionally conditions that might change the beam energy, such as a microchannel plate foil being in the beamline, are also being investigated.

5.4 Differential Cross Section

The goal of the ROOT analysis is to provide one of the important quantities discussed in Sec. 2.6, the proton yield as a function of $E_{c.m.}$ needed to determine the cross sec-

tion. For the R-Matrix analysis we need the differential cross section as a function of energy, $\frac{d\sigma(E)}{d\Omega}$. This spectrum will have features corresponding to the excited states in the ^{38}Ca compound nucleus and resonances of the $^{34}\mathrm{Ar}(\alpha, p)^{37}\mathrm{K}$ reaction. We expect peaks, troughs, and multiplets, and the locations and widths of these features will later be used in the R-Matrix analysis to identify resonances. First, however, we need to convert from the excitation function of the previous section to the differential cross section, $\frac{d\sigma(E)}{d\Omega}$.

$$\frac{d\sigma}{d\Omega} = \frac{(\text{Yield})}{(\text{Incident})(\text{Target})\Delta\Omega}\left[\frac{cm^2}{srn}\right], \tag{5.2}$$

where the yield is the number of counts in each energy bin, the incident is the total beam counts, the target is the areal target density, or target nuclei per area, and $\Delta\Omega$ is the solid angle covered by the detectors. The following unit conversions and calculations were applied to convert from an excitation function to differential cross sections.

5.4.1 Yield

The "yield", or number of counts in each energy bin, is given by the y axis value of a single bin in the excitation function spectrum. It is the total number of events possessing that range of energies in the center-of-mass frame for a given bin size and value. An example is in Fig. 5.18. This component has units of counts.

5.4.2 Incident

The "incident" is the total number of beam ions incident on the target for the length of the experiment, multiplied by the purity found during runs with no target where the uninhibited beam was collected in the IC, as seen in Fig. 5.19, which was found to be 85%. The beam counts were events measured in the IC. This component has units of counts.

5.4.3 Target

The "target" is the areal target density determined via

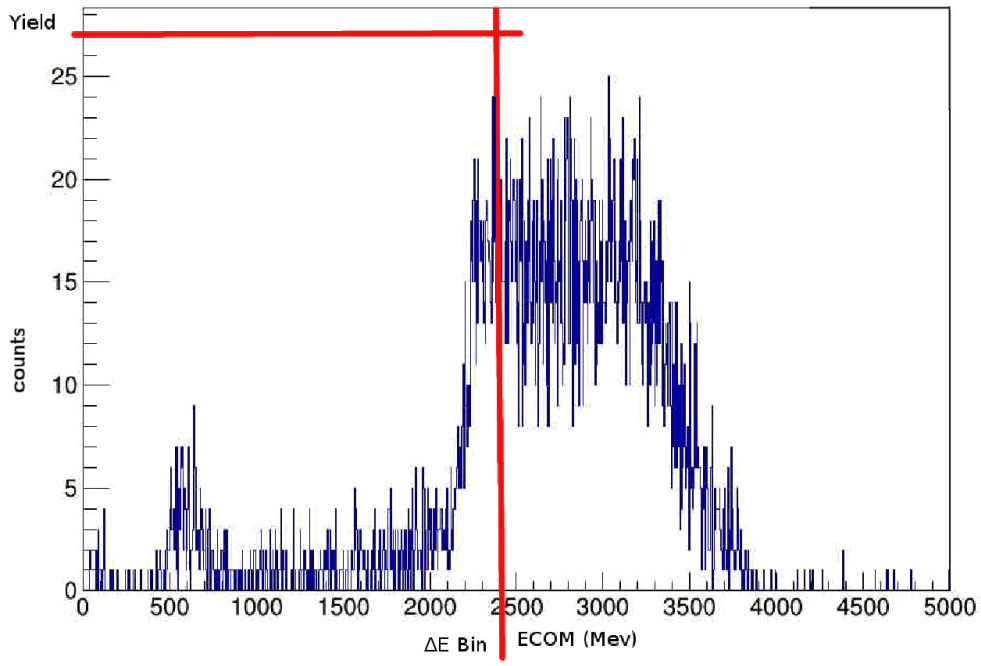

FIGURE 5.18. An example yield for a single bin in the excitation function. Bin size for this spectrum is 5 keV.

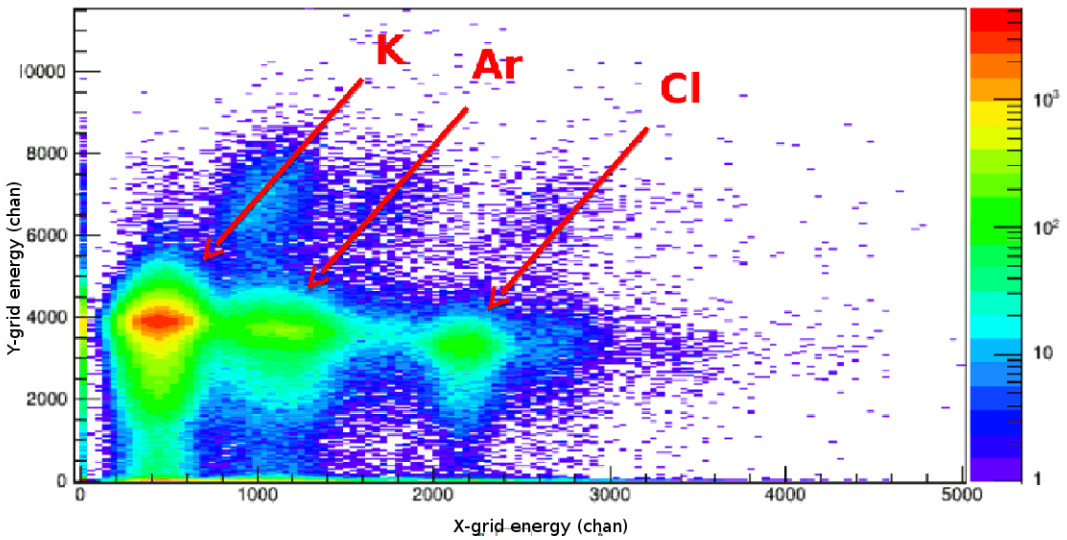

FIGURE 5.19. Beam components, ^{37}K, ^{37}Ar, and ^{37}Cl counted in the ionization chamber. From this data the beam purity was calculated at 85%.

$$\text{Target} = \frac{\Delta E * N_H}{S(E)} \frac{E^K_{lab}}{E_{c.m.}} \left[\frac{1}{cm^2}\right] \tag{5.3}$$

where ΔE is the bin size in keV in the center-of-mass frame, N_H is the number density of hydrogen in the target, $S(E)$ is the stopping power of the target in keV in the lab frame, and $\mathrm{E}^K_{lab}/\mathrm{E}_{c.m.}$ is a conversion factor.

The bin size was 5 or 10 keV, chosen to maximize data representation while emphasizing trends.

Stopping power $S(E)$ is a function describing the energy loss of the ^{37}K beam per unit of thickness, in the target material as a function of beam energy. Combined with the bin size and number density of the target material, this allows us to calculate the areal density of the target atoms in an energy bin, one of the quantities in the denominator of $\frac{d\sigma}{d\Omega}$. However, the energy loss of a nucleus through a material is an estimation based on experimental values, with numerical approximations to extrapolate outside measured regimes, so we use these theoretical calculations to estimate the value. Such calculations are material specific. The energy loss per unit thickness is not constant, but is a function of projectile energy and must be calculated in steps as it progresses through the target. Various software packages exist to assist in this task, and LISE++ was used in this case, with its Physical Calculator utility. The beam energy in MeV/u in the lab frame is given as an input, along with the target material and thickness, chosen at 1 μm for simplicity of units. The beam energy was varied in steps of 100 keV over the experimental energy range. The energy loss for each value was recorded. The plot in Fig. 5.20 shows that the energy loss values over the experimental energy range was a well behaved function and is well approximated by a 2^{nd} degree polynomial,

$$S(E) = 1.9481x10^{-5}(E^2) - .3924(E) + 3446, \tag{5.4}$$

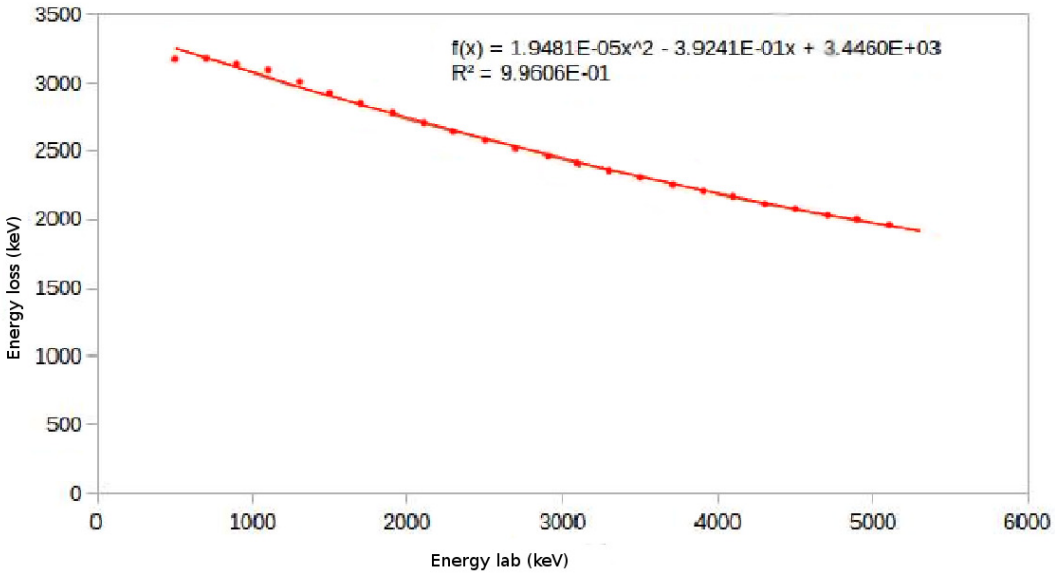

FIGURE 5.20. LISE++ energy loss data points for a range of values in the region of interest and a 2^{nd} degree polynomial approximation of the trend, with the fitting parameter R^2.

with an $R^2 = .9960$. This component has units of keV/cm.

The bin size (Δ E) is in the center of mass, while the stopping power ($S(E)$) is in the lab frame, so the factor $E_{c.m.}/E^K_{lab}=\frac{m_p}{m_p+m_k}$ was used to normalize these scaling factors, where the individual masses are in atomic mass units. This factor is unitless.

The number density of hydrogen (N_H) in the target is calculated as follows:

$$N_H = \frac{\rho(C_3H_6)}{\rho_{mol}(C_3H_6)}\frac{N_A}{mol}6H, \tag{5.5}$$

$$\rho(C_3H_6) = \frac{.95g}{cm^3}, \tag{5.6}$$

$$\rho_{mol} = \frac{42.08g}{mol}, \tag{5.7}$$

$$N_H = \frac{\rho(C_3H_6)}{\rho_{mol}(C_3H_6)}, \tag{5.8}$$

$$N_H = \frac{.95g}{cm^3}\frac{1mol}{42.08g}\frac{N_A molec}{1mol}\frac{6H}{molec} = .1354N_A\frac{H}{cm^3}. \tag{5.9}$$

This factor has units of H/cm^3.

5.5 $\Delta\Omega$

$$\Delta\Omega = \int_{\theta_1}^{\theta_2}\int_{\phi_1}^{\phi_2} sin\theta d\theta d\phi * \epsilon. \tag{5.10}$$

The value of $\Delta\Omega$ was calculated using the detector schematics and measurements listed in Ch. 4 and Appendix A in order to determine the angular coverage of each channel segment of each detector. The segment values were then added together for a total angular coverage. This was useful in particular in the case of the cut and corrections discussed in Section 5.2, where individual channels were removed over a given energy range in order to account for a threshold set above the necessary and expected energy minimum. It must be noted that since the detectors are planar, their position does not correspond to a perfect 2D projection onto the radial sphere concentric with the target. However, the corrected values and the estimated values from the flat geometric assumption matched to .1%, and thus were within the tolerance necessary for this analysis. This component has units of steradians.

Geometric efficiency (ϵ) is a factor applied to the angular coverage $\Delta\Omega$ to account for the actual active area of the detectors with respect to the ideal value of 100% coverage, and is included to account for the regions between detectors. This value was set at 95% based on schematics in Appendix A. This component is unitless.

5.6 Cross Section Uncertainty

Following the method given in Taylor [48], the statistical uncertainty was calculated by replacing the yield in Eq. 5.2, so that

$$\delta\left(\frac{d\sigma}{d\Omega}\right) = \frac{\sqrt{(\text{Yield})}}{(\text{Incident})(\text{Target})\Delta\Omega}\left[\frac{cm^2}{srn}\right]. \tag{5.11}$$

The statistical uncertainty dominated over any systematic uncertainty.

5.7 R-Matrix fitting

The cross section extracted from the experiment was used in the phenomenological R-Matrix theory calculation. R-Matrix methods are useful in analyzing measured cross sections for particle scattering on nuclei to extract values for the quantities E_r, J^π, and Γ_i, which are used in the reaction rate calculation via Eq. 2.25, except the quantity Γ_α, which is not available from the R-Matrix analysis of the proton channel. Applications include calculating resonance level properties, as well as extrapolating cross sections from the higher energies often measured in experiment, to the lower energies prevalent in the astrophysically relevant regimes. The R-Matrix code AZURE2 was designed to expand the application and use of R-Matrix methods beyond the specialized codes of experienced practitioners to broader multi-channel calculations for the general user [49]. It was designed following the formulation of Lane and Thomas [50] to solve the coupled wave equations of nuclear interactions and uses least-squares minimization routines provided by the ROOT package MINUIT2 [43] to minimize the deviation from input data. The inputs are the incoming particles, Q-value, and channel radius. The user may specify known or theorized resonances and provide their spins and partial widths, either with an experimentally measured or theoretical value. These quantities can either be fixed by the user or varied by the code to optimize the fit even more. The user may also provide experimental cross section data in an input file, with the following information for each data point: kinetic energy, angle, cross section, and cross section error, all in forward kinematics in the laboratory frame.

Following the derivation of [51], the R-Matrix refers to a matrix of the entrance and exit channels applied to solutions of the scattering wave function. The physical space is divided into the interior region, and its spherically symmetric potential $V(r)$, and the exterior region, with a Coulomb potential approximation:

$$V_C(r) = \frac{Z_1 Z_2 e^2}{4\pi\epsilon_0 r}, \tag{5.12}$$

and a fictitious channel divides the two regions, which is placed at an estimate of the nuclear radius. For the exterior region we assume a wave function of separable products and follow a scattering partial wave analysis, we start with the single channel case, and solve the radial Schrödinger equation for a Coulomb potential. This separable wave function is given by:

$$\Psi(r, \theta, \phi) = u(r) Y_{lm}(\theta, \phi). \tag{5.13}$$

So that the Hamiltonian is

$$H_l = T_l + V(r) \tag{5.14}$$

where

$$T_l = -\frac{\hbar^2}{2\mu}\left(\frac{d^2}{dr^2} - \frac{l(l+1)}{r^2}\right) \tag{5.15}$$

as usual. We solve the radial equation and find the solutions in the general form as

$$u_l(r) \rightarrow_{r\rightarrow\infty} I_l(\eta, kr) - U_l O_l(\eta, kr), \tag{5.16}$$

Where $I_l = G_l - iF_l$ and $O_l = G_i + iF_i$ where G and F are the irregular Coulomb functions, and η is the Sommerfeld parameter from Eq. 2.10. The scattering matrix, with δ as the phase shift, is

$$U_l = e^{2i\delta_l}. \tag{5.17}$$

We invoke the boundary conditions

$$u_l(0) = 0, \tag{5.18}$$

$$u_l^+(a) = u_l^-(a), \tag{5.19}$$

and

$$u'^+_l(a) = u'^-_l(a). \tag{5.20}$$

The R matrix at energy E then is defined by the inverse logarithmic derivative

$$R(E) = \frac{u(a)}{au'(a)}, \tag{5.21}$$

where a is the chosen channel radius. For the entire scattering function R-Matrix, we assume that $u_i(r)$ is a linear combination of N states (for N resonances)

$$u_i(r) = \Sigma_{n=1}^{N} A_n w_n(r) \tag{5.22}$$

that satisfy the following condition for some eigenvalue ϵ,

$$\left[\hat{T} + V(R)\right] w_n(r) = \epsilon_n w_n(r) \tag{5.23}$$

where w_n is an orthonormal set on the range [0,a]. The R-Matrix then becomes

$$R(E) = \Sigma_{n=1}^{N} \frac{\hbar^2}{2\mu a} \frac{w_n(a)^2}{\epsilon_n - E}. \tag{5.24}$$

We first fit to our experimental cross section using E_r values corresponding to those recently measured in Long *et al.* and listed in Table 3.1 [28], with J^π set to 2+, the spin most like populated via proton scattering. From there, each resonance was "tuned" individually with successive fit calculations by testing each of the accessible natural parity spins: 0^+, 1^-, 2^+ ,3^- ,and 4^+. The spins of the reactants, ^{34}Ar and α, are both 0^+, and therefore selection rules demand that only natural parity states are populated

in the compound nucleus. Also, the experimental setup from Long *et al.* involving the ^{40}Ar$(p,t)^{38}$Ca reaction has the same natural parity restriction. The intention was to examine the resulting partial widths and the fit using the goodness of fit statistic χ^2, to determine the optimum result. AZURE2 calculates a modified for χ^2, adapted for nuclear experiment from [52]:

$$X^2 = \sum_i \Big(\sum_j \frac{(f(x_{ij}) - c_i n_i y_{ij})^2}{(c_i n_i \sigma_{ij})^2} + \frac{((c_i - n_i)/n_i)^2}{\delta^2_{c-exp,i}} \Big) \tag{5.25}$$

where c_i is the normalization fit parameter, n_i is the starting normalization, $f(x_{i,j})$ is the calculated quantity from the R-matrix (i.e. cross section, S-factor, phase shift, etc.), $y_{i,j}$ is the data point value, $\sigma_{i,j}$ is the statistical uncertainty of the data point, and $\delta_{c-exp,i}$ is the percent systematic uncertainty of the data set [49]. The derived statistic χ^2/N, where N is the number of data points, was also used. Note that if the statistical uncertainty dominates, this quantity reduces to the standard χ^2.

Since the E_r values are known to a good accuracy, these were fixed in the code. With each fit, the spin assignments were also fixed, however, the partial widths were not fixed. The 2 or 3 best fit spin assignments were also earmarked, for use in the second iteration of the method. This method, while systematic, was possibly underconstrained in the context of fitting multiple coupled equations with parameters and input data as AZURE2 does. The χ^2 statistic is meant to calculate the deviation of the data and the input parameters, such as E_r, or partial widths, from the expected values. AZURE2 takes these values as inputs and allows the code vary them when needed to achieve a better fit. When these values are fixed and not allowed to vary, the calculation essentially reduces to a pure analysis of regression from the data. When the parameters are allowed to vary, the χ^2 can be artificially affected when the best-fit values found by the code vary significantly from the input value. As this method has many free parameters, the χ^2 value

was extremely sensitive to initial conditions and overall it was difficult to judge which spins were the optimum values. Even so, when choosing the best values found via this method, the fit did not improve on the original naive baseline with all states set to 2^+.

A second method was devised, beginning again from the original baseline described above, which successive attempts had not been able to improve upon. By visual inspection of the fit compared to the data it was clear that some of the states were already well represented by the 2^+ assignment. As the experiment by Long *et al.* could populate only natural parity states, and other states would almost definitely be populated in ^{37}K+p scattering, it was necessary to find a way to account for possible additional resonances. Also, it must be noted there is a ~300 keV region in that work in which no resonances were detected, from 7.5-7.8 MeV, though additional resonances may exist there. The best method found was to add approximately 1 resonance for every MeV with an initial guess for E_r where a possible visually-identifiable feature existed. The resonance energy was left variable and they were assigned a non-natural parity state. AZURE2 put these to good use and located several possible resonances corresponding to apparent visually-identifiable features, including one at 7.549 MeV, which may match with the single feature in O'Brien *et al.* that does not appear to correspond to a resonance in Long *et al.* Indeed, this feature exists in the ~300-keV gap between known levels at 7.480 MeV and 7.800 MeV discussed earlier. An additional possible resonance corresponding to 6.911 MeV was also located in this manner. These additional resonances not only improved the local fit, but greatly improved the overall fit of the other resonances as measured with the goodness of fit statistics. Without them the best-fits tended toward linearity and were locally featureless, as this is the best-fit without additional constraints. The states that were still poorly described by the fit after these steps were then tested with other possible spin values to arrive at the best combination of visual quality and χ^2 value. The

results of this method were sufficiently successful to proceed to a second iteration with more stringent metrics.

In this iteration, the best-fit J^π assignments and widths of the initial fit were fixed for the entirety of the process, unless they were presently under examination. Then each resonance was tested individually. The J^π states were varied over all possible natural parity values. Because there is no parity restriction on resonance levels identified from p scattering, the possible new resonances could theoretically have any J^π value, though would not contribute to the ^{34}Ar$(\alpha, p)^{37}$K reaction rate. The χ^2 values for each fit were recorded in order to identify the best, or several best-fits. However, even in this second iteration where most of the parameter values were fixed, the coupled equations being solved are under constrained. Therefore, smaller variances in χ^2 cannot purely be explained by the goodness of the fit and other metrics must be included when considering confidence in the spin assignment found. The spin value of an existing resonance was considered clearly identified when the total χ^2 was more than 3 less than the next best-fit. In cases where the χ^2 of two or more spin assignments were within 3 of the best-fit, several conditions were evaluated. First, the partial width was considered. We expect from the resolution given in Long *et al.* that the resonances identified in that work have widths less than ~100 keV. Assignments with values considered reasonable against this threshold were prioritized. An extremely large partial width may indicate the code is attempting to fit the resonance to the data by smearing it over a large range. This indicates that the conditions required to fit the parameters to this state fit the data only when it is essentially removed. Resonances with 3 or more spin assignments within the χ^2 range of 3 and/or resonances where no reasonable partial widths were found, were additionally tested to evaluate the χ^2 value when the resonance was removed entirely. All possible new resonances were also tested without the resonance included in the fit. The visual quality of the plotted fit was also considered, but as it is a somewhat subjective metric, it

cannot be used as a definitive determination and the only conclusion that can be drawn in that case is that further study is required. Therefore, in this iteration the primary metrics of a good fit for each resonance were the χ^2 calculation as well the partial widths. Since Long *et al.*'s experimental resolution made it unlikely that resonances detected in his work had a width of greater than 100 keV, a value >>100 keV was suspect under this metric. At this stage, it was also possible to account for experimental uncertainties in the R-Matrix analysis. The intrinsic angular resolution is determined by the width of channel strips in the detectors, as well as the beam spot. Together these give an uncertainty of ~110 keV. The resolution of the α calibration is determined by the FWHM of the peak recorded during calibration experimental runs (e.g. Fig. 5.2). This gives an uncertainty of ~80 keV. Added in quadrature gives a propagated uncertainty of ~136 keV in the lab frame, which is ~38 keV in the proton lab frame. These experimental uncertainties are accounted for in AZURE2 by "smearing" the cross-section experimental data by weighting each point and the neighboring points with a Guassian, peaked at the current value as it is being analyzed. The propagated uncertainty value of ~38 keV gives a σ for this Gaussian weighting of ~17 keV.

An uncertainty calculation, also performed in AZURE2, utilizes the MINOS minimization routine, available in MINUIT2 to calculate the uncertainty of the E_r values as well as the partial widths [49]. These uncertainties can be used to quantify the uncertainty in the reaction rate calculated via Eq. 2.26 with these parameters. The error analysis is still in progress.

5.8 The Resonances

Using the R-Matrix analysis we were able to make spin assignments on ten resonance levels identified in Long *et al.* above the α threshold, with varying levels of confidence. Four additional possible levels were identified by visual inspection and computation by AZURE2, from features in the excitation spectrum. After final analysis, four of the levels

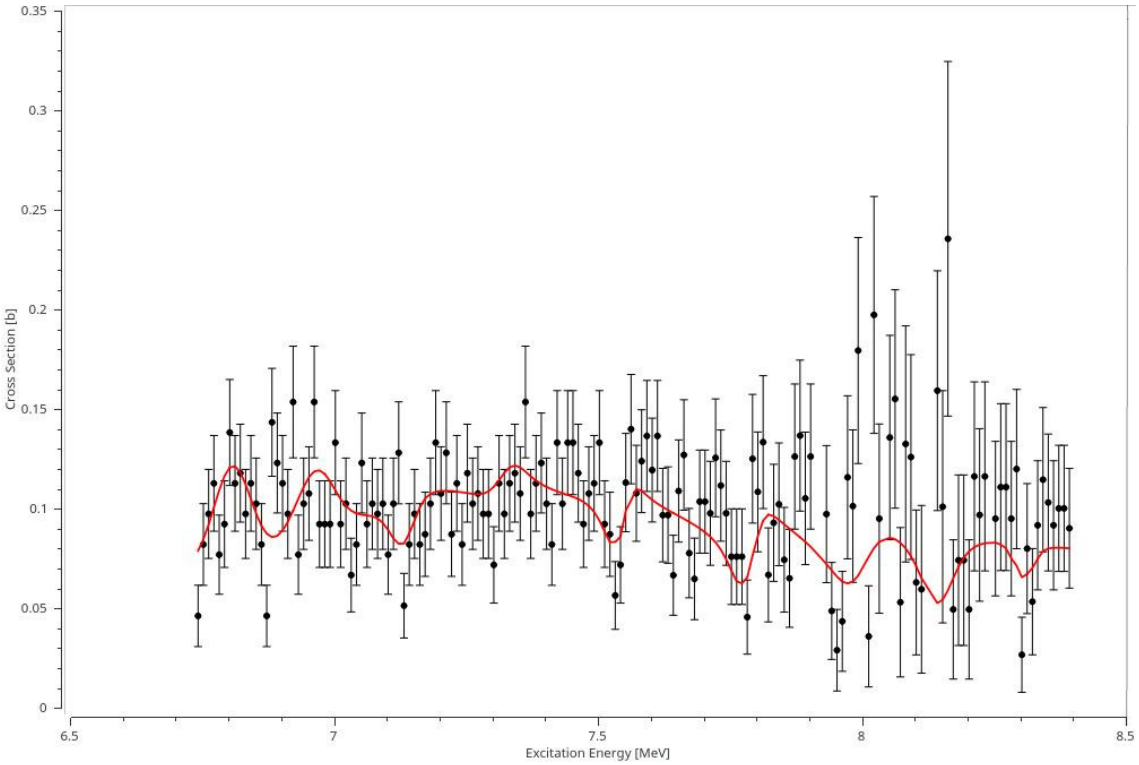

FIGURE 5.21. This plot shows the experimental cross section data as the black points, with their related uncertainty. The red curve is the cross section calculated by AZURE2 from the values given by the analysis.

were identified with high confidence, as well as one additional possible level. This is the primary result of this work. The table in Appendix A reviews the information given in the following sections. Figure 5.21 shows the plotted cross section in c.m., along with the cross section fit as constrained by the parameter values found in the AZURE2 best-fit.

5.8.1 Levels with High Confidence

Several resonances, when fit with AZURE2's R-matrix methods described in Section 5.7, gave evidence of conclusive J^{π} values and partial widths.

The 6772-keV level has been assigned a spin of 2^{+} for this work, with a χ^2/N value of .9489. The next best-fit for the level was the 1^{-} spin, with a χ^2/N value of 1.1782, and a χ^2 difference of ~37, giving high confidence in this spin assignment.

The 7041-keV level has been assigned a spin value of 2^+, with a χ^2/N value of .9380. The next best-fit for that level was 1^-, with a χ^2 difference of 14.14.

The 7176-keV level has been assigned a spin of 2^+, with a χ^2/N value of .9270. The next best-fit level was 1^-, with a χ^2 difference of 15.32.

The 8322-keV level has been assigned a spin of 2^+, with a χ^2 value of .9220. The next best-fit level was a 1^-, with a χ^2 difference of 7.94.

5.8.2 Levels with Several Compatible Fits

Six levels were confidently identified in the cross section data, but R-Matrix fitting was inconclusive as to the J^π, or spin assignment, with more than one value demonstrating possible compatibility using the metrics discussed in Section 5.7, χ^2 and partial widths.

The resonance at 6950 keV has possible spins identified as 0^+ or 2^+, with χ^2/N of .9489 and .8827, respectively, and a difference of χ^2/N of 10.52. However, the latter spin assignment of 2^+, while possessing a superior χ^2 was found by AZURE2 to have partial width above the 100 keV threshold, at ≈170 keV, than the 0^+ spin assignment at ∼43 keV. Figure 5.22 shows a comparison of the fits plotted with the two different spin assignments. While visual inspection is not a satisfactory final metric, the fitted cross section using a 0^+ assignment does appear to better describe the peak around the location of this resonance. Additional study is necessary. For the purposes of the reaction rate calculated later in this chapter, the value of 0^+ has been adopted.

The resonance at 7370 keV has two best-fit spin assignments, that of 2^+ with χ^2/N=.8975 and 1^- with χ^2/N=.9168, and with χ^2 difference of 3.07. Both were found by the code to have partial widths well above the 100 keV threshold, at 212 keV for 2^+ and 136 keV and for 1^-. In light of these widths above the 100 keV threshold, a further analysis with the resonance removed did indicate that a satisfactory fit was found with the resonance removed with χ^2/N of .9925. This is the only resonance state from Long *et al.* that met this condition. This resonance is not included in the rate calculation.

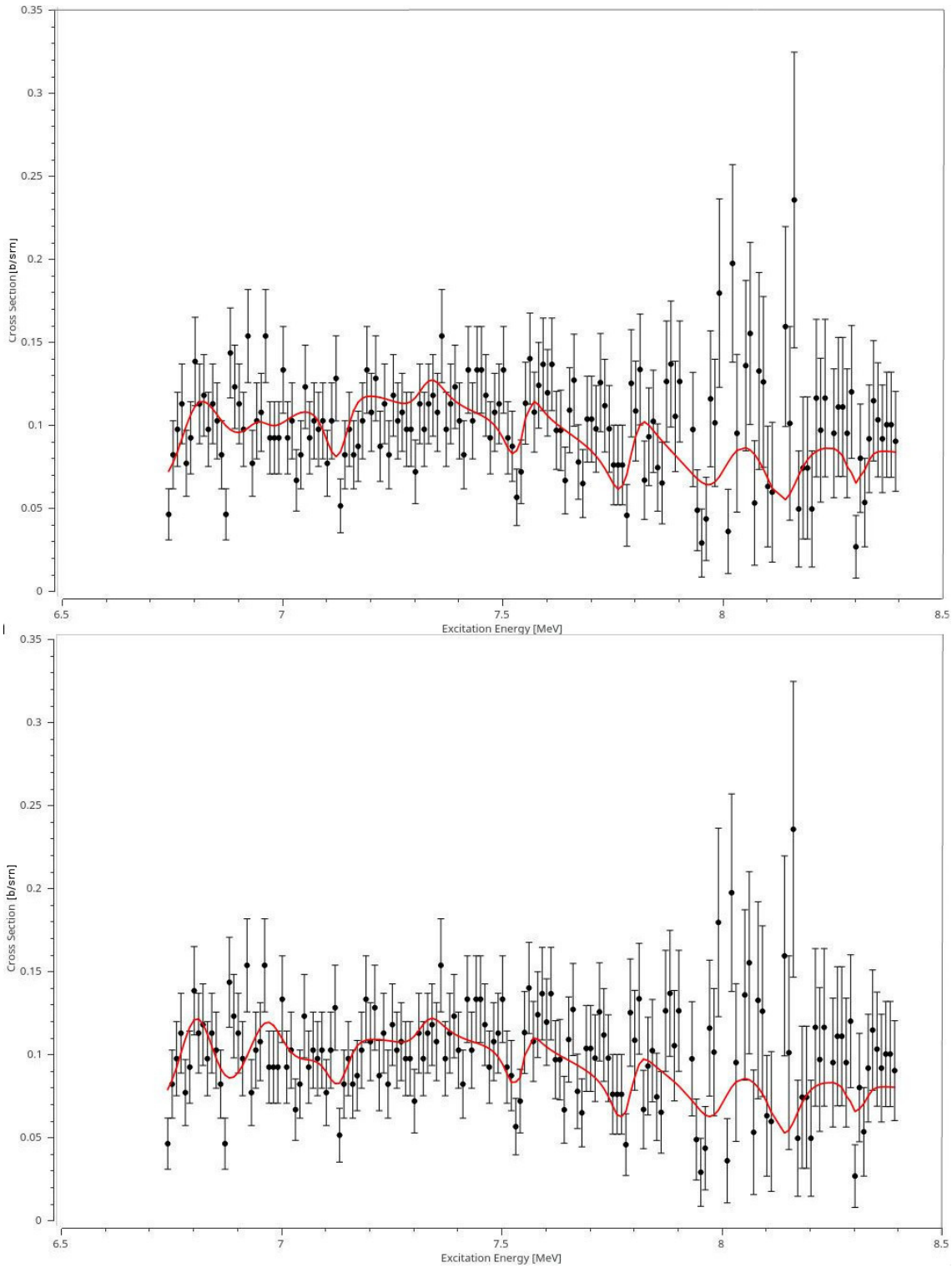

FIGURE 5.22. This plot shows the experimental cross section with the AZURE fit for the 0^+ (TOP) and the 2^+ (BOTTOM) spin assignments of the 6950-keV resonance. The curve in the above image is a better visual match to the data in the region of the resonance.

The resonance at 7480 keV has two best-fit spin assignments, both of which AZURE2 found to have partial widths above the 100-keV threshold. The spins of 0^+ and 2^+ have χ^2/N values of .9276 and .9031, respectively, and a χ^2 difference of 3.9. Since no resonance meets the χ^2 metric of 3, we next look to the partial widths. AZURE2 found the 0^+ spin to have a partial width of 147 keV, while the 2^+ was 263 keV. Thus it was then necessary to test the χ^2/N without the resonance entirely, giving a resulting χ^2/N=.9585. No clear conclusions can be drawn for this state, but given the aforementioned metrics, since this resonance was detected by Long *et al.*, it was assigned a spin of 0^+, and is included in the rate calculation. It should be mentioned that this is the state on the lower energy side of the 300-keV resonance gap in the results from Long *et al.*, which makes it complicated for the code to fit the local features of the resonance without resorting to a simple line.

The resonance at 7801 keV has two best-fit spin assignments, 2^+ with χ^2/N=.8978, and 1^-, with χ^2/N=.9141, and a total χ^2 difference of 2.24. Both partial widths found were well within the 100 keV threshold, with 1^- and 2^+ both at ~50 keV, so the value of 2^+ has been adopted for this work. However, the 1^- state should be considered similarly probable. As with the 7480-keV state, this resonance borders the 300-keV gap, this time on the higher energy end, so it faces similar complications as the 7480-keV resonance. As an additional note, without including these two bordering resonances it is difficult for the code to extrapolate the features inside the gap, and since the fit of a given resonance is inextricably tied to the closest neighboring resonances the effect of these two states is likely overestimated.

The resonance at 8020 keV has two best-fit spins, 2^+ with χ^2=.8978 and 1^- with χ^2=.9141, and a total χ^2 difference of 2.6. Both partial widths found by AZURE2 were above the 100 keV threshold, with 2^+ having a width of 141 keV, and 1^- having a width

of 111 keV. Despite this, the widths were not extreme enough to warrant testing of the fit without the resonance. The value of 2^+ has been adopted for this work.

The resonance at 8189 keV has 4 out of the 5 possible spin states meeting the χ^2/N criteria for best-fit, with the lowest, 2^+, at χ^2=.9422. However, the data in this region is from the cut regime described in Section 5.2, and has large uncertainties, thus further study is needed. Because this resonance was detected by Long *et al.*, it was included in the calculation and a value of 2^+ was adopted for this work.

5.8.3 New Levels

Using the method described in Section 5.7, four possible resonances were identified by AZURE2 by placing "floating" resonances of variable E_r every 1 MeV after fitting the initial baseline. These are in addition to those identified by Long *et al.* When analyzing the possible new resonances identified by the code, priority was given to non-natural parity states, as only natural parity states were possible in the ^{40}Ar$(p,t)^{38}$Ca reaction studied by Long *et al.* Also, the χ^2 difference metric of 3 was applied less strenuously.

A somewhat enigmatic possible resonance at 6911 keV was found, and further tests identified a non-natural parity spin assignment of 2^-, with χ^2=.9521. All other spins had a χ^2 difference > 100, the highest of any resonance. It should be noted that this state is less than 50 keV from one identified by Long *et al.* at 6950 keV. Additionally, the partial width of this possible resonance was found at >350 keV, well above to the 100-keV threshold. The final compounding factor is the fit without this resonance included. Fig. 5.23, has a χ^2/N of 1.9948, and from visual inspection, could be described as poor in the local region of E_r. A natural assumption might be that this resonance is identified by AZURE2 as a numerical artifact due to poor fitting on the neighboring resonance at 6950 keV, and the best-fit spin of 2^- in light of the natural parity assumptions make any conclusion uncertain. This state is not included in the final rate calculations.

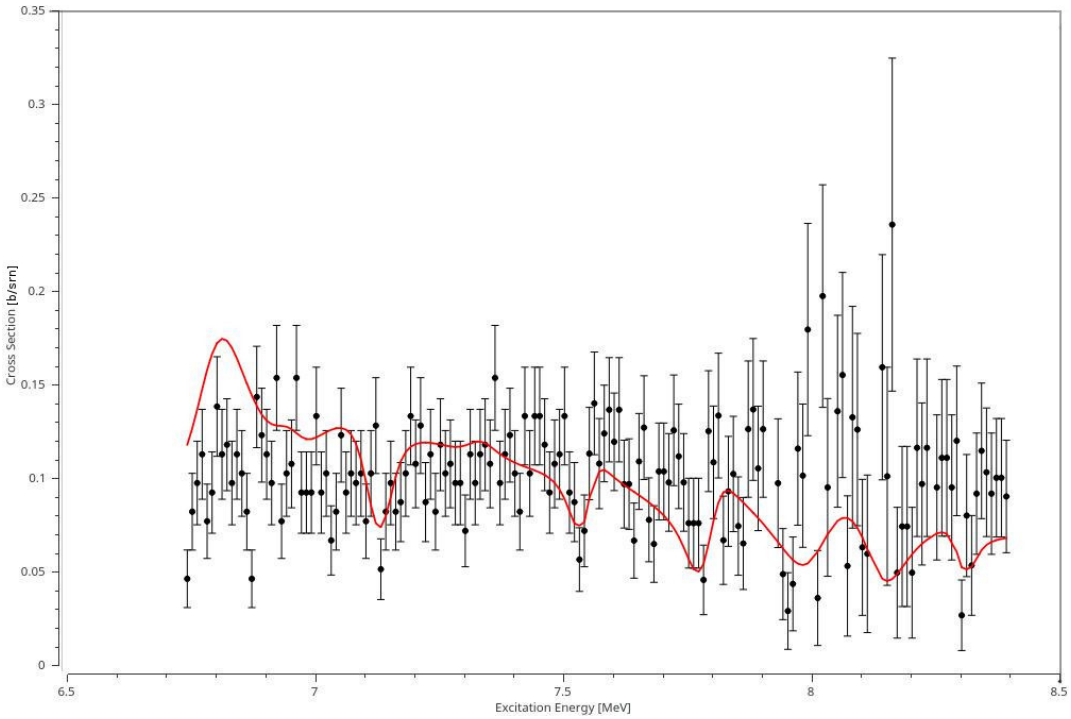

FIGURE 5.23. This plot shows the experimental cross section with the AZURE2 fit without including the possible resonance at 6911 keV. The visual match to the data in the region of the resonance is poorer than in the best-fit including this resonance.

A possible resonance at 7327 keV was identified, and testing all possible spins, those of both natural and unnatural parity, found that the 1^+ and 2^+ spins had nearly identical χ^2/N values, of .9298 and .9261, and a χ^2 difference of .58. Absent any restrictions on parity, this is to be expected as the contributions from these two different spins should be extremely similar. The partial width found for the 1^+ state was 48 keV, well within the threshold, and although the partial width of the 2^+ state is above it, at 104 keV it is only slightly and therefore cannot be ruled out entirely on this grounds. Also, the partial width metric is less significant in the new resonances not identified in Long *et al.*, however, a general consideration for partial width values still applies. An extremely large value would still imply the code is essentially removing the state from the fit. Due to the natural parity spin limitation, the 2^+ would otherwise be assumed if the resonance was to be included in the calculation, however, the fit without this resonance included had a χ^2/N of .9489, a difference between the best fit 2^+ state of ~3. The fit is not

significantly improved with the resonance added, and the question is raised again as to why a natural parity state was not detected by Long *et al.*, so this state was not included in the reaction rate, however, additional study is likely in order.

A possible resonance was identified at 7549 keV and as was the case with all the new resonances it is not limited to natural parity, so all spin assignments were tested. In fact it had 2 best-fit spins, that of 2^+, with χ^2/N=.9109, and 2^-, with χ^2/N=.9197 with a total χ^2 difference of only .41. However, AZURE2 found the 2^- state had a partial width of >700 keV, while the 2^+ spin assignment had a partial width of ~31 keV. For this reason the 2^- spin was ruled out. Though it should be investigated to conclude why this state was not found by the Long *et al.* work, it does correspond to a feature visible in the O'Brien *et al.* spectrum at ~ 7600 keV (see Fig. 3.5), as well as being in the 300 keV gap. Removing this resonance entirely gives a much poorer χ^2/N of 1.0183, with a χ^2 difference of ~ 15. Additionally, the plot of the fit by AZURE2 with this resonance removed seems to match the data poorly, especially in the local region of E_r, as seen in Fig. 5.24. This resonance was included in the calculation and a spin value of 2^+ was adopted for this work.

Finally, two additional possible resonances at 7693 keV and 8293 keV were identified by AZURE2. However, the possible resonance at 7693 keV had no clear spin value, as the difference between the lowest and highest χ^2, out of 8 possible spins, was ~ 17. Additionally, it did not have a significantly altered χ^2/N value when the resonance was removed entirely. The spin assignment with the best χ^2 was only ~3.9 less than that with the resonance removed. Because this was a new resonance, the combined analysis of these χ^2/N values were not convincing enough to include it in the final rate calculation. The 8293-keV resonance, which lies in the in the cut region with large uncertainties discussed in 5.2, was similarly ambiguous. Of the 8 possible spin assignments tested, the difference between the best and worst χ^2 was < 20, and a difference between the best

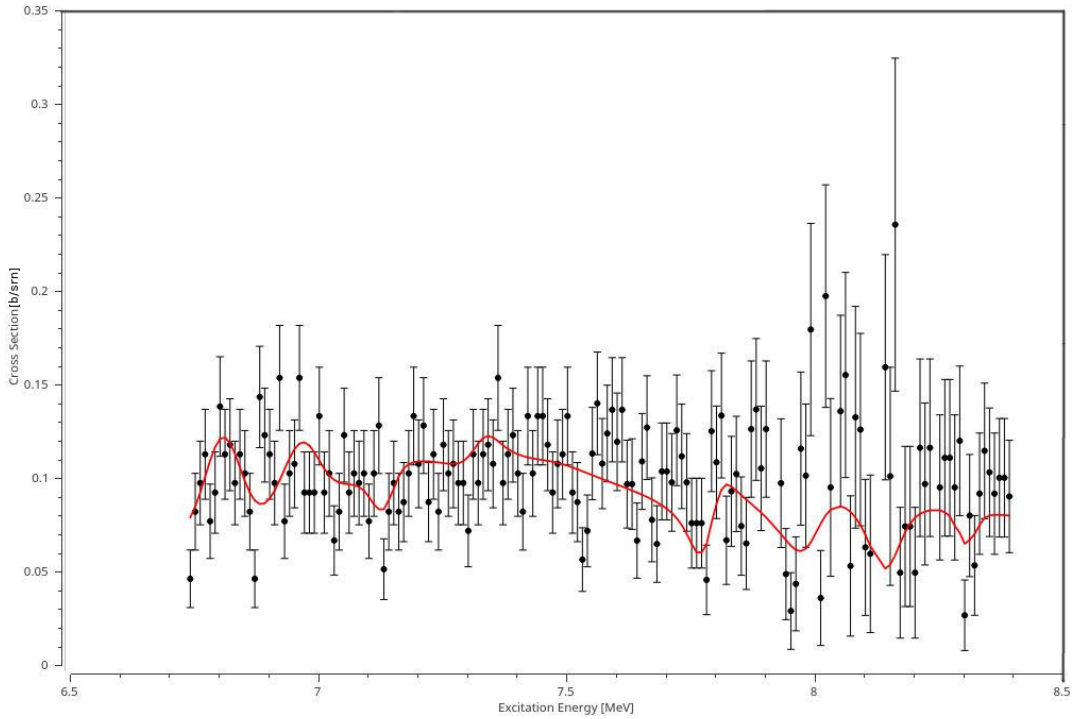

FIGURE 5.24. This plot shows the experimental cross section with the AZURE2 fit for the new possible resonance at 7549 keV removed. The fit is a poorer visual match to the data in the region of the resonance.

χ^2 and that with the resonance removed entirely was 7. As with the resonance at 7693 keV, the combined analysis of these χ^2 values were not convincing enough to include it in the reaction rate calculation considering it was not detected by Long *et al.* Neither of these possible resonances are included in the fit calculation.

5.9 Calculating the Reaction Rate

From the spin assignments found from the analysis of the experimental data (Table 5.1), and discussed in the previous section we are able to return to the formula for the reaction rate, Eq. 2.26.

$$N_A < \sigma\nu >_{01} = 1.54x10^{11}(\mu T_9)^{-3/2}\Sigma_i(2J_i + 1)\Gamma_{\alpha_i}e^{-11.605*E_{r_i}/T_9}. \tag{5.26}$$

and insert these values. We also follow the treatment of [53] and utilize the α single particle widths, multiplied by a spectroscopic factor of .01 to give the Γ_α values found in Table 5.1. As discussed in the AZURE2 fitting of the previous section, spin assignments,

TABLE 5.1. Resonance parameters used to calculate the ^{34}Ar$(\alpha, p)^{37}$K reaction rate. The new state determined in this work is denoted with a (*) and single particle widths are adopted from [53] and multiplied by a spectroscopic factor of 0.01 to obtain the listed Γ_α values below.

E_x (keV)	E_r (keV)	J^π	Γ_α (MeV)
6772	667	2^+	7.51×10^{-28}
6950	845	0^+	4.37×10^{-24}
7041	936	2^+	2.38×10^{-21}
7176	1071	2^+	2.11×10^{-19}
7480	1375	0^+	2.01×10^{-16}
7549*	1444	2^+	1.27×10^{-15}
7801	1696	2^+	1.11×10^{-13}
8020	1915	2^+	2.32×10^{-12}
8189	2084	2^+	1.54×10^{-11}
8322	2217	2^+	6.09×10^{-11}

as well as possible alternatives, were made for 10 previously identified resonances, along with a new possible resonance at 7549 keV and its associated spin. We use these values to calculate a baseline reaction rate and then plot the curves for the individual resonance contributions as well as their combined contributions. The results of these calculations are represented in the following figures: Fig. 5.25 plots the individual contributions from each resonance along with the total value, while Fig. 5.26 compares these results to the accepted rate from REACLIB (Fig. 3.3). The comparison shows a significant difference in the rate, as much as a factor of 100. Higher energy resonances are known to contribute more to the total rate, so it may be that the resonances outside the range of this experiment have the strongest contribution, so additional work to identify their true J^π value is in order. Also, it is theorized that the rate may be dominated by one or two α-cluster resonances that have not yet been distinguished from among the known resonances [28]. If this is correct and the α-cluster resonance is outside the energy range of this experiment, that would certainly explain this result. The possible alternative spin assignments will be used in additional calculations to put bounds on the rate. Figure 5.27 shows the ratio of the rate of this work to the REACLIB standard rate, along with the rates from the HF code Talys, and both the standard and α cluster rate found in [28] The average ratio of

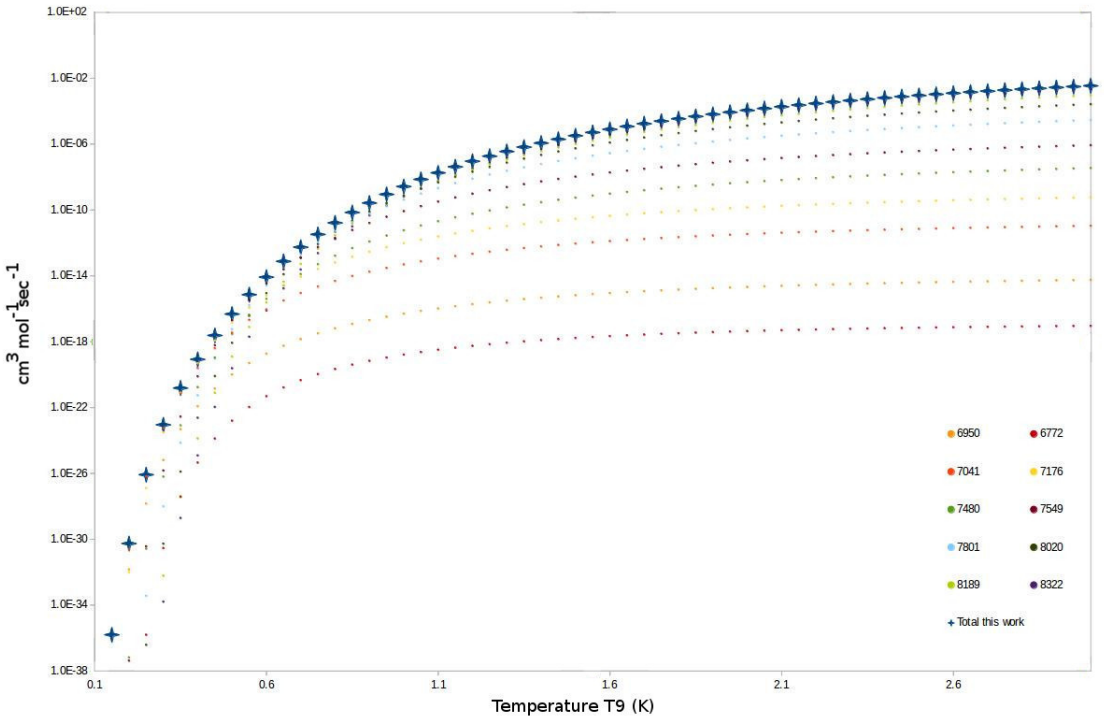

FIGURE 5.25. This plot shows the reaction rate contribution from the levels identified in this work, as well as the total contribution from the sum of all states.

the rate found in this work to the REACLIB rate is .0951. This value is used in stellar evolution models to measure the results on simulated XRB's and LMXB's.

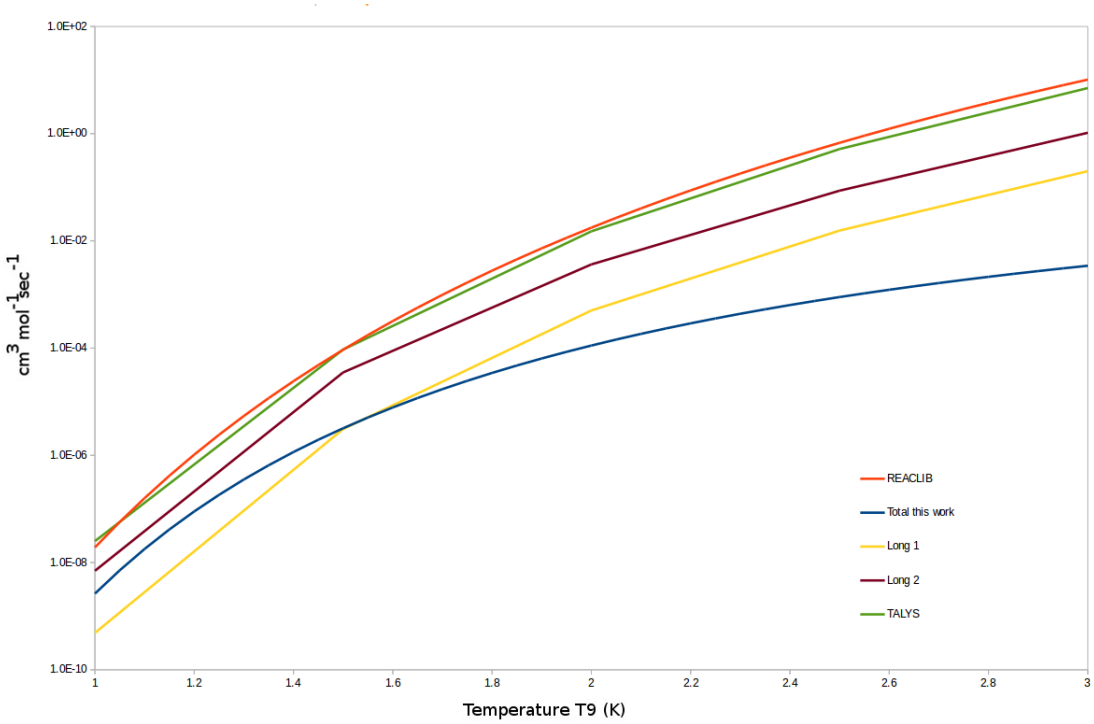

FIGURE 5.26. This plot shows the total reaction rate contribution from the sum of all states included in this work, compared to the currently accepted rate in REACLIB, along with rates from the HF code Talys, and both the standard and α cluster rate found in [28].

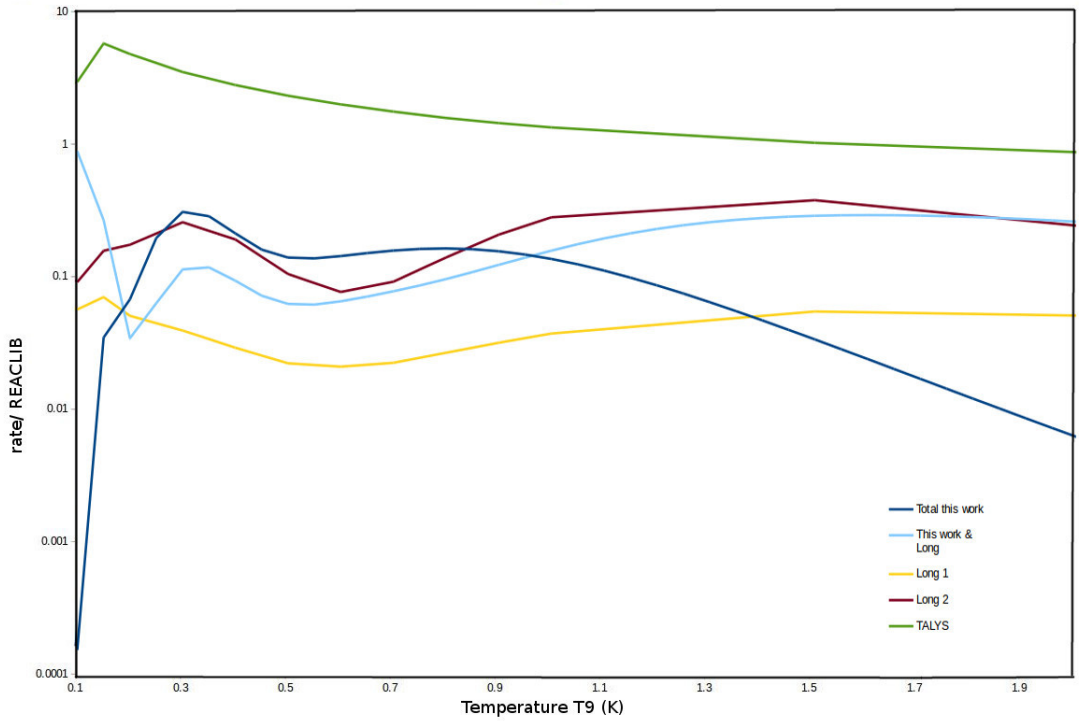

FIGURE 5.27. This plot shows the ratio to the REACLIB rate of the rates from this work, along with rates from the HF code Talys, and both the standard and α cluster rate found in [28]. The average ratio of the rate found in this work to the REACLIB rate is .0951.

Chapter 6
Models

The state of the art in stellar models depends upon which aspect of physics you choose to focus. The field has historically been limited to specialized codes that solve a few equations relevant to the work at hand. Hydrodynamics, general relativity, nuclear pasta, and many other subjects all have their own specialized code. Two notable exceptions to this are the stellar evolution codes KEPLER, which was used in Cyburt *et al.* [23], and Modules for Experiments in Stellar Astrophysics (MESA), which attempt to provide fully-coupled physics and a co-processed nuclear network. However, though these codes encompass the full classical physics of the stellar environment, they are limited to a single radial dimension. Due to the 1D nature, pulsations, rapid rotation, convection, spherical asymmetry features such as polar jets and accretion disks, and neutrino transport are all limited in their depiction. Due to computational limitations, such as processor speed, memory limits, and storage space, fully-coupled physics in 3 dimensions is still decades off. Extrapolating from the current largest simulation ever performed and the expectations of Moore's law, the current estimate is 50-60 years before computing power matches the needs of a fully coupled 3D simulation.

The goal of the computational portion of the project is to apply MESA to emulate the behavior of an accreting neutron star, with the accompanying burst behavior, alter the reaction rate of $^{34}\mathrm{Ar}(\alpha, p)^{37}\mathrm{K}$, and measure the impact on the light curve following the method of Cyburt *et al.* [9] and Eq. 3.1.

MESA is a collection of open source Fortran 95 components that together evolve more than 90 variables in over 10 coupled differential equations of stellar evolution over time and space, using matrix and linear algebra libraries. The resolution is variable, with

adaptive mesh in both time and space. It uses OpenMP to distribute processes among cores, with all variables written to be thread safe. The code has a stock library of standard physics, and provides output information in the form of time-evolved quantities such as temperature, opacity, elemental diffusion data, atmospheric boundary conditions, and a library of others. Specialized options for each of these variables can be invoked and varied at runtime. Additional variables, and custom physics can be applied by the user to the local model by altering a source file incorporated expressly for this purpose. These can either expand upon or replace the main routines without modifying the entire installation. Some options for applying custom physics involve user-defined mixing routines or custom neutrino behaviors. Appendix B provides further computational details such as an index of variables and equations calculated by the software [54][55].

The MESA code includes a nuclear reaction network, but as with the other methods that strictly rely on post-processing of nuclear networks for nucleosynthesis exploration, the default case is designed simply to include enough species to account for energy generation. This small network, usually ~8 species, is enough to match reported energy generation values to .1% (see Tables 4 and 5 in [54]). The MESA code recently added the capability for a fully-coupled, adaptive nuclear network, and though it cannot complete a comprehensive network calculation as yet, these expanded capabilities will allow a network that encompasses the $^{34}\mathrm{Ar}(\alpha, p)^{37}\mathrm{K}$ reaction, as well as those reactions important to the rp process. Full reaction networks can include a few thousand species and tens of thousands of calculations. This magnitude is still best suited to a dedicated post processing code, however, the expanded networks in MESA improve on the previous capabilities, and alleviate some of the limitations posed by lack of feedback between the physical quantities of the star and the nucleosynthesis. In any case, MESA can still provide the thermodynamic variables needed for a full post-processing network calculation.

6.1 XRB Models

As was previously discussed, the ^{34}Ar(α, p)^{37}K reaction is found to be important to the light curve of an XRB, in the work by Cyburt *et al.*, Parikh *et al.*, and Fisker *et al.* However, due to limitations discussed previously in Ch. 3, these models have shortcomings which limit their applicability. This work uses the stellar XRB model adapted from one provided by the MESA development group and Rob Farmer [55], to test the effect of the new reaction rate found in this work. We will compare this to the results of Parikh, Cyburt, and Fisker, and the results will be a commentary not only on the importance of the rate, but on the applicability of their models.

Farmer's model from Paxton *et al.* [55] was written as a demonstration of MESA's new co-processing capabilities. The model is still limited to 1D so burning is considered uniform over the surface of the star. The accretion rate is also constant. It is modeled after several years worth of RXTE burst observations [16] of GS 1826-24, which showed burst recurrence variation from 4.1 to 3.56 hrs, in a period of 2 years, but the light curve shape remained consistent. Accretion is set at 3.0x10^{-9} $M_\odot$ yr^{-1}, and the accreted and burning material is assumed to be 70.5% ^{1}H, 27.5% ^{4}He, and 2% metallicity. Even though these quantities are intended to closely approximate GS 1826-24, the burst recurrence time of the model, which is strongly dependent on accretion rate, is 1 hr less than that of the actual system. A reduced accretion to 2.4x10^{-9} $M_\odot$ yr^{-1} does improve the matching of recurrence time, but the light curve becomes less faithful to the one actually observed. The envelope base luminosity is set to 1.6x10^{34} ergs/s.

Material mixing due to rotation is included for both physical accuracy and computational convergance. Gravity in each cell is corrected for GR effects, but since the EOS is still not known, and there may be additional difficulties to modeling it once it is discovered, the model has an inner boundary inside of which the physical quantities of stellar evolution (discussed in Appendix A) are set constant and are not evolved along with

the envelope. A core mass of 1.4 $M_\odot$ and 11.2 km is surrounded by the modeled zones, with an inert layer in the interior of the envelope that does not burn. All of the physical quantities are easily varied should the parameter space be examined further in future explorations.

In the work by Paxton *et al.* [55], variations of the nuclear network were tested with three networks containing 53, 153, and 305 species, as well as the adaptive network. Figure 6.1 shows a relatively good match of the light curves to the GS 1826-24 for all except the 53-species model. This network is missing many of the component species for the (α, p) waiting point reactions. More specifically it does not contain any isotopes of Ar, K, or Ca and so it does not reflect the impact of $^{34}\mathrm{Ar}(\alpha, p)^{37}\mathrm{K}$. While the difference in light curves is far from conclusive evidence of the impact of $^{34}\mathrm{Ar}(\alpha, p)^{37}\mathrm{K}$, the convergence of curves with increasing net size, which is known to be more physical and has been discussed as having an important impact on model results, makes a strong case for an extended exploration in co-processing nucleosynthesis and stellar evolution.

A 153 species network named rp_153.net is to be used in this work, with isotopes up to $^{56}\mathrm{Ni}$, so named for its emphasis on the proton-rich isotopes common in the (r, p) process. This network was taken from [56], and includes all the charged-particle reactions connecting the incorporated species, as well as β decay and some neutron reactions. As well as including all the component isotopes in the $^{34}\mathrm{Ar}(\alpha, p)^{37}\mathrm{K}$ reaction, this net includes all the species necessary to study the full list of (α, p) waiting-point reactions.

6.2 Model Results

A model using the standard REACLIB $^{34}\mathrm{Ar}(\alpha, p)^{37}\mathrm{K}$ reaction rate was run to use as a baseline for comparison of the results of the model with the rate found in this work. This rate was then replaced by a rate which modifies the REACLIB rate by the .0951 factor found in this work. The metric of interest is the luminosity calculation in Eq. 3.1, as well as any additional variation in the output variables. Additional parameter space

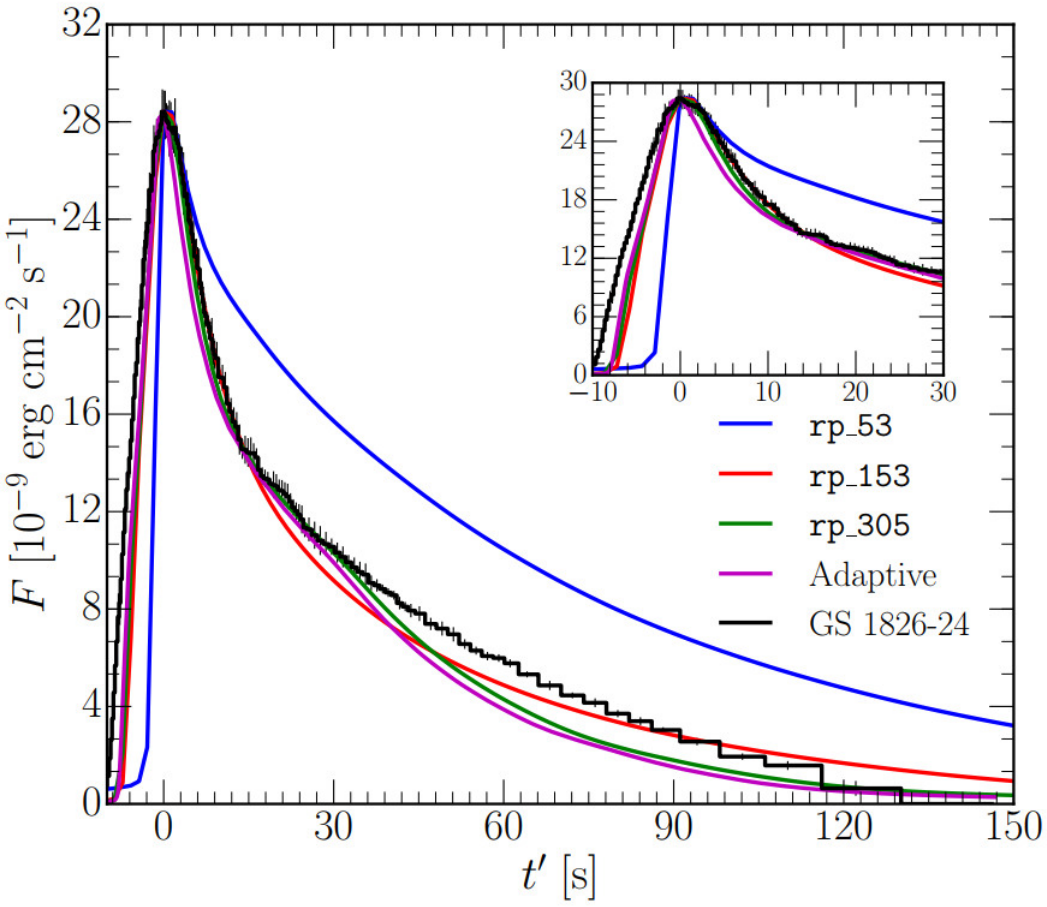

FIGURE 6.1. The figure gives the light curves for different networks resulting from the XRB model from [55], with flux vs folded time. In order to display multiple burst profiles on the same plot, the results are "folded", where time is in measured as a relative value (t') and not fixed, and the light curves are aligned such that the peak luminosity (F) occur at the same value of t'. The different networks are denoted by color

exploration is possible, by varying the luminosity, accretion, radius, mass, and any other physical quantities that can be user specified in MESA (Appendix B).

Figure 6.2 was produced using a simplified baseline calculation by the author using a custom built server in the LSU laboratory. The preliminary results show two immediately apparent effects. First, the burst light curve does not appear to be impacted by the rate factor found in this work and applied to the $^{34}\mathrm{Ar}(\alpha, p)^{37}\mathrm{K}$ reaction rate. Comparing Fig. 6.2 and the curve in Fig. 6.3, where the only variation between the models that produced these two burst light curves is the change in reaction rate, we see that the magnitude of the curve produced by the new rate appears identical. Second, and most interesting, is the burst recurrence time. Figures 6.4 and 6.5 show some of the standard output plots of MESA, displaying several quantities of interest in a convenient format. The lower left quadrant of this output grid shows the luminosity of the star, with the repeated peaks corresponding to the XRB peaks. Visual inspection of the time scale from the start of the first observed burst in Fig. 6.4 and 6.5, produced using the standard REACLIB rate and the new rate factor, respectively, to the last observed burst in both cases shows that the new rate factor decreases average burst recurrance time from 1.81 hrs to 1.76 hrs. This is compared to an observed value of the Clocked burster of 3.6-4.1 hours.

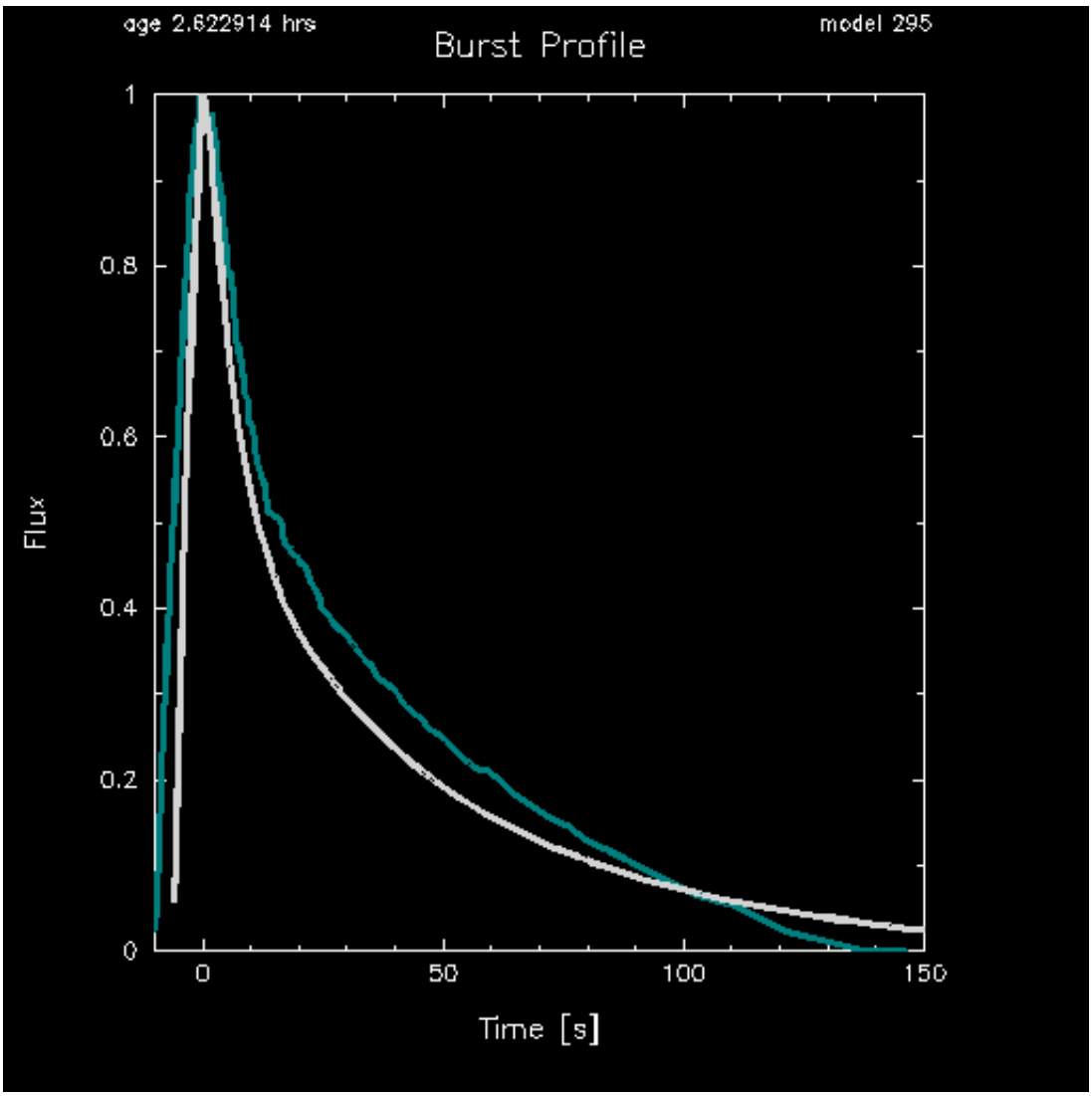

FIGURE 6.2. This figure shows the baseline XRB light curve produced using the standard REACLIB rate for $^{34}\mathrm{Ar}(\alpha, p)^{37}K$ and a 153-species network designed to emphasis rp process reactions, and modelled with stellar modelling software MESA. The white curve is the burst produced by the model, while the green curve is the observational data from the Clocked Burster. Visual match to the observation is good.

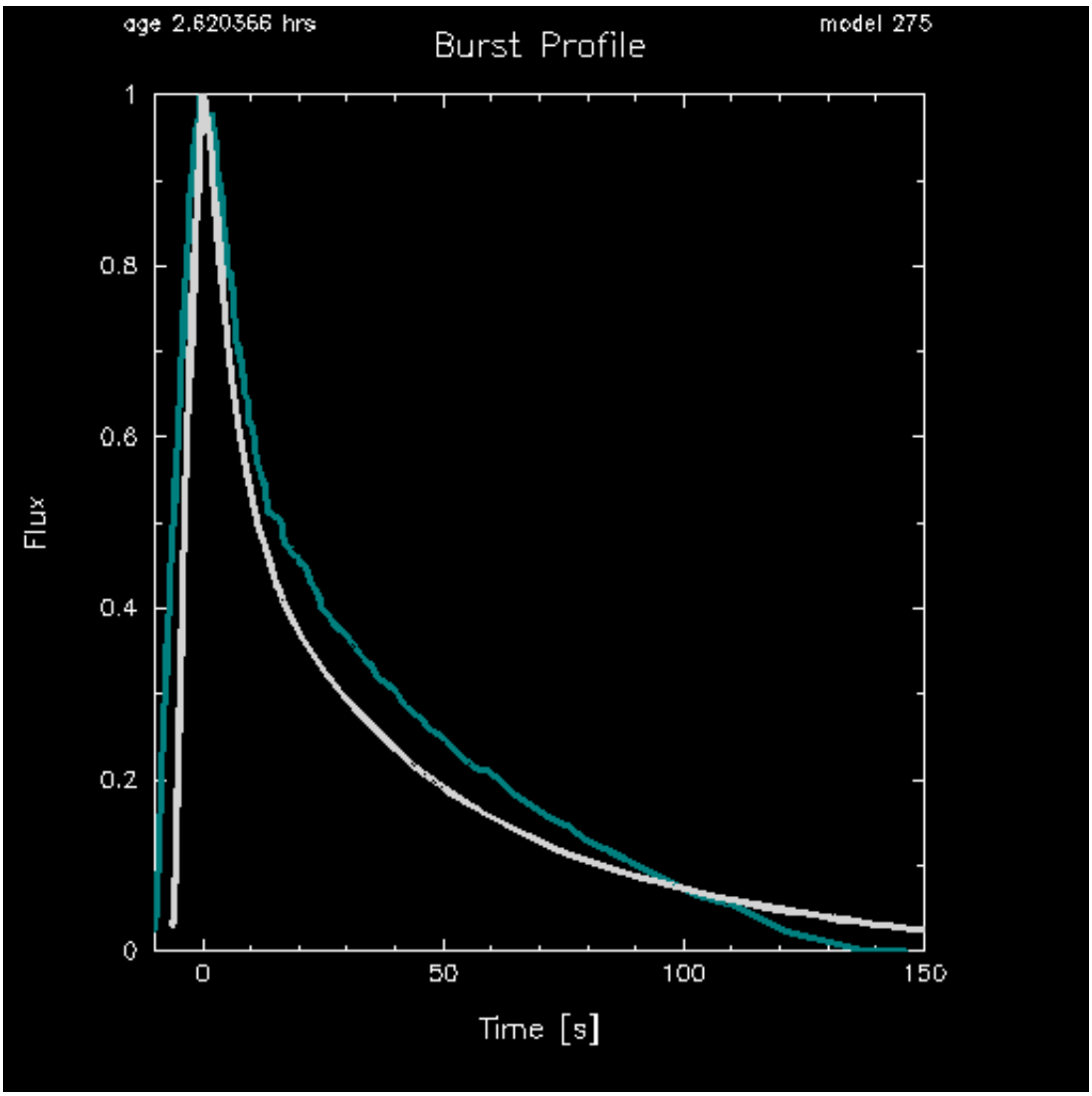

FIGURE 6.3. This figure shows the XRB light curve produced using the standard REACLIB rate for ^{34}Ar(α, p)^{37}K multiplied by the factor of .0951 found in this work, and a 153-species network designed to emphasis rp process reactions, and modelled with stellar modelling software MESA. The white curve is the burst produced by the model, while the green curve is the observational data from the Clocked Burster. Visual match to the observation is similar to Fig. 6.2.

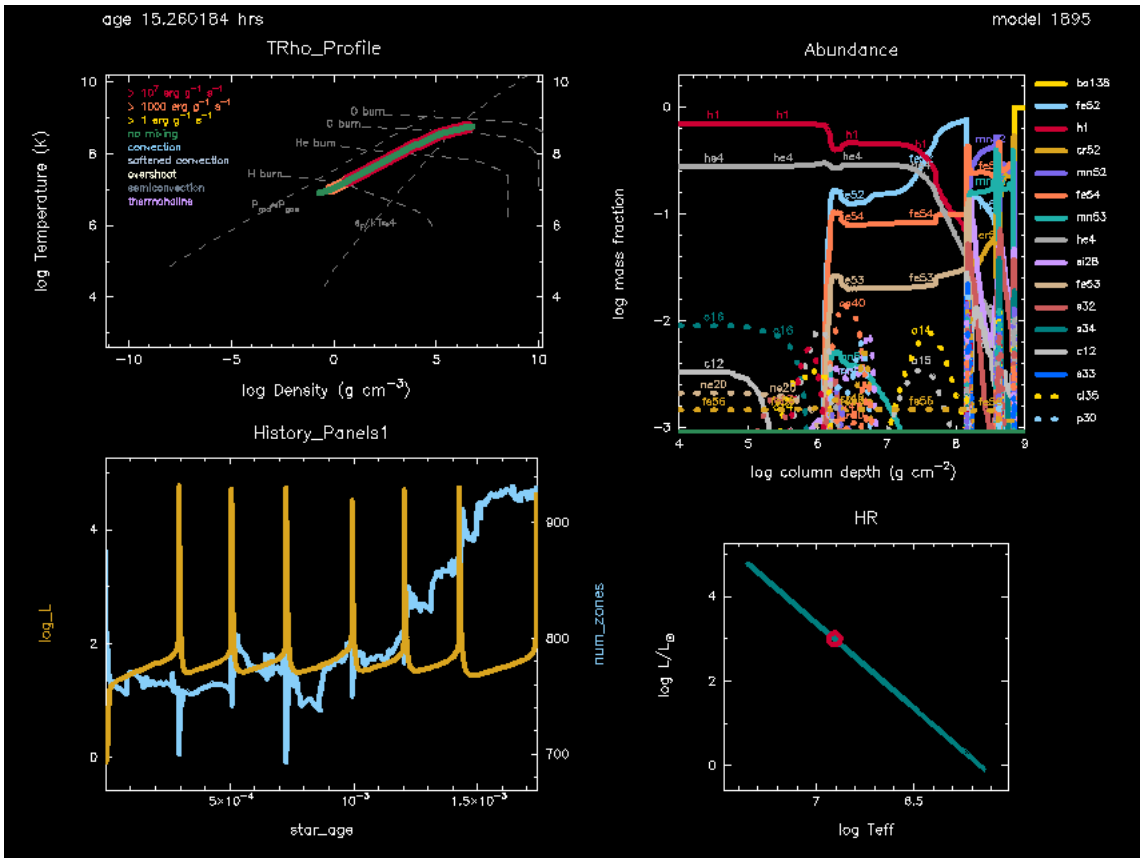

FIGURE 6.4. This figure shows a grid of standard value output by MESA produced using the standard REACLIB rate for ^{34}Ar$(\alpha, p)^{37}$K and a 153-species network designed to emphasis rp process reactions. The lower left hand plot shows luminosity vs time, with the peaks corresponding to XRB light curve peaks. Burst recurrence time for this model is 1.81 hrs.

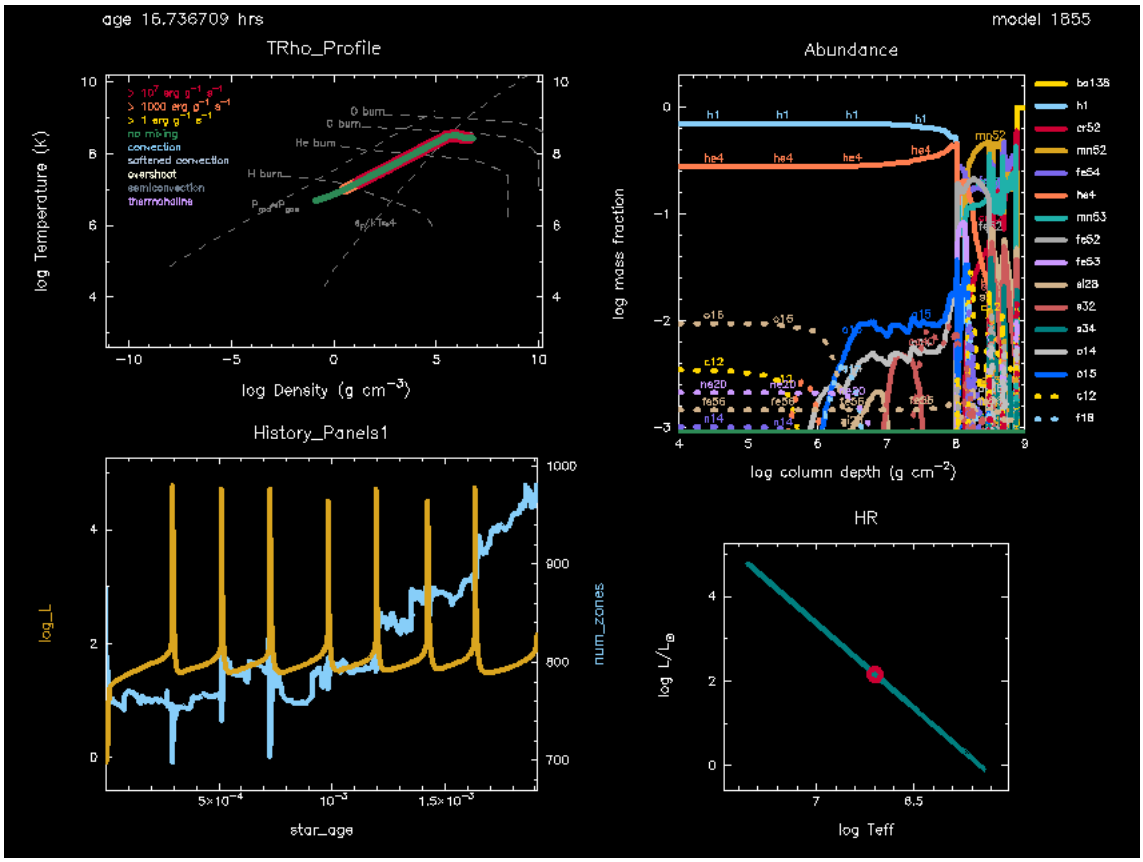

FIGURE 6.5. This figure shows a grid of standard value output by MESA produced using the standard REACLIB rate for ^{34}Ar$(\alpha, p)^{37}$K modified by a factor of .0951, and a 153-species network designed to emphasis rp process reactions. The lower left hand plot shows luminosity vs time, with the peaks corresponding to XRB light curve peaks. Burst recurrence time for this model is 1.76 hrs.

Chapter 7
Results and Discussion

The ^{34}Ar(α, p)^{37}K reaction has important implications for XRB nucleosynthesis and the resulting light curves. Barriers exist to studying it directly, and so this work studied proton scattering on ^{37}K to explore the compound nucleus ^{38}Ca. This was done to examine properties of resonances above the α threshold in the range of energies corresponding to theorized XRB temperatures. This scattering study reveals information that allows us to determine the important quantities in the reaction rate, (Eq. 2.24). Due to the relative values of proton partial width and total resonance width, whose ratio $\approx$1, the generalized rate equation, (Eq. 2.8) reduces to Eq. 2.26. Thus the only necessary quantities are the resonance energies E_r, their spin assignments J^π, and the α partial widths Γ_α, though it is possible from the experimental data to calculate the values of the partial widths (Γ_p) and total resonance widths (Γ_T), and this information can still be utilized in other calculations. The experimental results presented here were analyzed following the methods in Ch. 5 to give an excitation function in the lab frame, which was input into the R-Matrix software AZURE2 to find best fit spins for the levels taken from Long *et al.* [28], as well as 4 additional levels identified in the R-Matrix analysis. These spins were combined with the corresponding values for E_r identified in [28], and Γ_α, determined from [53], and using Eq. 2.25, a reaction rate contribution for the levels examined in this work was calculated (Fig. 5.26). An additional calculation was done using resonances outside the experimental energies of this study that were identified in Long *et al.*, with spin assignments set to 1^- as this was the most probable spin as calculated by Long *et al.* in order to identify an upper bound on the rate, which is shown in Fig. 7.1. The results show that the combined rate calculated with resonances and spin assignments identified

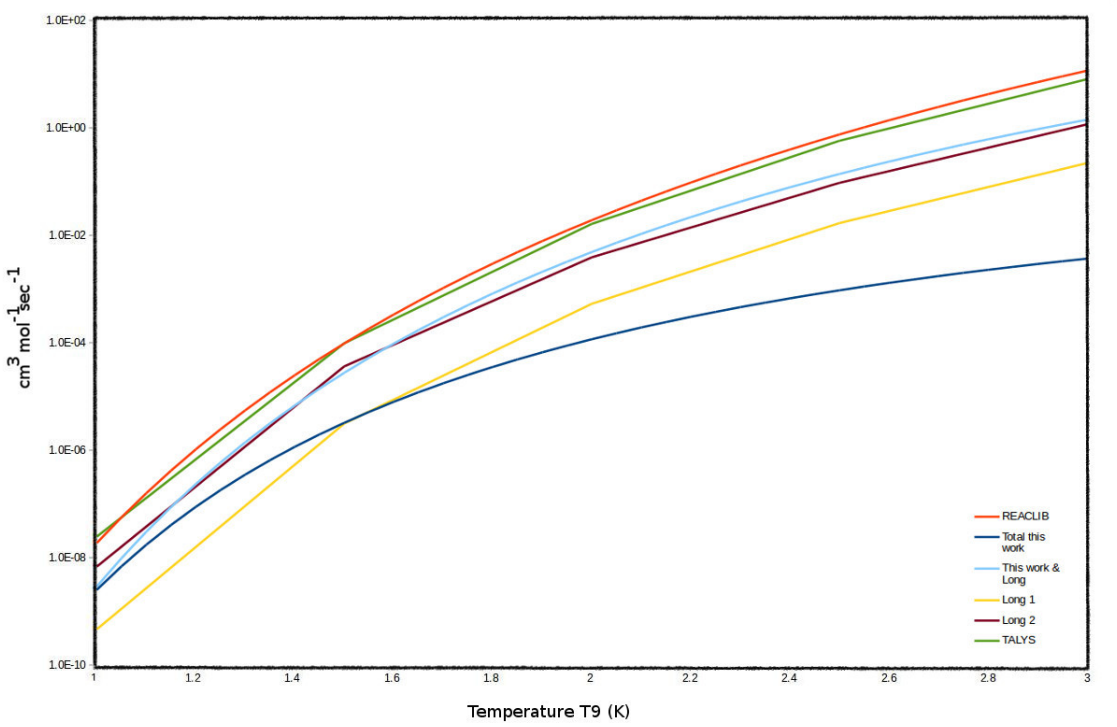

FIGURE 7.1. This plot shows the reaction rate found in this work as well as a rate calculated using all additional resonance states from Long *et al.*. Other rates shown are the standard rate from REACLIB, along with rates from the HF code Talys, and both the standard and α cluster rate found in [28]

in this work as well as the resonances outside the experimental energy range of this work from Long *et al.* varies from both the standard and α cluster rate calculated in that work. This is likely caused by differences in the method of choosing spins, as Long *et al.* use a Monte Carlo approach instead of choosing a single spin value as done here. Since both spin and the resulting α partial width appear in the reaction rate equation, any difference is compounded. The rate factor shown in Fig. 5.27 was then implemented using an XRB stellar model developed in MESA, and the resulting XRB observables were examined. Full analysis of the model results is in progress, but preliminary results show that the rate of ^{34}Ar(α, p)^{37}K affects the burst recurrence time and possibly the magnitude of the light curve.

7.1 Future Work

There are several open questions related to this work that need to be addressed. The excitation energy range observed in this work presently does not match the calculated range derived from the reported beam energy. We have restricted the source of this discrepancy to an incorrect reported beam energy or an incorrect calculation in the calibration. As discussed in Ch. 5, we are in search of additional confirmation of the applied calibration via study of the ^{40}Ar+p scattering. Also, the ^{37}K+^{12}C fusion evaporation protons that are known to punch through the final layer of the Si detector telescopes can be used to compare their maximum energy with known values. In addition, the staff at the NSCL is reviewing the logs to determine if the reported beam energy is accurate This is still under investigation.

The cut region currently considered suspect suffers from outsized uncertainty compared to the other cross section data energy ranges due to lower statistics. It is possible this might be corrected by combining information from the two different data regimes, the QQQ3 and QQQ5 detectors to synthesize a more complete data set from a combination of the two.

The uncertain spins, while they present a complication in calculating a definitive reaction rate, can provide bounds on the rate calculated in the best fit, as the rate can be recalculated using all the likely spin assignments.

The XRB models run with the new rate will need to be analyzed to provide the necessary comparison with previously published models. Even though the many rapid advancements of stellar modelling have provided new developments such as co-processed networks, it may be that the limitations that remain prevent us from uncovering the true nature of the interplay between the reactions and the light curve, and we may still find ourselves unsure of the cause of double-peaked bursts despite our best efforts. Also, the XRB models are the first step in an important contribution the author hopes to make to

the field. The standard for sensitivity studies has been stellar models completed with a small network and full network calculations in a post-processing code. The most recent XRB sensitivity study discussed in this work, that of Cyburt *et al.*, is a notable exception, as it was completed using the more comprehensive stellar evolution code KEPLER, which is able to calculate a large co-processed network. However, KEPLER is closed-source, and closed-access. MESA, with its open-source, open-access model, not only has the benefit of a wider audience of developers and therefore a more rapid and intensive release model, but it also will allow any experimentalist to train in its use and apply it to any of the existing stellar models and nuclear reactions, and even develop cutting-edge, novel new models. The author intends to continue extensive work and adaptation of the existing XRB model and complete the first published sensitivity study on XRB's using MESA.

The direct experiment always looms large in the experimentalist's future outlook, as it is the ultimate goal and represents the best hope for a comprehensive rate. Several new developments may facilitate this: the Facility for Radioactive Ion Beams (FRIB) is the next generation accelerator facility in the United States that is currently under construction at Michigan State University. FRIB will be operational in 2022 and provide radioactive ion beams with higher intensities than currently available allowing direct measurements of many reactions of astrophysical interest for the first time, potentially including the ^{34}Ar(α, p)^{37}K reaction.

The nuclear astrophysics group at LSU has several new projects in progress for their nuclear-astrophysical experimental program, which will also open new opportunties for study of radioactive-ion-beam reactions. The Array for Nuclear Astrophysics and Structure with Exotic Nuclei (ANASEN) is an active target, i.e. the target gas also acts as the detector medium, designed for this purpose and developed by the LSU-FSU (Florida State University) collaboration. Extended gas targets can be used to measure the exci-

tation function over a range of energies concurrently with a single incident ion beam energy. ANASEN consists of a cylindrical proportional counter (PC) that surrounds the beam axis and Si detectors arranged in a barrel configuration around the PC. To perform a direct measurement of the excitation function of the ^{34}Ar$(\alpha, p)^{37}$K reaction, a beam of ^{34}Ar would proceed through the ANASEN chamber and protons produced via (α, p) reactions occurring along the beam path would yield position and energy measurements in both the PC and Si detectors, allowing event-by-event reconstruction of the kinematics. ANASEN has already been successfully used for multiple direct (α, p) measurements and a ^{34}Ar$(\alpha, p)^{37}$K study is planned once an ^{34}Ar beam of sufficient intensity ($\geq 10^5$ pps) can be achieved. Also, the LSU group is presently installing an Enge split-pole spectrometer at FSU. This will allow transfer reaction studies, similar to the one described in Long *et al.*, to be performed to determine additional information on the excited states in ^{38}Ca corresponding to ^{34}Ar+α resonances. For example, the ^{40}Ca$(p, t)^{38}$Ca study could be measured at a series of angles to determine the angular distributions of states in ^{38}Ca and determine their J^π values for comparison the assignments made in this work.

From the new rate information provided by this work, future experiments, stellar models, and theoretical calculations will be better informed and better constrained, until such time as the forward reaction can be studied with sufficiently high statistics in the astrophysically relevant regime to allow for more definitive conclusions. Though we make strides toward settling the relevant questions in XRB nucleosynthesis, such as how this reaction affects light curves, final abundances, and whether it could be responsible for the double peaked burst, much more work is left to put these questions to rest.

Bibliography

[1] A. G. W. Cameron. Abundances of the elements in the solar system. *Space Sci Rev*, 15(1):121–146, September 1973. doi: 10.1007/BF00172440.

[2] J. Grindlay, H. Gursky, H. Schnopper, D. R. Parsignault, J. Heise, A. C. Brinkman, and J. Schrijver. Discovery of intense X-ray bursts from the globular cluster NGC 6624. *The Astrophysical Journal Letters*, 205:L127–L130, May 1976. doi: 10.1086/182105.

[3] R. D. Belian, J. P. Conner, and W. D. Evans. The discovery of X-ray bursts from a region in the constellation Norma. *The Astrophysical Journal Letters*, 206:L135–L138, June 1976. doi: 10.1086/182151.

[4] Q. Z. Liu, J. van Paradijs, and E. P. J. van den Heuvel. A catalogue of low-mass X-ray binaries in the Galaxy, LMC, and SMC (Fourth edition). *Astronomy and Astrophysics*, 469:807–810, July 2007. doi: 10.1051/0004-6361:20077303.

[5] H. Ritter and U. Kolb. Catalogue of cataclysmic binaries, low-mass X-ray binaries and related objects (Seventh edition). *Astronomy and Astrophysics*, 404:301–303, June 2003. doi: 10.1051/0004-6361:20030330.

[6] H. Schatz, A. Aprahamian, V. Barnard, L. Bildsten, A. Cumming, M. Ouellette, T. Rauscher, F.-K. Thielemann, and M. Wiescher. End Point of the rp Process on Accreting Neutron Stars. *Phys. Rev. Lett.*, 86(16):3471–3474, April 2001. doi: 10.1103/PhysRevLett.86.3471.

[7] Anuj Parikh, Jordi Jose, Fermin Moreno, and Christian Iliadis. The Effects of Variations in Nuclear Processes on Type I X-Ray Burst Nucleosynthesis. *The Astrophysical Journal Supplement Series*, 178(1):110–136, September 2008. doi: 10.1086/589879.

[8] Jacob Lund Fisker, Friedrich-Karl Thielemann, and Michael Wiescher. The Nuclear Reaction Waiting Points: 22Mg, 26Si, 30S, and 34Ar and Bolometrically Double-peaked Type I X-Ray Bursts. *ApJ*, 608(1):L61, June 2004. doi: 10.1086/422215.

[9] R. H. Cyburt, A. M. Amthor, A. Heger, E. Johnson, L. Keek, Z. Meisel, H. Schatz, and K. Smith. Dependence of X-Ray Burst Models on Nuclear Reaction Rates. *The Astrophysical Journal*, 830(2):55, October 2016. doi: 10.3847/0004-637X/830/2/55.

[10] Andrew W. Steiner, James M. Lattimer, and Edward F. Brown. The Neutron Star Mass-Radius Relation and the Equation of State of Dense Matter. *ApJL*, 765(1): L5, 2013. doi: 10.1088/2041-8205/765/1/L5.

[11] Christian Iliadis. *Nuclear Physics of Stars*. Wiley-VCH, Weinheim, 1 edition edition, April 2007.

[12] Carl J. Hansen, Steven D. Kawaler, and Virginia Trimble. *Stellar Interiors: Physical Principles, Structure, and Evolution*. Springer, 2004.

[13] I. Bombaci. The maximum mass of a neutron star. *Astronomy and Astrophysics*, 305:871, January 1996.

[14] Amanda I. Karakas and John C. Lattanzio. The Dawes Review 2: Nucleosynthesis and stellar yields of low and intermediate-mass single stars. *arXiv:1405.0062 [astro-ph]*, April 2014.

[15] Juhan Frank, Andrew King, and Derek Raine. *Accretion Power in Astrophysics*. Cambridge University Press, Cambridge, UK ; New York, 3 edition edition, February 2002.

[16] Duncan K. Galloway, Michael P. Muno, Jacob M. Hartman, Dimitrios Psaltis, and Deepto Chakrabarty. Thermonuclear (type-I) X-ray bursts observed by the Rossi X-ray Timing Explorer. *The Astrophysical Journal Supplement Series*, 179(2): 360–422, December 2008. doi: 10.1086/592044.

[17] H. Schatz and K. E. Rehm. X-ray binaries. *Nuclear Physics A*, 777:601–622, October 2006. doi: 10.1016/j.nuclphysa.2005.05.200.

[18] M. Wiescher, J. Görres, and H. Schatz. Break-out reactions from the CNO cycles. *J. Phys. G: Nucl. Part. Phys.*, 25(6):R133, June 1999. doi: 10.1088/0954-3899/25/6/201.

[19] Anna L. Watts. Thermonuclear burst oscillations. *arXiv:1203.2065 [astro-ph]*, March 2012. Annual Review of Astronomy and Astrophysics 2012, vol. 50, p.609-640.

[20] C. J. Hansen and H. M. van Horn. Steady-state nuclear fusion in accreting neutron-star envelopes. *The Astrophysical Journal*, 195:735–741, February 1975. doi: 10.1086/153375.

[21] Anna L. Watts and Immanuel Maurer. Accretion rate and the occurrence of multi-peaked X-ray bursts. *Astronomy & Astrophysics*, 467(2):L33–L36, May 2007. doi: 10.1051/0004-6361:20077326.

[22] Osamu Koike, Masa-aki Hashimoto, Reiko Kuromizu, and Shin-ichirou Fujimoto. Final Products of the rp-Process on Accreting Neutron Stars. *ApJ*, 603(1):242, 2004. doi: 10.1086/381354.

[23] Richard H. Cyburt, A. Matthew Amthor, Ryan Ferguson, Zach Meisel, Karl Smith, Scott Warren, Alexander Heger, R. D. Hoffman, Thomas Rauscher, Alexander Sakharuk, Hendrik Schatz, F. K. Thielemann, and Michael Wiescher. The JINA REACLIB Database: Its Recent Updates and Impact on Type-I X-ray Bursts. *ApJS*, 189(1):240, 2010. doi: 10.1088/0067-0049/189/1/240.

[24] T. Rauscher and F.-K. Thielemann. Astrophysical Reaction Rates From Statistical Model Calculations. *Atomic Data and Nuclear Data Tables*, 75(1-2):1–351, May 2000. doi: 10.1006/adnd.2000.0834.

[25] T Rauscher. NON-SMOKER Hauser Feshbach rates with Audi Wapastra masses., 1999.

[26] J Blackmon, C Macon, C. M Deibel, C Rasco, D Santiago-Gonzalez, A Lauer, J Lai, L Afanasieva, I Wiedenhoever, L Baby, G Rogachev, E Koshchiy, H Schatz, F Montes, F Kontos, T Ahn, and M Avila. Study of the 38ca through 37k+p scattering to improve the 34ar(alpha,p)37k reaction rate. NSCL PAC proposal 14059, 2014.

[27] S. O'Brien, G. P. A. Berg, M. Couder, J. Goerres, D. Patel, K. Sault, M. Wiescher, T. Adachi, K. Hatanaka, D. Ishikawa, H. Matsubara, H. Okamura, H. J. Ong, T. Suzuki, A. Tamii, J. Zenihiro, M. Dozono, T. Wakasa, H. [Research Center for Nuclear Physics Fujita, University of Witwatersrand School of Physics, and Y. (and others)Fujita. Exploring the {alpha}p-Process with Grand Raiden. *AIP Conference Proceedings*, 1090(1), January 2009. doi: 10.1063/1.3087029.

[28] A. M. Long, T. Adachi, M. Beard, G. P. A. Berg, Z. Buthelezi, J. Carter, M. Couder, R. J. deBoer, R. W. Fearick, S. V. Förtsch, J. Görres, J. P. Mira, S. H. T. Murray, R. Neveling, P. Papka, F. D. Smit, E. Sideras-Haddad, J. A. Swartz, R. Talwar, I. T. Usman, M. Wiescher, J. J. Van Zyl, and A. Volya. Indirect study of the stellar 34Ar(alpha,p)37K reaction rate through 40Ca(p,t)38Ca reaction measurements. *Phys. Rev. C*, 95(5):055803, May 2017. doi: 10.1103/PhysRevC.95.055803.

[29] R. A. Paddock. (p,t) Reaction on Even-Even $N=Z$ Nuclei in the $2s1d$ Shell. *Phys. Rev. C*, 5(2):485–500, February 1972. doi: 10.1103/PhysRevC.5.485.

[30] S. Kubono, S. Kato, M. Yasue, H. Ohnuma, M. Sasao, K. Tsukamoto, and R. Kuramasu. The 40Ca(p, t)38Ca reaction and configuration mixing. *Nuclear Physics*

A, 276(2):201–220, January 1977. doi: 10.1016/0375-9474(77)90379-7.

[31] W. P. Alford, P. Craig, D. A. Lind, R. S. Raymond, J. Ullman, C. D. Zafiratos, and B. H. Wildenthal. Structure of 22Mg, 26Si, 34Ar and 38Ca via the (3He, n) reaction. *Nuclear Physics A*, 457(2):317–336, September 1986. doi: 10.1016/0375-9474(86)90381-7.

[32] C. M Deibel, L. Afanasieva, J. Lai, B. C. Rasco, M Albers, M. Alcorta, S Almaraz-Calderon, P. F. Bertone, J Chen, J. A. Clark, J. P. Greene, C. R. Hoffman, C. L. Jiang, B. P. Kay, H. Y. Lee, C Nair, T Palachan-Hazan, R. C. Pardo, K. E. Rehm, A. M. Rogers, C. Ugalde, G Zinkann, S. Bedoor, D. V. Shetty, A. H. Wuosmaa, P Carnelli, J. M. Figueira, A. Chen, D Irvine, S Manwell, J. C. Lighthall, S. T. Marley, N. Patel, and M. Paul. Radioactive Ion Beam studies of α, p process waiting points in X-Ray Bursts. In *XII International Symposium on Nuclei in the Cosmos*, Cairns, Australia, August 5-12, 2012. Proceedings of Science.

[33] B. Harss, R.C. Pardo, K. E. Rehm, F. Borasi, J. P. Greene, R. V F Janssens, C. L. Jiang, J. Nolen, M. Paul, J.P. Schiffer, R. E. Segel, J. Specht, T. F. Wang, P. Wilt, and B. Zabransky. Production of radioactive ion beams using the in-flight technique. *Review of Scientific Instruments*, 71(2):380–387, February 2000. doi: 10.1063/1.1150211.

[34] C. M. Deibel. private communication, August 2017.

[35] K. Schmidt, K. A. Chipps, S. Ahn, J. M. Allen, D. W. Bardayan, J. C. Blackmon, D. Blankstein, J. Browne, K. Y. Chae, J. Cizewski, C. M. Deibel, O. Gomez, U. Greife, U. Hager, M. R. Hall, K. L. Jones, A. Kontos, R. L. Kozub, L. E. Linhardt, M. Matos, Z. Meisel, F. Montes, P. D. O'Malley, W. Ong, S. D. Pain, S. T. Pittman, A. Sachs, H. Schatz, K. T. Schmitt, K. Smith, M. S. Smith, N. F. Soares de Bem, P. J. Thompson, R. Toomey, D. Walter, and C. Wrede. X-ray Burst Studies with the JENSA Gas Jet Target. In *Proceedings of the 14th International Symposium on Nuclei in the Cosmos (NIC2016)*, page 021107, Toki Messe, Niigata, Japan, 2017. doi: 10.7566/JPSCP.14.021107.

[36] C. Ruiz, F. Sarazin, L. Buchmann, T. Davinson, R. E. Azuma, A. A. Chen, B. R. Fulton, D. Groombridge, L. Ling, A. Murphy, J. Pearson, I. Roberts, A. Robinson, A. C. Shotter, P. Walden, and P. J. Woods. Strong resonances in elastic scattering of radioactive ^{21} Na on protons. *Phys. Rev. C*, 65(4):042801, March 2002. doi: 10.1103/PhysRevC.65.042801.

[37] K1200.gif, 2009. URL `https://people.nscl.msu.edu/~hartung/phptry/picsaccel/K1200.gif`.

[38] K. Kimura, T. Izumikawa, R. Koyama, T. Ohnishi, T. Ohtsubo, A. Ozawa, W. Shinozaki, T. Suzuki, M. Takahashi, I. Tanihata, T. Yamaguchi, and Y. Yamaguchi. High-rate particle identification of high-energy heavy ions using a tilted electrode gas ionization chamber. *Nuclear Instruments and Methods in Physics Research Section A: Accelerators, Spectrometers, Detectors and Associated Equipment*, 538 (1–3):608–614, February 2005. doi: 10.1016/j.nima.2004.08.100.

[39] K. Y. Chae, S. Ahn, D. W. Bardayan, K. A. Chipps, B. Manning, S. D. Pain, W. A. Peters, K. T. Schmitt, M. S. Smith, and S. Y. Strauss. Construction of a fast ionization chamber for high-rate particle identification. *Nuclear Instruments and Methods in Physics Research Section A: Accelerators, Spectrometers, Detectors and Associated Equipment*, 751(Supplement C):6–10, July 2014. doi: 10.1016/j.nima.2014.03.016.

[40] J. Lai, K. Macon, J Blackmon, C. M Deibel, A. Lauer, L. E. Linhardt, C williams, D Santiago-Gonzalez, S Kuvin, J Belarge, I Wiedenhover, L.T. Baby, S Almaraz-Calderon, B DiGiovine, C.R. Hoffman, M Avila, B. P. Kay, K. E. Rehm, and B. B. Back. Position-Sensitive Fast Ionization Chambers. *In Progress*, 2017.

[41] B Davin, R. T de Souza, R Yanez, Y Larochelle, R Alfaro, H. S Xu, A Alexander, K Bastin, L Beaulieu, J Dorsett, G Fleener, L Gelovani, T Lefort, J Poehlman, R. J Charity, L. G Sobotka, J Elson, A Wagner, T. X Liu, X. D Liu, W. G Lynch, L Morris, R Shomin, W. P Tan, M. B Tsang, G Verde, and J Yurkon. LASSA: A large area silicon strip array for isotopic identification of charged particles. *Nuclear Instruments and Methods in Physics Research Section A: Accelerators, Spectrometers, Detectors and Associated Equipment*, 473(3):302–318, November 2001. doi: 10.1016/S0168-9002(01)00295-9.

[42] George L. Engel, Muthukumar Sadasivam, Mythreyi Nethi, Jon M. Elson, Lee G. Sobotka, and Robert J. Charity. A multi-channel integrated circuit for use in low- and intermediate-energy nuclear physics—HINP16C. *Nuclear Instruments and Methods in Physics Research Section A: Accelerators, Spectrometers, Detectors and Associated Equipment*, 573(3):418–426, April 2007. doi: 10.1016/j.nima.2006.12.052.

[43] Rene Brun and Fons Rademakers. ROOT — An object oriented data analysis framework. *Nuclear Instruments and Methods in Physics Research A*, 389:81–86, February 1997. doi: 10.1016/S0168-9002(97)00048-X.

[44] O. B. Tarasov and D. Bazin. LISE++: Radioactive beam production with in-flight separators. *Nuclear Instruments and Methods in Physics Research B*, 266:4657–4664, October 2008. doi: 10.1016/j.nimb.2008.05.110.

[45] Y Wang and M Nastasi, editors. *Handbook Modern Ion Beam Materials Analysis 2nd Edition — Materials Science*, volume 2. Materials Research Society, 2nd edition, March 2010.

[46] A. C. L. Barnard and C. C. Kim. Elastic scattering and reactions of protons on argon-40. *Nuclear Physics*, 28(3):428–437, December 1961. doi: 10.1016/0029-5582(61)90033-5.

[47] G. D. Freier, K. F. Famularo, D. M. Zipoy, and J. Leigh. Elastic Scattering of Protons by A40. *Physical Review*, 110:446–447, April 1958. doi: 10.1103/PhysRev.110.446.

[48] John R. Taylor. *An Introduction to Error Analysis: The Study of Uncertainties in Physical Measurements*. University Science Books, Sausalito, Calif, 2nd edition edition, August 1996.

[49] R. E. Azuma, E. Uberseder, E. C. Simpson, C. R. Brune, H. Costantini, R. J. de Boer, J. Görres, M. Heil, P. J. Leblanc, C. Ugalde, and M. Wiescher. AZURE: An R-matrix code for nuclear astrophysics. *Physical Review C*, 81:045805, April 2010. doi: 10.1103/PhysRevC.81.045805.

[50] A. M. Lane and R. G. Thomas. R-Matrix Theory of Nuclear Reactions. *Rev. Mod. Phys.*, 30(2):257–353, April 1958. doi: 10.1103/RevModPhys.30.257.

[51] P. Descouvemont and D. Baye. The R-matrix theory. *Reports on Progress in Physics*, 73(3):036301, March 2010. doi: 10.1088/0034-4885/73/3/036301.

[52] G. D'Agostini. On the use of the covariance matrix to fit correlated data. *Nuclear Instruments and Methods in Physics Research Section A: Accelerators, Spectrometers, Detectors and Associated Equipment*, 346(1):306–311, July 1994. doi: 10.1016/0168-9002(94)90719-6.

[53] A. M. Long. An indirect study of the astrophysical ^{34}ar$(\alpha, p)^{37}$k reaction and its influence on type i x-ray burst light curves, 2016.

[54] Bill Paxton, Lars Bildsten, Aaron Dotter, Falk Herwig, Pierre Lesaffre, and Frank Timmes. Modules for Experiments in Stellar Astrophysics (MESA). *ApJS*, 192 (1):3, January 2011. doi: 10.1088/0067-0049/192/1/3.

[55] Bill Paxton, Pablo Marchant, Josiah Schwab, Evan B. Bauer, Lars Bildsten, Matteo Cantiello, Luc Dessart, R. Farmer, H. Hu, N. Langer, R. H. D. Townsend, Dean M. Townsley, and F. X. Timmes. Modules for Experiments in Stellar Astrophysics

(MESA): Binaries, Pulsations, and Explosions. *arXiv:1506.03146 [astro-ph]*, June 2015.

[56] Jacob Lund Fisker, Hendrik Schatz, and Friedrich-Karl Thielemann. Explosive Hydrogen Burning during Type I X-Ray Bursts. *ApJS*, 174(1):261, January 2008. doi: 10.1086/521104.

Appendix A: AZURE2 Analysis Results

TABLE A.1: This figure describes the results of the AZURE2 fitting process described in Sect. J^π is the spin assignment, Γ_p is the proton partial width, and χ^2 and χ^2/N are the goodness-of-fit statistics discussed in Eq. and the paragraph that follows it. The spin chosen for the reaction rate calculation is in bold (unless the resonance is left out altogether), while resonances with multiple possible fits have the second best fit(s) italicized. In cases where the partial width was discussed in the text as a secondary metric for the quality of the fit, these values were listed in the final column.

E_r (keV)	J^π	χ^2/N	χ^2	Γ_p (keV)
6772	0^+	1.2021	191.14	
	1^-	1.1782	187.34	
	2^+	**0.9489**	**150.87**	
	3^-	1.3240	210.57	
	4^+	1.1851	188.44	
6911 (new)	0^+	1.9930	316.90	
	1^-	1.6121	256.32	
	1^+	1.9830	315.30	
	2^-	**0.9521**	**151.39**	**>350**
	2^+	1.8463	293.57	
	3^-	1.9269	306.39	
	3^+	1.9837	315.42	
	4^+	1.9919	316.71	
	without	1.9948	317.18	
6950	*0^+*	*0.9489*	*150.87*	*~43*
	1^-	0.9632	153.15	
	2^+	**0.8827**	**140.35**	**~170**
	3^-	1.0726	170.55	
	4^+	0.9602	152.67	
7041	0^+	1.0278	163.42	
	1^-	1.0269	163.28	
	2^+	**0.9380**	**149.14**	
	3^-	1.1510	183.01	
	4^+	1.0213	162.40	

(table cont'd.)

TABLE A.1: This figure describes the results of the AZURE2 fitting process described in Sect. J^π is the spin assignment, Γ_p is the proton partial width, and χ^2 and χ^2/N are the goodness-of-fit statistics discussed in Eq. and the paragraph that follows it. The spin chosen for the reaction rate calculation is in bold (unless the resonance is left out altogether), while resonances with multiple possible fits have the second best fit(s) italicized. In cases where the partial width was discussed in the text as a secondary metric for the quality of the fit, these values were listed in the final column.

E_r (keV)	J^π	χ^2/N	χ^2	Γ_p (keV)
7176	0^+	1.0825	172.12	
	1^-	1.0233	162.71	
	2^+	**0.9270**	**147.39**	
	3^-	1.1473	182.42	
	4^+	1.0860	172.67	
7327 (new)	0^+	0.9462	150.45	
	1^-	0.9394	149.37	
	1^+	*0.9298*	*147.84*	*~48*
	2^-	0.9439	150.08	
	2^+	*0.9261*	*147.26*	*~104*
	3^-	1.0562	167.93	
	3^+	0.9405	149.54	
	4^+	0.9449	150.25	
	without	**0.9489**	**150.88**	
7370	0^+	0.9922	157.76	
	1^-	0.9168	145.77	~136
	2^+	*0.8975*	*142.70*	*~212*
	3^-	0.9243	146.97	
	4^+	0.9925	157.82	
	without	**0.9925**	**157.82**	
7480	**0^+**	**0.9276**	**147.50**	**147**
	1^-	0.9314	148.09	
	2^+	*0.9031*	*143.59*	*263*
	3^-	1.0466	166.41	
	4^+	0.9307	147.98	
	without	0.9585	152.39	

(table cont'd.)

TABLE A.1: This figure describes the results of the AZURE2 fitting process described in Sect. J^π is the spin assignment, Γ_p is the proton partial width, and χ^2 and χ^2/N are the goodness-of-fit statistics discussed in Eq. and the paragraph that follows it. The spin chosen for the reaction rate calculation is in bold (unless the resonance is left out altogether), while resonances with multiple possible fits have the second best fit(s) italicized. In cases where the partial width was discussed in the text as a secondary metric for the quality of the fit, these values were listed in the final column.

E_r (keV)	J^π	χ^2/N	χ^2	Γ_p (keV)
7549 (new)	0^+	1.0276	163.40	
	1^-	0.9542	151.73	
	1^+	0.9573	152.21	
	2^-	*0.9197*	*146.24*	*>700*
	2^+	**0.9109**	**144.83**	**~31**
	3^-	1.0256	163.00	
	3^+	1.0075	160.20	
	4^+	1.0389	165.80	
	without	1.0183	161.92	
7693 (new)	0^+	0.9272	147.43	
	1^-	0.8959	142.44	
	1^+	0.9060	144.05	
	2^-	0.8916	141.77	
	2^+	0.8911	141.69	
	3^-	1.0047	159.75	
	3^+	0.9090	146.42	
	4^+	0.9252	147.11	
	without	**0.9298**	**147.84**	
7801	0^+	0.9659	153.58	
	1^-	*0.9328*	*148.32*	*~50*
	2^+	**0.9187**	**146.08**	**~50**
	3^-	1.0597	168.49	
	4^+	0.9640	153.80	
8020	0^+	0.9577	152.27	
	1^-	*0.9141*	*145.35*	**~111**
	2^+	**0.8978**	**142.75**	**~141**
	3^-	1.0142	161.25	
	4^+	0.9609	152.78	

(table cont'd.)

TABLE A.1:This figure describes the results of the AZURE2 fitting process described in Sect. J^π is the spin assignment, Γ_p is the proton partial width, and χ^2 and χ^2/N are the goodness-of-fit statistics discussed in Eq. and the paragraph that follows it. The spin chosen for the reaction rate calculation is in bold (unless the resonance is left out altogether), while resonances with multiple possible fits have the second best fit(s) italicized. In cases where the partial width was discussed in the text as a secondary metric for the quality of the fit, these values were listed in the final column.

E_r (keV)	J^π	χ^2/N	χ^2	Γ_p (keV)
8189	*0^+*	*0.9462*	*150.45*	
	1^-	*0.9464*	*150.47*	
	2^+	**0.9422**	**149.81**	
	3^-	1.0818	172.00	
	4^+	*0.9525*	*151.44*	
8293 (new)	0^+	0.9286	147.64	
	1^-	0.8861	140.89	
	1^+	0.9182	146.00	
	2^-	0.9321	148.21	
	2^+	0.9126	145.11	
	3^-	1.0180	161.89	
	3^+	0.9090	144.53	
	4^+	0.9084	144.44	
	without	**0.9294**	**147.78**	
8322	0^+	0.9928	157.86	
	1^-	0.9719	154.54	
	2^+	**0.9220**	**146.60**	
	3^-	1.1005	174.98	
	4^+	0.9815	156.07	

(table cont'd.)

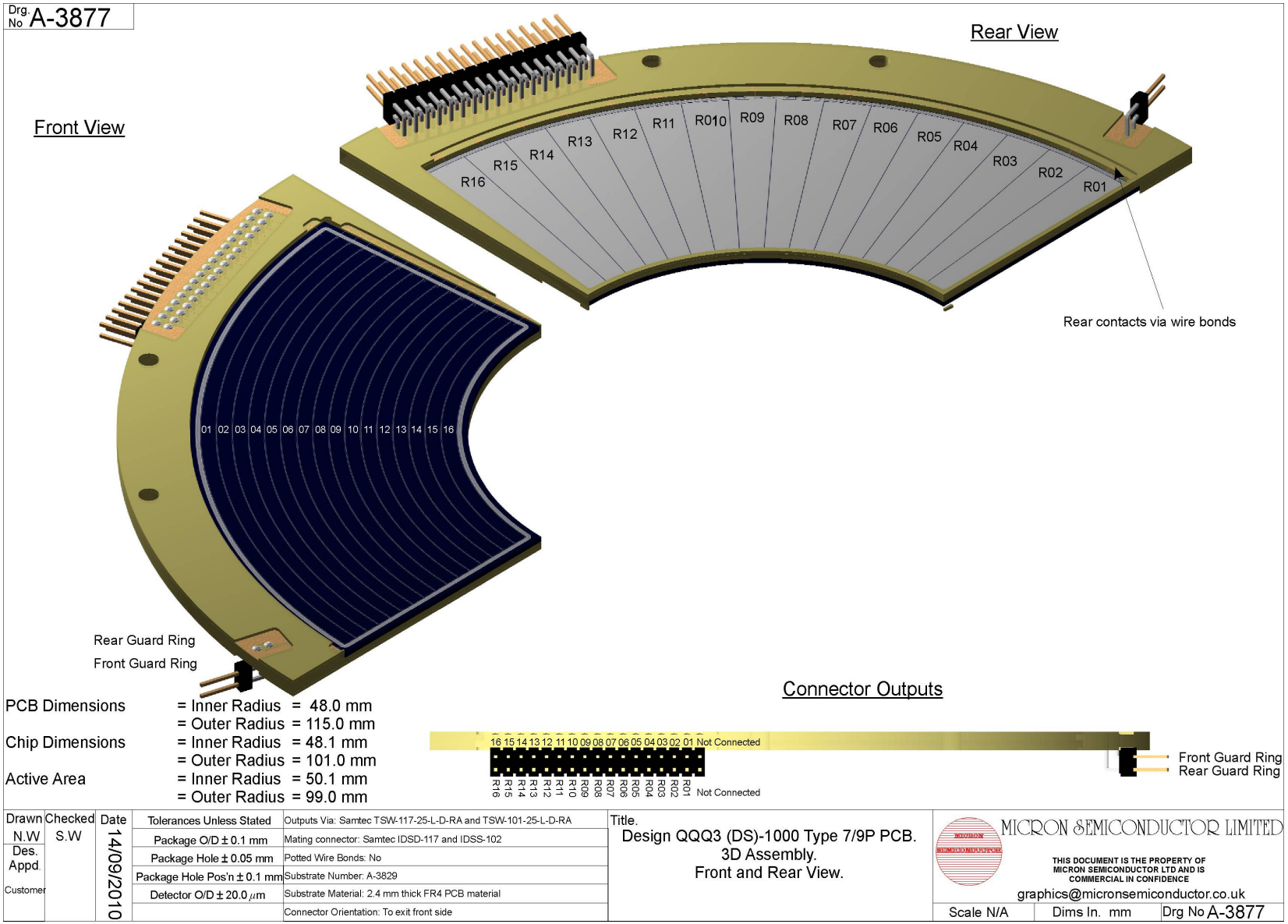

FIGURE B.1. Manufacturer Schematic of QQQ3 16 channel Si detectors.

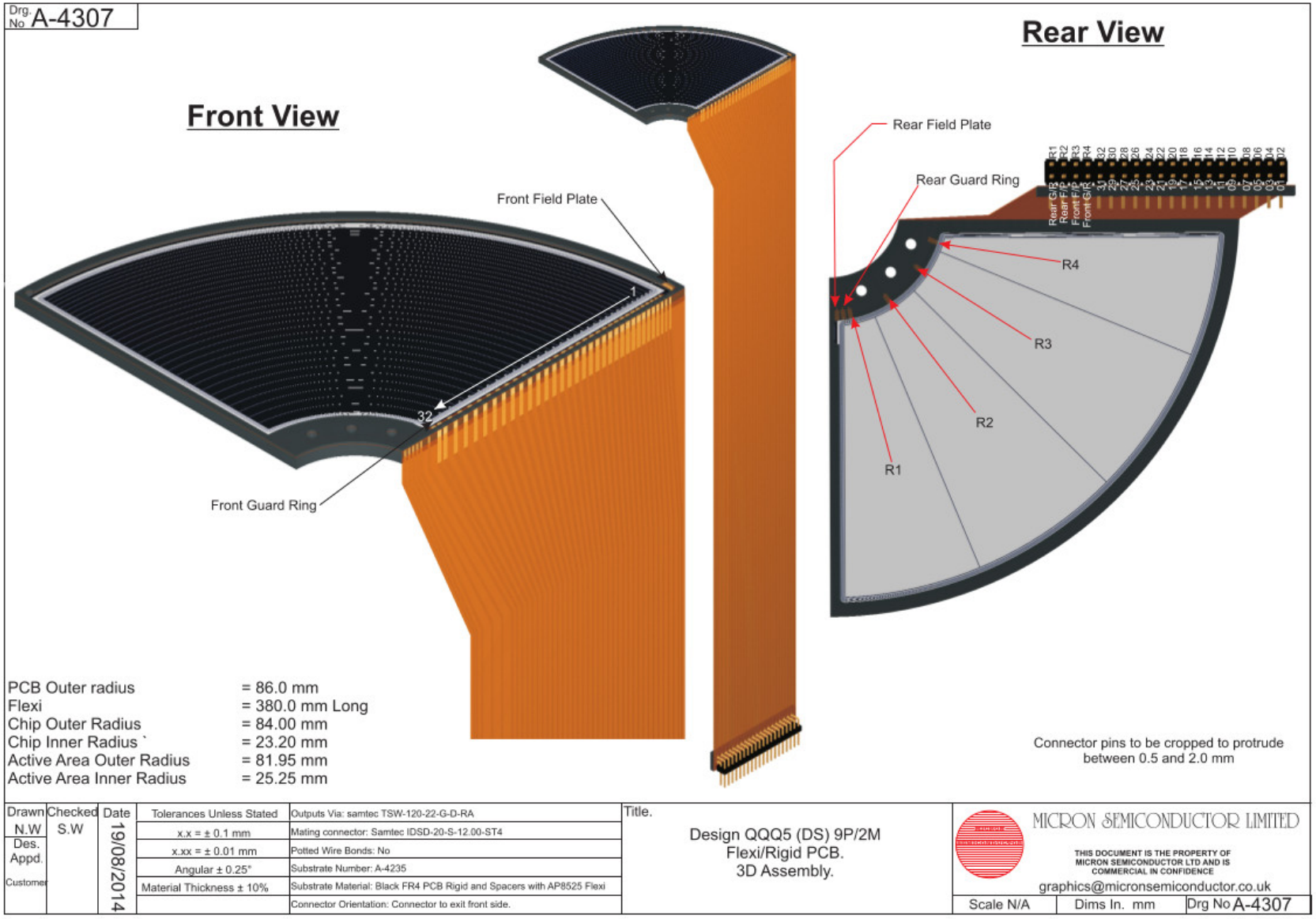

FIGURE B.2. Manufacturer Schematic of 100 μm QQQ5 32 channel Si detectors.

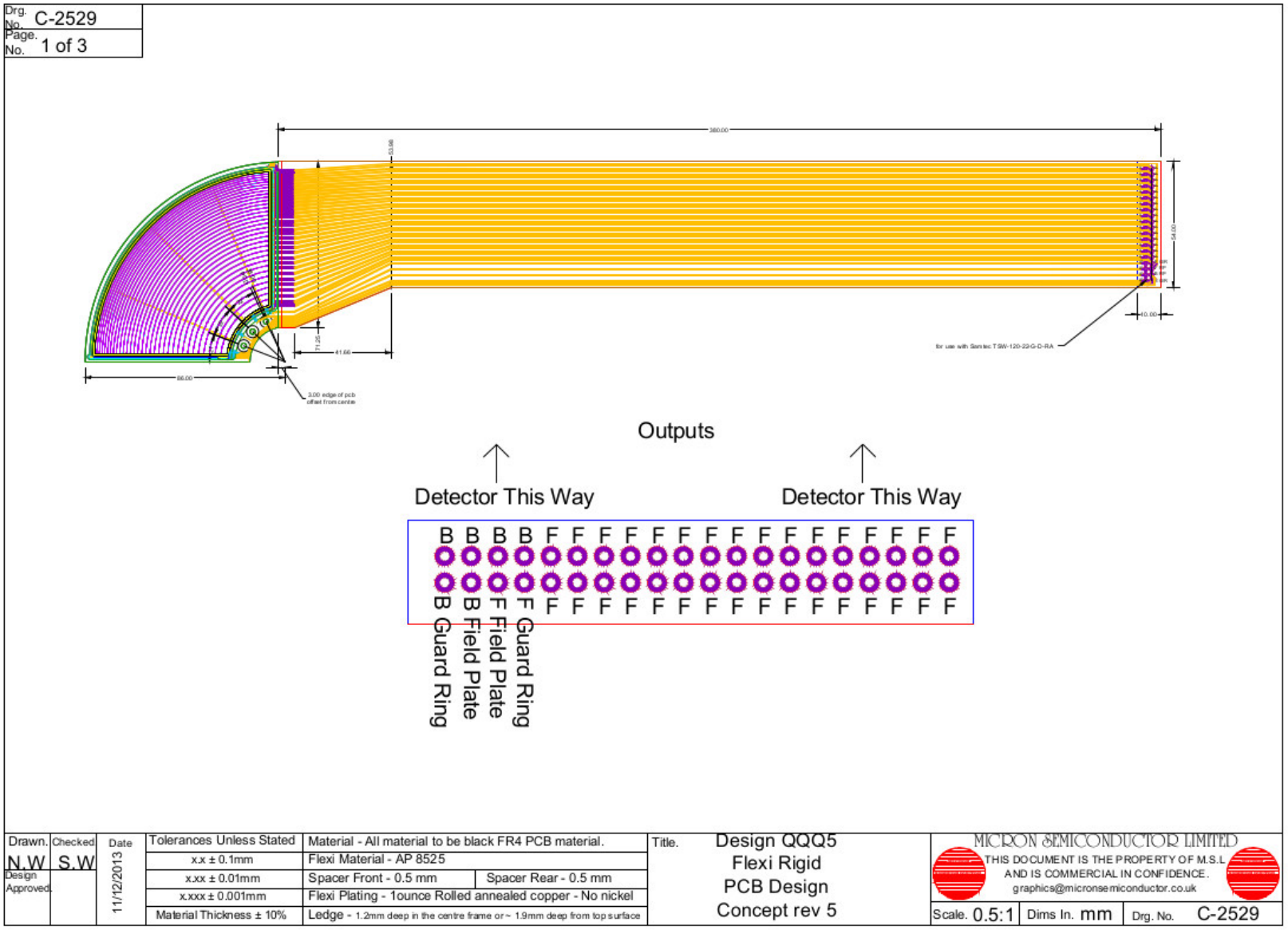

FIGURE B.3. Manufacturer Schematic of 1 mm QQQ5 32 channel Si detectors.

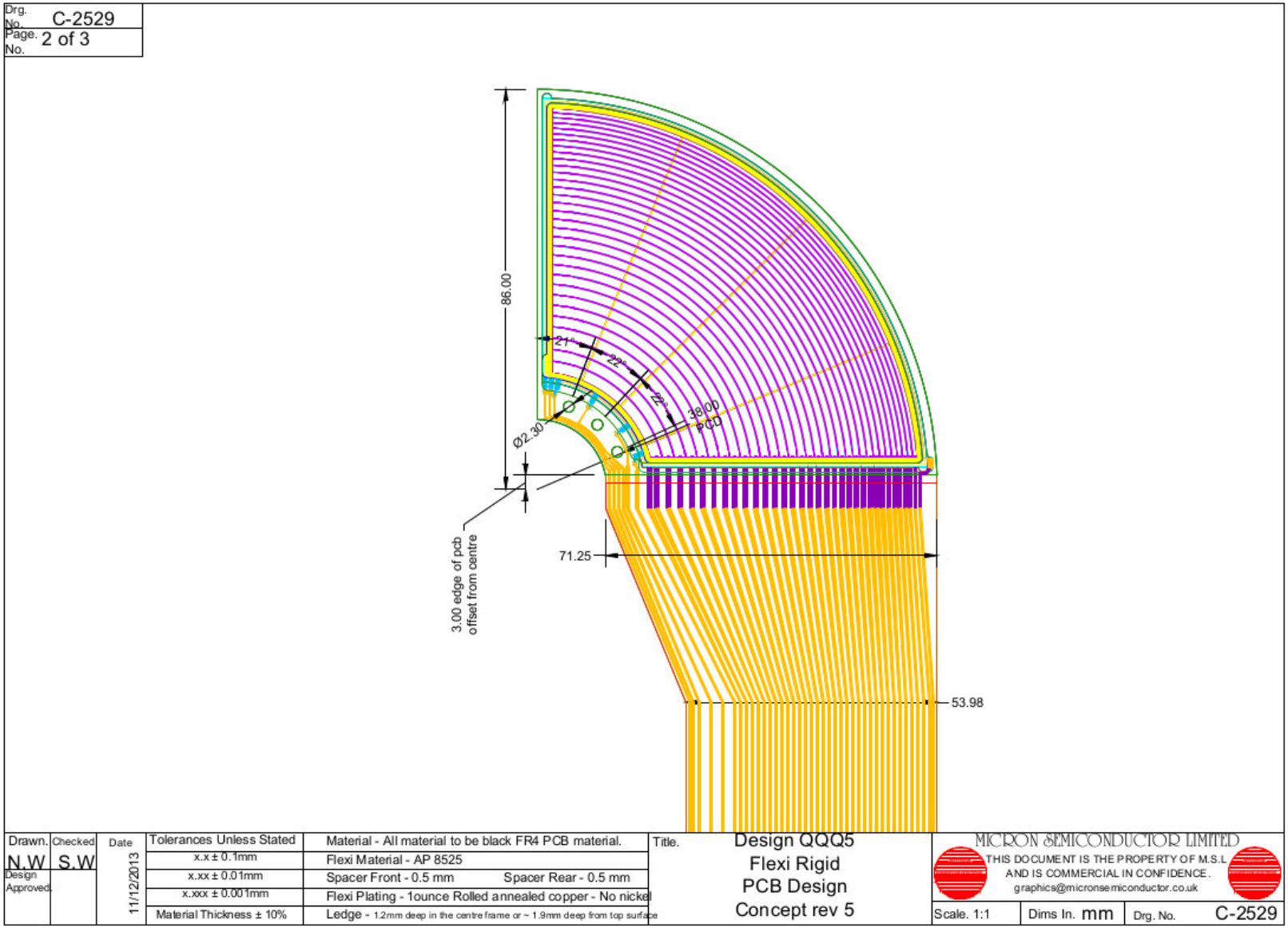

FIGURE B.4. Manufacturer Schematic of 1 mm QQQ5 32 channel Si detectors.

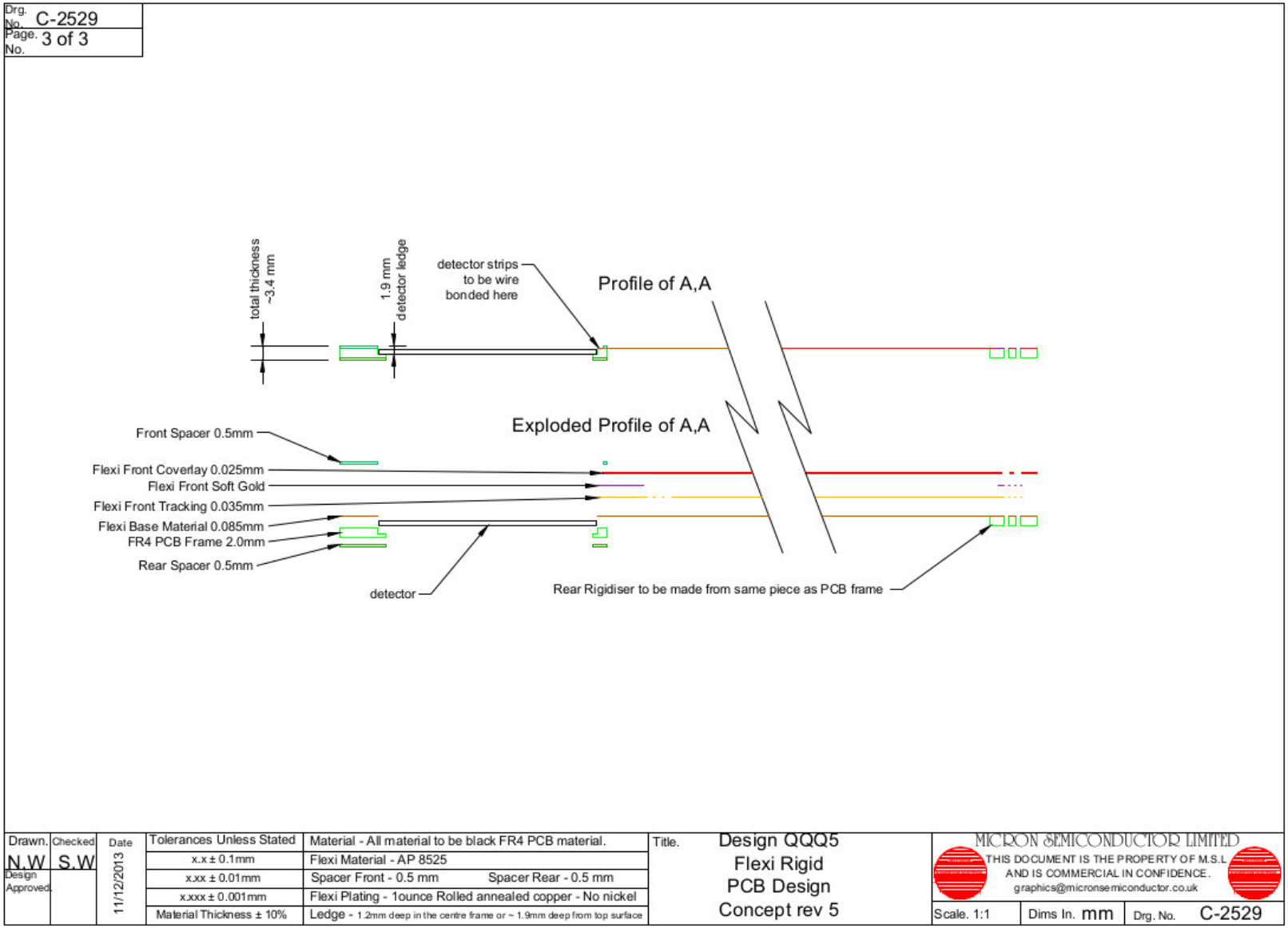

FIGURE B.5. Manufacturer Schematic of 1 mm QQQ5 32 channel Si detectors.

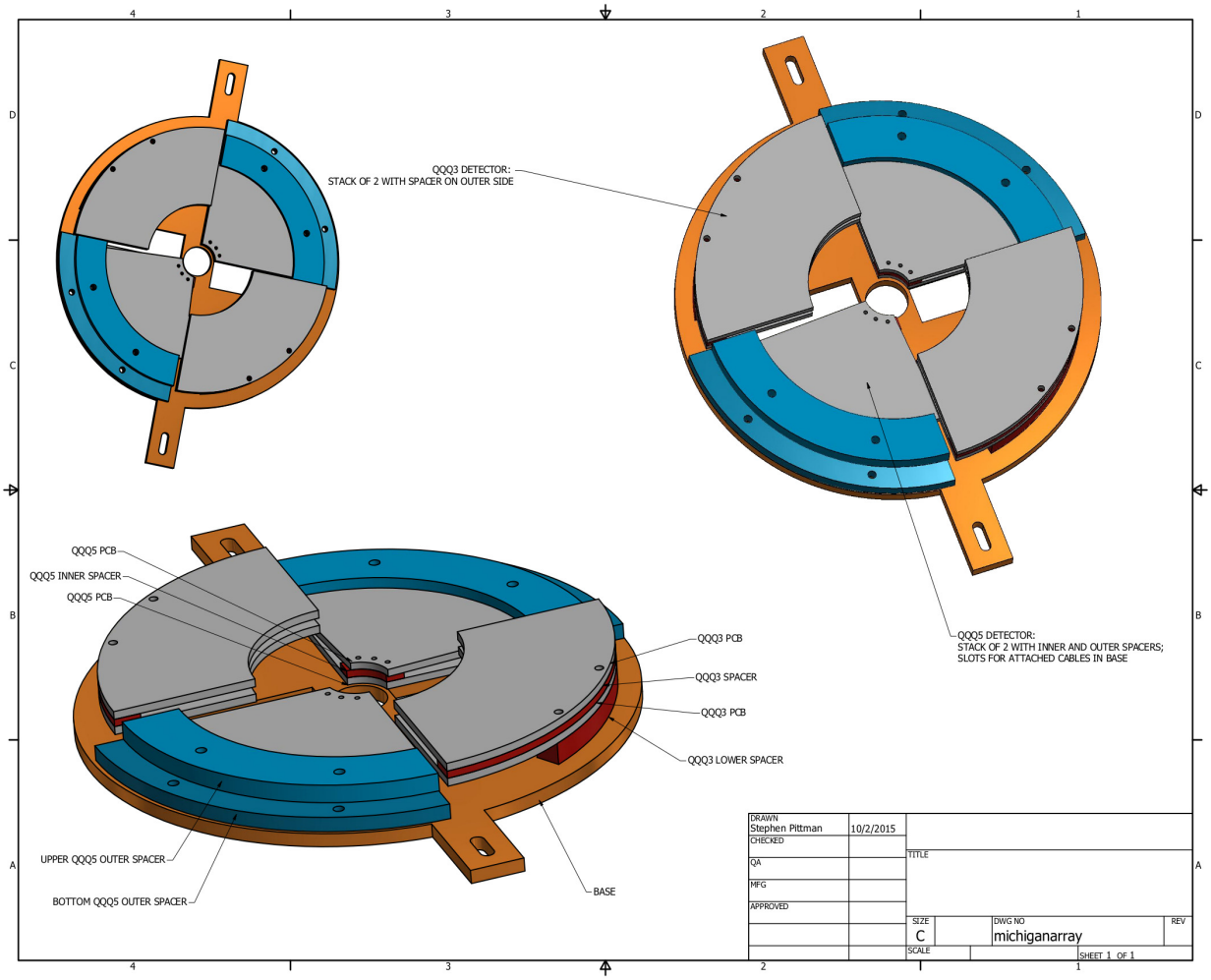

FIGURE B.6. Computer aided design rendering of the the Si detector assembly. The spacers separating the telescope layers are shown in red and blue for the QQQ3's and QQQ5's, respectively, and the mount base is shown in orange. The detectors covering shallower angles are the QQQ5's, while those covering steeper angles are the QQQ3's. An additional .1 smm QQQ5 was mounted on in front of the pictured two, not shown here. Image courtesy of Erin Good.

Vita

Amber C. Lauer is a native Oregonian who received a BS in Math in 2007 and MS in Physics in 2011 from Portland State University. She then travelled here to the great state of Louisiana to attend LSU and pursue a PhD in physics. This degree is in progress and she is presently a Doctoral Candidate looking forward to a Laboratory Post-doctoral position in the fall of 2017.